



Transition of flow regime along a marine-terminating outlet glacier in East Antarctica

D. Callens¹, K. Matsuoka², D. Steinhage³, B. Smith⁴, E. Witrant^{5,1}, and F. Pattyn¹

¹Laboratoire de Glaciologie, Université Libre de Bruxelles, Brussels, Belgium

²Norwegian Polar Institute, Tromsø, Norway

³Alfred-Wegener-Institut Helmholtz-Zentrum für Polar- und Meeresforschung, Bremerhaven, Germany

⁴Applied Physics Laboratory, University of Washington, Seattle, WA, USA

⁵GIPSA-lab, Université Joseph Fourier, Grenoble, France

Correspondence to: D. Callens (dcallens@ulb.ac.be)

Received: 10 September 2013 – Published in The Cryosphere Discuss.: 7 October 2013

Revised: 21 March 2014 – Accepted: 25 March 2014 – Published: 13 May 2014

Abstract. We present results of a multi-methodological approach to characterize the flow regime of West Ragnhild Glacier, the widest glacier in Dronning Maud Land, Antarctica. A new airborne radar survey points to substantially thicker ice (> 2000 m) than previously thought. With a discharge estimate of $13\text{--}14\text{ Gtyr}^{-1}$, West Ragnhild Glacier thus becomes one of the three major outlet glaciers in Dronning Maud Land. Its bed topography is distinct between the upstream and downstream section: in the downstream section (< 65 km upstream of the grounding line), the glacier overlies a wide and flat basin well below the sea level, while the upstream region is more mountainous. Spectral analysis of the bed topography also reveals this clear contrast and suggests that the downstream area is sediment covered. Furthermore, bed-returned power varies by 30 dB within 20 km near the bed flatness transition, suggesting that the water content at bed/ice interface increases over a short distance downstream, hence pointing to water-rich sediment. Ice flow speed observed in the downstream part of the glacier ($\sim 250\text{ myr}^{-1}$) can only be explained through very low basal friction, leading to a substantial amount of basal sliding in the downstream 65 km of the glacier. All the above lines of evidence (sediment bed, wetness and basal motion) and the relatively flat grounding zone give the potential for West Ragnhild Glacier to be more sensitive to external forcing compared to other major outlet glaciers in this region, which are more stable due to their bed geometry (e.g. Shirase Glacier).

1 Introduction

The overall mass balance of the Antarctic ice sheet is dominated by a significant mass deficit in West Antarctica (Rignot et al., 2008; Pritchard et al., 2012). This is primarily due to thinning and acceleration of glaciers (e.g. Pine Island Glacier; Joughin et al., 2003) mainly driven by the loss of buttressing from ice shelves (Schoof, 2010). Concurrently, the trend in East Antarctica is weaker. The East Antarctic ice sheet (EAIS) is only losing mass slightly, as increased surface accumulation compensates mass loss through outlet glaciers (Shepherd et al., 2012). While Miles et al. (2013) observe a link between front migration and climate forcing, a significant widespread thinning trend along the Pacific coast of the EAIS remains lacking.

Although East Antarctica is mainly continental, limited observations in Dronning Maud Land (DML), show that the ice sheet seaward of the inland mountains lies on a bed well below sea level (BEDMAP2; Fretwell et al., 2013) and most of the ice from the polar plateau is discharged through numerous glaciers in between coastal mountain ranges. The ice-dynamical consequences of such settings have yet to be explored. In this paper we investigate the marine boundary of such a glacier system draining the EAIS in DML.

The coastal region of DML is characterized by numerous outlet glaciers feeding into ice shelves (Fig. 1a). They are generally short in length but reach out to the continental shelf edge. The stability of these ice shelves is primarily ensured through the presence of ice rises and pinning points, making

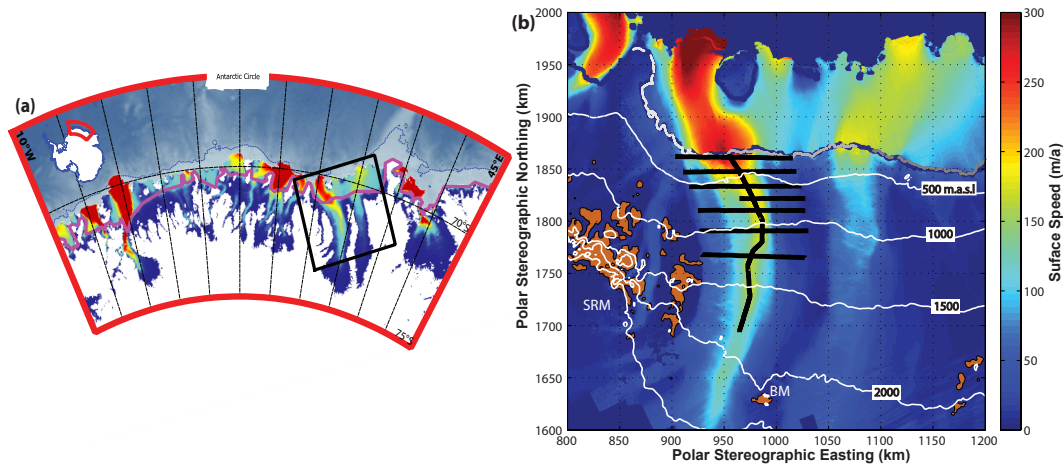


Fig. 1. Overview map of West Ragnhild Glacier, Dronning Maud Land, East Antarctica. **(a)** Dronning Maud Land. Ice flow speed is shown on the same scale as for panel **(b)** (but white when $< 15 \text{ myr}^{-1}$; Rignot et al., 2011a). The grounding line is shown in purple (Bindschadler et al., 2011). Rock outcrops are shown in brown (SCAR, 2012). The square shows the $400 \text{ km} \times 400 \text{ km}$ area covered by the map on panel **(b)**. The inset shows the coverage of panel **(a)**. **(b)** West Ragnhild Glacier. Background colour shows the surface flow speed derived from satellite interferometry and speckle tracking. Contours show surface elevations at 500 m interval (Bamber et al., 2009). From west to east, the grounding line is defined on the basis of a pair of PALSAR images taken in 2007 (light grey) and two pairs of RADARSAT (middle grey and dark grey) taken in 2000 (Rignot et al., 2011b). Black lines are the longitudinal and transverse radar profiles. Rock outcrops as in **(a)**. SRM and BM stand for Sør Rondane Mountains and Belgica Mountains, respectively.

the ice shelf locally grounded. Potential unpinning of these ice shelves would inevitably lead to ice shelf speed up, which makes them sensitive to marine forcing.

Of all glaciers in DML, West Ragnhild Glacier is the widest ($\approx 90 \text{ km}$) and longest. Its ice flow speed is already 100 myr^{-1} 250 km upstream from the grounding line (Fig. 1b). Based on the ice thickness data presented in this paper, we estimate the grounding line mass flux to be $13\text{--}14 \text{ Gtyr}^{-1}$, which constitutes roughly 10% of the total discharge from DML (Rignot et al., 2008). This is of the same order of magnitude as Shirase Glacier ($13.8 \pm 1.6 \text{ Gtyr}^{-1}$; Pattyn and Derauw, 2002) and Jutulstraumen (14.2 Gtyr^{-1} ; Høydal, 1996), the other two major outlet glaciers in the DML region.

The stability of West Ragnhild Glacier is most likely governed by the dynamics of its ice shelf which is dominated by two important ice rises and several pinning points. While rapid changes at the marine boundary have not yet been observed, Rignot et al. (2013) point to an exceedance of basal melt (underneath the ice shelf and at the grounding line) over calving for several ice shelves in DML (including Roi Baudouin Ice Shelf, downstream of West Ragnhild Glacier). Melting at the grounding line 50 km west from West Ragnhild Glacier has been reported in Pattyn et al. (2012), but its magnitude is of the orders of tens of centimetres per year.

To understand what makes West Ragnhild Glacier one of the three most significant mass outputs in DML, we investigate its basal conditions using satellite remote sensing, airborne radar and ice sheet modelling. First, radar analysis reveals the geometry of the bed. Second, we characterize

the roughness of the bed and its reflectivity through spectral and bed-returned power analyses, which inform us of the nature of the bed as well as of the water content. Finally, we estimate the basal friction through inverse modelling to reconstruct basal motion. We subsequently discuss the consequences of a marine-terminating East Antarctic outlet glacier, characterized by a wet sediment and dominated by basal motion/sliding.

2 Data acquisition

Ice flow surface velocities are generated based on RADARSAT data acquired during the austral spring of 2000. These velocities combine phase and speckle tracking offsets, using methods that minimize the error of the final combined product (Joughin, 2002). The resolution of the velocity data is $500 \text{ m} \times 500 \text{ m}$, covering the main trunk of West Ragnhild Glacier and its vicinity (Fig. 1b).

The airborne radio echo sounding survey was carried out on West Ragnhild Glacier during the austral summer 2010–2011, resulting in one longitudinal (along-flow) profile and seven transverse profiles (Fig. 1b). The radar system employed a 150 MHz centre frequency and transmitted bursts of 600 and 60 ns duration, toggling between the two bursts (Nixdorf et al., 1999; Steinhage et al., 2001). The system recorded at a rate of 20 Hz. For further signal-to-noise improvement, the data of same burst length were stacked ten-fold, resulting in a horizontal resolution of $80 \pm 20 \text{ m}$. We identified the bed echo along 91% of the entire survey

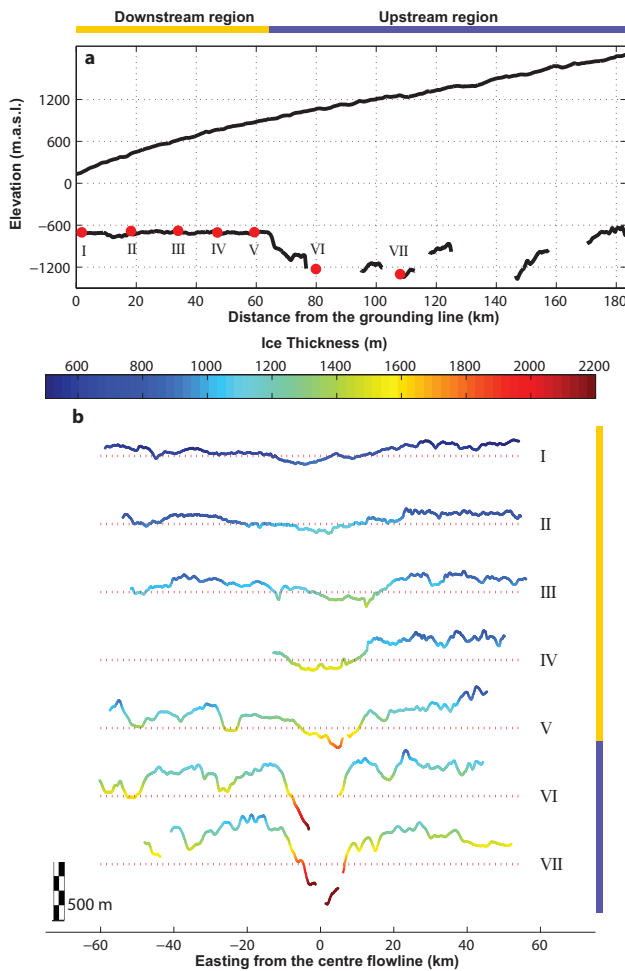


Fig. 2. Radar data. **(a)** Ice and bed topography along the central flowline. The red circles are the locations of the cross profiles. **(b)** Bed topography (ordinate) and ice thickness (colour) measured across the flow. The red dotted lines show the isodepth of 600 m b.s.l., the approximate elevation of the flat basin measured along the centre flowline **(a)** and the reference for each profile. Transverse profiles are numbered from I to VII on both panels. The yellow and blue line illustrates our understanding of the downstream and upstream region.

(Fig. 2). Most sections lacking a bed echo are shorter than ~ 10 km (the maximum data gap is 20 km). Adjacent regions to these data gaps slope down steeply toward the data gaps. Therefore, the data gaps probably correspond to a deep bed and thick ice, causing an increased radar signal attenuation, and hence loss of signal.

Ice thickness was derived using a constant radio wave propagation speed of $168 \mu\text{s}^{-1}$. Surface elevation was obtained by laser altimetry from the aircraft, and bed elevation was subsequently derived by subtracting the ice thickness from the surface elevation. We applied the geoid height of 20 m above the EGM96 ellipsoid (Rapp, 1997) to derive the surface and bed elevations relative to sea level.

3 Mapping the subglacial topography

Compared to older data sets of Antarctic bedrock topography (e.g. BEDMAP; Lythe et al., 2001), our new radar survey reveals a significantly different picture¹. The survey highlights a marked contrast in bed topography (Fig. 2). Between the Sør Rondane and Belgica Mountains, ice flows in a deeply incised valley, ~ 20 km wide, lying ~ 1000 m below sea level at the two uppermost transverse profiles (Fig. 2b). The bed topography is rather variable here, fluctuating between 1200 and 800 m b.s.l. Further downstream, bedrock elevation increases rapidly (more than 500 m within 10 km distance) up to a flat subglacial lowland lying around 600 m b.s.l. This can be observed on both the longitudinal (Fig. 2a) and cross profiles (Fig. 2b). The elevation of this lowland varies less than 50 m locally, so the lowland is much flatter than the landward valley between Sør Rondane and Belgica Mountains. The amplitude of the local elevation variations increases sharply between cross profiles 4 and 5 as we reach the piedmont of the Sør Rondane Mountains. This is also the zone where we find the onset of the subglacial valley, described earlier.

4 Spectral analysis of bed topography

4.1 Bed roughness index

One way to quantitatively characterize the above-described bed conditions is to calculate bed roughness. The bed roughness index RI is obtained by applying a fast Fourier transform (FFT) to the bed elevation within a moving window (Taylor et al., 2004):

$$RI = \int_{f_{\min}}^{f_{\max}} \frac{|X[f]|^2}{N_T \Delta x} df, \quad (1)$$

where $f_{\min} = 1/(N_T \Delta x)$, $f_{\max} = 1/(2 \Delta x)$, $N_T = 2^n$ is the number of data points in the window, Δx is the sampling interval (100 m in our case) and where

$$X[f] = \sum_{d=1}^{N_T} x(d) e^{\frac{2\pi i}{N_T} (d-1)(f-1)}. \quad (2)$$

Equation (2) is the definition of the FFT for a dataset $x(d)$ with index d in the range $1 \leq d \leq N_T$, and $X[f]$ is the same data set in the frequency domain with index f in the range $f_{\min} \leq f \leq f_{\max}$. In other words, the bed roughness index RI is the integral of the resultant power spectrum within each of the moving windows.

We first resample the radar-derived bed topography (80 ± 20 m intervals) with a fixed (100 m) interval. We then detrend the measured bed elevation in each moving window,

¹The data collected for this paper are incorporated in the recently published BEDMAP2 data set (Fretwell et al., 2013).

which is required to be able to perform an FFT. The method is applied within a 2^n data point window. Several authors recommend $n \geq 5$ (Taylor et al., 2004; Bingham and Siegert, 2009; Rippin et al., 2011). By using $n = 6$ we are able to analyse roughness over wavelengths ranging from 200 up to 6400 m.

4.2 Results

The longitudinal bed profile (Fig. 2) reveals two distinct areas: a flat area (between the grounding line and 65 km upstream) and an intersected subglacial relief typical of subglacial mountain ranges. The transition between them occurs within 10 km. The bed roughness index RI is capable of quantifying this difference (Figs. 3 and 4a). While the two regions are still quite distinct, the transition of roughness from one to the other is more gradual than expected from visual interpretation. For the downstream cross profiles (I–III), the bed roughness is approximately constant, pointing to a wide and relatively smooth lowland. Following the analysis of Bingham and Siegert (2009), the flat and smooth area in the downstream section of the West Ragnhild Glacier may therefore very well be overlain by marine sediment. According to the further upstream profiles (IV–V), the bed is rougher away from the current glacier flowline (longitudinal radar profile). The low roughness area is therefore restricted to the zones of fast ice flow. Once outside this section, bed roughness indices increase, pointing to a rougher surface (VI–VII).

5 Analysis of bed-returned power

5.1 Analytical setup

To further examine the spatial distribution of basal conditions, we analyse the radar power returned from the bed, hereafter called BRP. The geometrically corrected BRP, BRP^c , can be seen as a proxy for bed reflectivity if englacial effects do not vary along the radar profile (Matsuoka, 2011). The BRP^c is affected by both englacial attenuation L and bed reflectivity R . In the decibel scale, $[x]_{\text{dB}} = 10 \log_{10}(x)$, this relationship can be written as

$$\begin{aligned} [\text{BRP}^c]_{\text{dB}} &= [\text{BRP}]_{\text{dB}} + 10 \log_{10} \left(h + \frac{H}{n} \right)^2, \\ &\simeq [R]_{\text{dB}} - [L]_{\text{dB}}. \end{aligned} \quad (3)$$

The geometrically corrected bed-returned power BRP^c can be calculated based on the measured BRP returned from the bed and a geometric factor defined by $(h + H/n)^2$. Here, h is the height of the aircraft above the glacier surface, H is the ice thickness (distance between the surface and the bed of the ice mass), and n is the refraction index of the ice (~ 1.8 ; Matsuoka et al., 2012). The BRP^c is then normalized to the mean of the observed values.

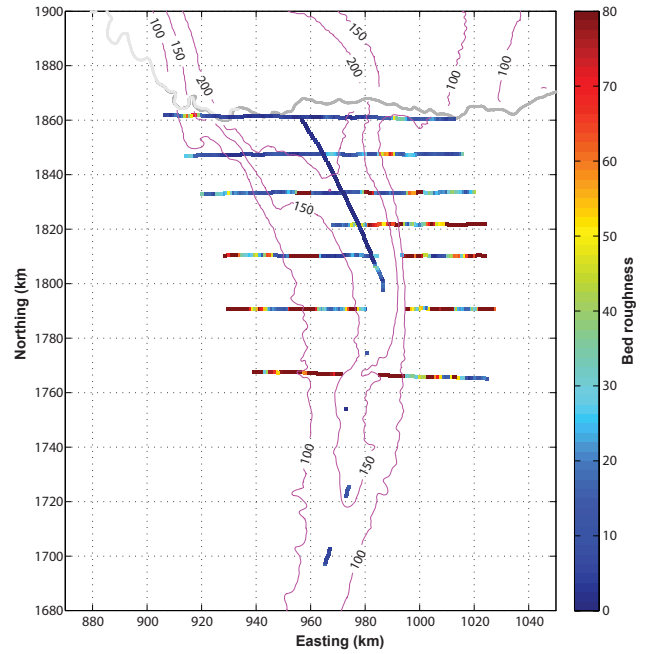


Fig. 3. Bed roughness analysis. Bed roughness index of the basal topography (colour) calculated for wavelengths ranging from 200 to 6400 m. The grounding line is the same as in Fig. 1b. Short legs of absent bed echoes result in long gaps in the estimated bed roughness indices due to the window-based calculation of the bed roughness index. Larger RI corresponds to rougher bed. Contour lines represent surface speed (m a^{-1}).

One has to note that effects of temporal changes in the instrumental characteristics and of ice crystal alignments are ignored in Eq. (3). Englacial attenuation has contributions from pure ice and chemical constituents included in the glacier ice, both of which depend exponentially on ice temperature.

We estimate attenuation L using Eqs. (4)–(6) listed below (Matsuoka et al., 2012). The depth-averaged attenuation rate $\langle N \rangle$ is derived from the depth profile of the attenuation rate $N(z)$, i.e.,

$$[L]_{\text{dB}} = \int_0^H N(z) dz. \quad (4)$$

The attenuation profile $N(z)$ is proportional to local ice conductivity σ :

$$N(z) = \frac{1000(10 \log_{10} e)}{c \varepsilon_0 \sqrt{\varepsilon}} \sigma(z) \approx 0.914 \sigma(z), \quad (5)$$

where c is the wave velocity in vacuum, ε_0 is the permittivity of free space and ε is the relative permittivity of the ice. Since we focus only on the contribution of pure ice to the attenuation, conductivity depends only on temperature through

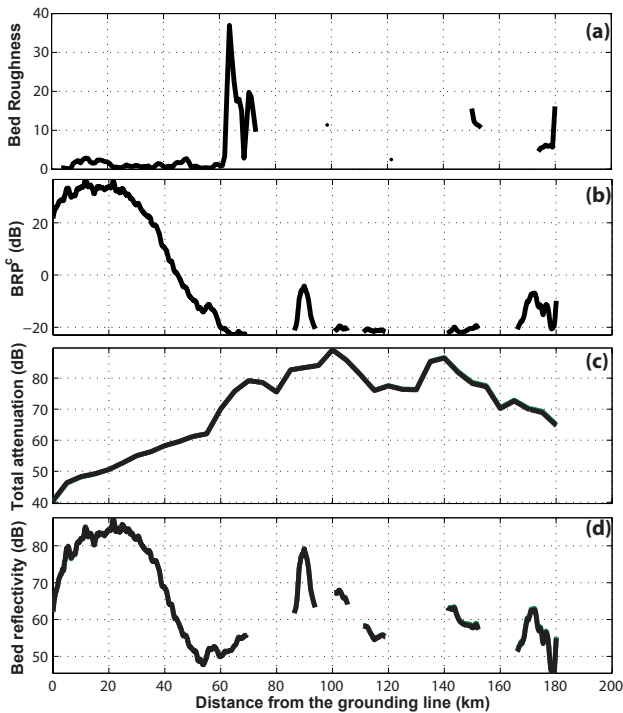


Fig. 4. Subglacial conditions along the central flowline. (a) Bed roughness index RI; (b) geometrically corrected bed-returned power BRP^c ; (c) englacial attenuation L ; (d) bed reflectivity R .

an Arrhenius-type relationship.

$$\sigma = \sigma_0 \exp \left[-\frac{E_0}{k} \left(\frac{1}{T(z)} - \frac{1}{T_r} \right) \right], \quad (6)$$

where $\sigma_0 = 15.4 \mu\text{S m}^{-1}$ is the pure-ice conductivity at the reference temperature $T_r = 251 \text{ K}$, $T(z)$ is the vertical profile of temperature, $E_0 = 0.33 \text{ eV}$ is the activation energy and $k = 8.617 \times 10^{-5} \text{ eV K}^{-1}$ is the Boltzmann constant (Matsuoka et al., 2012).

Englacial temperatures $T(z)$ for the attenuation model (Eq. 6) are calculated using a two-dimensional thermomechanical higher-order model (Pattyn, 2002, 2003). Details of this approach are given in Matsuoka et al. (2012). We use a geothermal heat flux of 42 mW m^{-2} as lower boundary condition. However, as shown in Matsuoka et al. (2012), the exact choice of geothermal heat flux will not affect the modelled englacial attenuation since the bed in the surveyed domain is predicted to be at the pressure melting point everywhere even with a flux as low as 42 mW m^{-2} . Once the bed reaches pressure melting point, additional geothermal and shear heating have virtually no impact on ice temperature, hence on englacial attenuation (Matsuoka, 2011). Therefore, the estimated along-flow patterns of the attenuation and bed reflectivity are robust regardless of the uncertainties in geothermal heat flux. Figure 4c shows $[L]$ along the longitudinal profile.

Although the chemical contribution to attenuation can nearly equal the pure-ice contribution near the coast (Matsuoka et al., 2012), the lack of observation forces us to ignore its contribution and to use only the pure-ice contribution to estimate englacial attenuation. Furthermore, MacGregor et al. (2007) and Matsuoka et al. (2012) showed that the relative importance of impurities contribution decreases as temperature increases. The modelling reveals a mean attenuation rate from pure ice between 20.2 and 23.1 dB km^{-1} . For this range of value, Matsuoka et al. (2012) determine that chemical contribution is less than the fifth of the pure ice contribution.

5.2 Results

In the upstream valley, BRP^c remains relatively low (-20 dB) and varies little (several dB) except at two sites where BRP^c shows anomalous features (90 km and 170 km upstream from the grounding line; Fig. 4b). Further downstream, BRP^c increases by $\sim 50 \text{ dB}$ within 20 km, over which the ice thins only by $\sim 200 \text{ m}$ (Fig. 2).

To clarify contributions of the bed reflectivity on BRP^c , we estimate the englacial attenuation using the predicted temperature (Fig. 4c). Attenuation decreases $\sim 20 \text{ dB}$ within 10 km at 65 km upstream from the grounding line due to a decrease in ice thickness. Further downstream, attenuation gradually decreases by 20 dB over 50 km, which is probably more related to the changes in ice thickness than to changes in depth-averaged attenuation rate $\langle N \rangle$. To retrieve the actual bed reflectivity, we estimated bed reflectivity from BRP^c and englacial attenuation using Eq. (3). The corresponding estimated bed reflectivity rapidly increases, approaching the grounding line at 40–50 km, from where it varies little within the last $\sim 30 \text{ km}$ (Fig. 4d). The high bed reflectivity in the zone immediately upstream of the grounding line may eventually point to wet bed conditions. This high bed reflectivity is not directly related to the smoother bed interface because RI is calculated for the wavelengths longer than 200 m but the reflectivity is affected by the bed smoothness in the scale of several wavelengths of the radio wave (5 m for this study). In the next section, we will investigate whether wet basal conditions are likely or not.

6 Ice flow modelling

6.1 Model setup

Velocity data show that West Ragnhild Glacier accelerates steadily towards the grounding line (Fig. 5). In this section, using an ice flow model, we will infer the required spatial distribution of basal friction (or, inversely, slipperiness) to match modelled ice flow velocities to the satellite-observed ones. The most common method is an inversion method in which a friction parameter is spatially optimized in

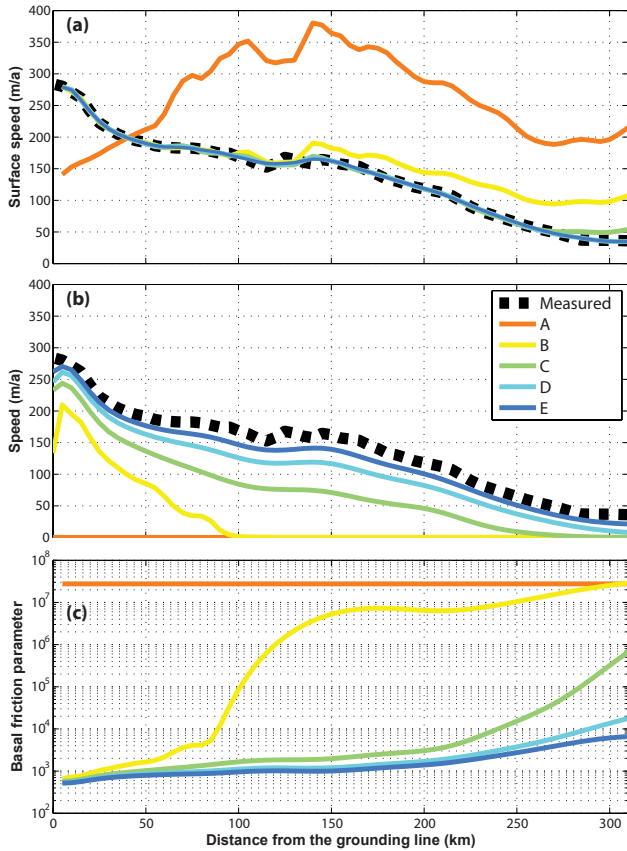


Fig. 5. (A) Observed surface flow speed (dashed black line) and optimized surface flow speed profiles along the central flowline of West Ragnhild Glacier; (B) Basal ice flow speed according to the optimization and compared to the satellite-observed surface flow speed (as in panel A); (C) Basal friction β^2 along the flowline.

order to minimize the misfit between modelled and observed velocities (MacAyeal, 1992, 1993; Arthern et al., 2010).

As a forward model we apply a simple ice flow model to calculate the ice flow field along the central flowline of Western Ragnhild Glacier, based on the shallow-ice approximation (SIA). In the vertically integrated case, the SIA surface velocity ($u(s)$) is then given by

$$u(s) = u(b) + \frac{2\bar{A}}{n+1} H |\tau_d|^{n-1} \tau_d, \quad (7)$$

where $\tau_d = -\rho g H \frac{\partial s}{\partial x}$ is the driving stress, and $u(b) = \beta^{-2} \tau_d$ is the basal velocity according to a viscous sliding law (Patyn et al., 2008). Other parameters in Eq. (7) are \bar{A} and $n = 3$, the vertically integrated temperature-dependent flow parameter and the exponent in Glen's flow law, respectively; β is the basal friction, ρ is the ice density, g is the gravitational acceleration, H is the ice thickness, and s is the surface elevation. For a flowline stretching from the ice divide (Dome Fuji) to the grounding line, boundary conditions for Eq. (7) are a zero upstream velocity and a fixed surface velocity at

the edge of our profile of $u = 300 \text{ m yr}^{-1}$, according to observations.

Since an SIA model does not take into account longitudinal stress gradients, spurious high-frequency variability in the velocity field is to be expected when the surface of the ice sheet is not supposed to relax to the imposed stress field. Especially small variations in surface slope may lead to a large variability in velocity, due to its dependence on the power of n . To prevent this, surface gradients are calculated over a distance of several ice thicknesses (Kamb and Echelmeyer, 1986; Rabus and Echelmeyer, 1997).

The main unknown in Eq. (7) is the basal velocity field, which is initialized with a high value of basal friction ($\beta^2 = 10^7$), corresponding to conditions of ice frozen to the bed. We then invoke an optimization procedure to determine the spatial distribution of β^2 so that the modelled surface velocity (u_s^m) matches the observed one (u_s^o). This is formulated as a least-squares problem for which we seek β^2 that minimizes the following objective function:

$$J(\hat{\beta}^2) = \sum_{i=1}^{n_o} \|u_s^o(i) - u_s^m(\hat{\beta}^2, i)\|^2. \quad (8)$$

The minimization problem is solved in a vector-valued approach. The vector containing the squared errors of the basal velocity mismatch is provided to the algorithm that calculates the flow field according to Eq. (7). The error vector is used to compute a preconditioned conjugate gradient (computed numerically using small variations in β^2 along the flowline). The subspace trust region method based on the interior-reflective Newton method (trust-region-reflective algorithm) described by Coleman and Li (1994, 1996) then determines the modified β^2 -profile for the next iteration. The iterations stop when the change in $J(\hat{\beta}^2)$ is below an arbitrarily small threshold.

We add two constraints to β^2 . It has to be positive and, as we expect the basal friction pattern to be continuous in space (i.e. $u(b)$ is continuously differentiable), the spatial pattern is expressed in terms of summations of Legendre polynomials. Such polynomials have the interesting property that they form an orthogonal basis and lead to a better conditioning of the nonlinear optimization problem, thus necessitating fewer iterations to converge to the optimal solution. We use these polynomials to describe the spatial distribution of β^2 along the flowline. We use polynomials up to degree 35. At this stage, we reach convergence, which means that increasing the polynomial degree does not reduce the error function any further.

The surface and bed topography within the survey domain are taken from our data. Beyond this domain, bed and surface topography are taken from both BEDMAP (Lythe et al., 2001) and Bamber et al. (2009). The resulting profile is similar to the one resampled directly from BEDMAP2 (Fretwell et al., 2013), since our ice thickness data have been included. Short gaps within the retrieved bed echoes are

linearly interpolated; the length of such gaps is typically less than several ice thicknesses, so that the large-scale flow fields are hardly affected by this choice. Longer gaps (> 10 km) were interpolated in the same way. Bed topography uncertainties associated with the longer data gaps introduces flow speed uncertainties in the most upstream area and are sufficiently far away from our region of interest.

6.2 Results

To correct for the unknown deformational velocity, we performed the optimization procedure for different values of the vertically integrated flow parameter \bar{A} . Each of the values corresponds to mean ice temperatures of -2 , -4 , -5 , -10 and -15 °C (Cuffey and Paterson, 2010). Amongst the five different flow parameters depicted in Fig. 5, case A corresponds to the warmest (softest) ice (-2 °C), and predicts higher ice flow speeds due to ice deformation along the whole flowline compared to the observed ones. For this value, the optimization procedure fails, as the model cannot allow “negative” basal velocities. Not only is the ice too soft (hence flows too fast), the pattern of the deformational velocity does not match the observed velocity profile.

Cases B to E reveal a good match of the modelled velocities with the observed ones. For each decrement in ice temperature, the ice gets stiffer and the amount of basal sliding along the profile becomes more important. Therefore, cases D and E correspond to much colder (stiffer) ice (-10 and -15 °C, respectively) and predict deformational velocities that are too small, so that basal sliding takes up the majority of the velocity along the profile.

The corresponding pattern of β^2 is, with the exception of case A, very similar for all simulations: it reveals a relatively high friction inland and a low friction in the area 100 km upstream from the grounding line. Over the upstream section of the longitudinal profile, ice motion is essentially governed by internal deformation. All experiments show that basal motion is dominant only in the downstream region.

7 Discussion and conclusions

Prior to our study, only two glaciers were considered as important contributors to the discharge of ice from DML, i.e. Jutulstraumen and Shirase Glacier, and both have been the subject of more interest in the past (e.g. Høydal, 1996; Pattyn and Derauw, 2002). Despite their fast flow (the grounding line velocity of Shirase Glacier is > 2000 m yr^{-1}), they each discharge approximately 10 % of the total snow accumulation of this part of the ice sheet (Rignot et al., 2008). Both glaciers are topographically constrained and characterized by a highly convergent flow regime. They also terminate in a relatively narrow trunk. From an ice-dynamical viewpoint, Shirase Glacier is a relatively stable feature, as its grounding line cannot retreat over a distance larger than 5 to 10 km, since the

bedrock rapidly rises above sea level from the present position of the grounding line (Pattyn, 1996, 2000; Pattyn and Derauw, 2002). Such conditions make an outlet glacier less prone to dynamic grounding line retreat and significant mass loss due to dynamic changes in the ice shelf.

Taking into consideration West Ragnhild Glacier definitely changes the discharge picture in DML. Indeed, based on the thickness data across the grounding line in conjunction with satellite-observed ice flow velocities, its discharge (13 – 14 Gt yr^{-1}) is comparable to the discharge of Jutulstraumen and Shirase Glacier. Nonetheless, the ice flow velocities of West Ragnhild Glacier are relatively low. Ice flow speed is > 100 m yr^{-1} at 100 km upstream of the grounding line and up to 250 m yr^{-1} at the grounding line (Fig. 1). The reason for such low values is ice shelf buttressing by two major ice rises within the Roi Baudouin Ice Shelf, slowing down the flow upstream. While according to Rignot et al. (2008), the area seemed to be in balance, a significant imbalance is currently observed in the grounding zone of West Ragnhild Glacier and along the grounding line of the Roi Baudouin Ice Shelf (Rignot et al., 2013), which is in line with direct observations (Pattyn et al., 2012).

Despite present-day stable conditions, the analysis presented in this paper clearly demonstrates that West Ragnhild Glacier (i) is an important outlet glacier, (ii) is marine terminating with a grounding line 600–700 m b.s.l., and (iii) has a downstream section that is smooth, sediment covered and water saturated in the downstream area. Beside data evidence, inverse modelling allows the conclusion that decreasing basal friction leads to an increasing basal velocity towards the grounding line. Using two different kinds of evidence, we demonstrate that the bed/ice interface plays a dominant role in the acceleration of West Ragnhild Glacier toward the grounding line.

Given the fact that the smooth bed is also flat and horizontal and devoid of distinct lateral constraints, the grounding line is potentially capable of advancing and retreating across a substantial area. According to theoretical considerations (Schoof, 2007), a grounding line retreat may be expected if sudden changes occur at the seaward side. The close proximity of the DML ice shelves to the margin of the continental shelf (Timmermann et al., 2010, and Fig. 1a) could potentially allow relatively warm water from the abyssal plains to circulate under the shelf, leading to significant sub-shelf melting (e.g. Smedsrud et al., 2006). Unpinning of the ice shelf could therefore lead to grounding line retreat due to increased flow speed, hence increased dynamic mass loss, in line with recent observations (Rignot et al., 2013). New geophysical data presented in this paper highlight such a possibility in West Ragnhild Glacier.

Acknowledgements. The radar survey was conducted by the Alfred Wegener Institute with further logistical support from the Princess Elisabeth Station (Belgian Antarctic Research Expedition, BELARE), and funded by the European Facilities for Airborne Research (EUFAR). D. Callens is funded through a FNRS-FRIA fellowship (Fonds de la Recherche Scientifique) and received an Yggdrasil mobility grant (Research Council of Norway). This work is in part supported by the Centre for Ice, Climate and Ecosystems (ICE) at the Norwegian Polar Institute.

Edited by: C. R. Stokes

References

- Arthern, R. J. and Gudmundsson, G. H.: Initialisation of Ice-Sheet Forecasts viewed as an Inverse Robin Problem, *J. Glaciol.*, 56, 527–533, 2010.
- Bamber, J. L., Gomez-Dans, J. L., and Griggs, J. A.: A new 1 km digital elevation model of the Antarctic derived from combined satellite radar and laser data – Part 1: Data and methods, *The Cryosphere*, 3, 101–111, doi:10.5194/tc-3-101-2009, 2009.
- Bindschadler, R. A., Choi, H., and ASAID Collaborators: High-Resolution Image-derived Grounding and Hydrostatic Lines for the Antarctic Ice Sheet, Digital media, National Snow and Ice Data Center, Boulder, Colorado, USA, 2011.
- Bingham, R. G. and Siegert, M. J.: Quantifying subglacial bed roughness in Antarctica: implications for ice-sheet dynamics and history, *Quaternary Sci. Rev.*, 28, 223–236, 2009.
- Coleman, T. and Li, Y.: On the Convergence of Reflective Newton Methods for Large-Scale Nonlinear Minimization Subject to Bounds, *Math. Program.*, 67, 189–224, 1994.
- Coleman, T. and Li, Y.: An Interior, Trust Region Approach for Nonlinear Minimization Subject to Bounds, *SIAM J. Optimiz.*, 6, 418–445, 1996.
- Cuffey, K. and Paterson, W. S. B.: *The Physics of Glaciers*, 4th Edn., Elsevier, New York, 2010.
- Fretwell, P., Pritchard, H. D., Vaughan, D. G., Bamber, J. L., Bartrand, N. E., Bell, R., Bianchi, C., Bingham, R. G., Blankenship, D. D., Casassa, G., Catania, G., Callens, D., Conway, H., Cook, A. J., Corr, H. F. J., Damaske, D., Damm, V., Ferraccioli, F., Forsberg, R., Fujita, S., Gim, Y., Gogineni, P., Griggs, J. A., Hindmarsh, R. C. A., Holmlund, P., Holt, J. W., Jacobel, R. W., Jenkins, A., Jokat, W., Jordan, T., King, E. C., Kohler, J., Krabill, W., Riger-Kusk, M., Langley, K. A., Leitchenkov, G., Leuschen, C., Luyendyk, B. P., Matsuoka, K., Mouginot, J., Nitsche, F. O., Nogi, Y., Nost, O. A., Popov, S. V., Rignot, E., Rippin, D. M., Rivera, A., Roberts, J., Ross, N., Siegert, M. J., Smith, A. M., Steinhage, D., Studinger, M., Sun, B., Tinto, B. K., Welch, B. C., Wilson, D., Young, D. A., Xiangbin, C., and Zirizzotti, A.: Bedmap2: improved ice bed, surface and thickness datasets for Antarctica, *The Cryosphere*, 7, 375–393, doi:10.5194/tc-7-375-2013, 2013.
- Høydal, Ø. A.: A force-balance study of ice flow and basal conditions of Jutulstraumen, Antarctica, *J. Glaciol.*, 42, 413–425, 1996.
- Joughin, I.: Ice-sheet velocity mapping: a combined interferometric and speckle-tracking approach, *Ann. Glaciol.*, 34, 195–201, 2002.
- Joughin, I., Rignot, E., Rosanova, C. E., Lucchitta, B. K., and Bohlander, J.: Timing of Recent Accelerations of Pine Island Glacier, Antarctica, *Geophys. Res. Lett.*, 30, 1706, doi:10.1029/2003GL017609, 2003.
- Kamb, B. and Echelmeyer, K. A.: Stress-gradient Coupling in Glacier Flow: 1. Longitudinal Averaging of the Influence of Ice Thickness and Surface Slope, *J. Glaciol.*, 32, 267–298, 1986.
- Lythe, M. B., Vaughan, D. G., and BEDMAP consortium: BEDMAP: a new ice thickness and subglacial topographic model of Antarctica, *J. Geophys. Res.*, 106, 11335–11351, 2001.
- MacAyeal, D. R.: The basal stress distribution of Ice Stream E, Antarctica, inferred by control methods, *J. Geophys. Res.*, 97, 595–603, 1992.
- MacAyeal, D. R.: A Tutorial on the Use of Control Methods in Ice-Sheet Modeling, *J. Glaciol.*, 39, 91–98, 1993.
- MacGregor, J. A., Winebrenner, D. P., Conway, H., Matsuoka, K., Mayewski, P. A., and Clow, G. D.: Modeling englacial radar attenuation at Siple Dome, West Antarctica, using ice chemistry and temperature data, *J. Geophys. Res.*, 112, F03008, doi:10.1029/2006JF000717, 2007.
- Matsuoka, K.: Pitfalls in radar diagnosis of ice-sheet bed conditions: Lessons from englacial attenuation models, *Geophys. Res. Lett.*, 38, L05505, doi:10.1029/2010GL046205, 2011.
- Matsuoka, K., MacGregor, J. A., and Pattyn, F.: Predicting radar attenuation within the Antarctic ice sheet, *Earth Planet. Sc. Lett.*, 359–360, 173–183, 2012.
- Miles, B. W. J., Stokes, C. R., Vieli, A., and Cox, N. J.: Rapid, climate-driven changes in outlet glaciers on the Pacific coast of East Antarctica, *Nature*, 500, 563–566, 2013.
- Nixdorf, U., Steinhage, D., Meyer, U., Hempel, L., Jenett, M., Wachs, P., and Miller, H.: The newly developed airborne radio-echo sounding system of the AWI as a glaciological tool, *Ann. Glaciol.*, 29, 231–238, 1999.
- Pattyn, F.: Numerical modelling of a fast-flowing outlet glacier: experiments with different basal conditions, *Ann. Glaciol.*, 23, 237–246, 1996.
- Pattyn, F.: Ice-sheet modelling at different spatial resolutions: focus on the grounding line, *Ann. Glaciol.*, 31, 211–216, 2000.
- Pattyn, F.: Transient glacier response with a higher-order numerical ice-flow model, *J. Glaciol.*, 48, 467–477, 2002.
- Pattyn, F.: A New 3D Higher-Order Thermomechanical Ice-Sheet Model: Basic Sensitivity, Ice-Stream Development and Ice Flow across Subglacial Lakes, *J. Geophys. Res.*, 108, B82382, doi:10.1029/2002JB002329, 2003.
- Pattyn, F. and Derauw, D.: Ice-dynamic conditions of Shirase Glacier, Antarctica, inferred from ERS-SAR interferometry, *J. Glaciol.*, 48, 559–565, 2002.
- Pattyn, F., Perichon, L., Aschwanden, A., Breuer, B., de Smedt, B., Gagliardini, O., Gudmundsson, G. H., Hindmarsh, R. C. A., Hubbard, A., Johnson, J. V., Kleiner, T., Kononov, Y., Martin, C., Payne, A. J., Pollard, D., Price, S., Rückamp, M., Saito, F., Souček, O., Sugiyama, S., and Zwinger, T.: Benchmark experiments for higher-order and full-Stokes ice sheet models (ISMIP-HOM), *The Cryosphere*, 2, 95–108, doi:10.5194/tc-2-95-2008, 2008.
- Pattyn, F., Matsuoka, K., Callens, D., Conway, H., Depoorter, M., Docquier, D., Hubbard, B., Samyn, D., and Tison, J. L.: Melting and refreezing beneath Roi Baudouin Ice Shelf (East Antarctica)

- inferred from radar, GPS, and ice core data, *J. Geophys. Res.*, 117, F04008, doi:10.1029/2011JF002154, 2012.
- Pritchard, H. D., Ligtenberg, S. R. M., Fricker, H. A., Vaughan, D. G., van den Broeke, M. R., and Padman, L.: Antarctic ice-sheet loss driven by basal melting of ice shelves, *Nature*, 484, 502–505, doi:10.1038/nature10968, 2012.
- Rabus, B. T. and Echelmeyer, K. A.: The Flow of a Polythermal Glacier: McCall Glacier, Alaska, U.S.A., *J. Glaciol.*, 43, 522–536, 1997.
- Rapp, R. H.: Use of potential coefficient models for geoid undulation determinations using a spherical harmonic representation of the height anomaly/geoid undulation difference, *J. Geodesy*, 71, 282–289, 1997.
- Rignot, E., Bamber, J. L., van den Broeke, M. R., Davis, C., Li, Y., van de Berg, W. J., and van Meijgaard, E.: Recent Antarctic ice mass loss from radar interferometry and regional climate modelling, *Nat. Geosci.*, 1, 106–110, 2008.
- Rignot, E., Mouginot, J., and Scheuchl, B.: Ice flow of the Antarctic ice sheet, *Science*, 333, 1427–1430, 2011a.
- Rignot, E., Mouginot, J., and Scheuchl, B.: MEASUREs Antarctic Grounding Line from Differential Satellite Radar Interferometry, NASA EOSDIS Distributed Active Archive Center at NSIDC, Boulder, Colorado, USA, Digital media, 2011b.
- Rignot, E., Jacobs, S., Mouginot, J., and Scheuchl, B.: Ice shelf melting around Antarctica, *Science*, 314, 266–270, 2013.
- Rippin, D. M., Vaughan, D. G., and Corr, H. F. J.: The basal roughness of Pine Island Glacier, West Antarctica, *J. Glaciol.*, 57, 67–76, 2011.
- SCAR: Scientific Committee on Antarctic Research Antarctic Digital Database, available at: <http://www.add.scar.org> (last access: 6 July 2012), digital media, 2012.
- Schoof, C.: Ice sheet grounding line dynamics: steady states, stability and hysteresis, *J. Geophys. Res.*, 112, F03S28, doi:10.1029/2006JF000664, 2007.
- Schoof, C.: Glaciology: beneath a floating ice shelf, *Nat. Geosci.*, 3, 450–451, 2010.
- Shepherd, A., Ivins, E. R., Geruo, A., Barletta, V. R., Bentley, M. J., Bettadpur, S., Briggs, K. H., Bromwich, D. H., Forsberg, R., Galin, N., Horwath, M., Jacobs, S., Joughin, I., King, M. A., Lenaerts, J. T. M., Li, J., Ligtenberg, S. R. M., Luckman, A., Luthcke, S. B., McMillan, M., Meister, R., Milne, G., Mouginot, J., Muir, A., Nicolas, J. P., Paden, J., Payne, A. J., Pritchard, H., Rignot, E., Rott, H., Sandberg Sørensen, L., Scambos, T. A., Scheuchl, B., Schrama, E. J. O., Smith, B., Sundal, A. V., van Angelen, J. H., van de Berg, W. J., van den Broeke, M. R., Vaughan, D. G., Velicogna, I., Wahr, J., Whitehouse, P. L., Wingham, D. J., Yi, D., Young, D., and Zwally, H. J.: A reconciled estimate of ice-sheet mass balance, *Science*, 338, 1183–1189, 2012.
- Smedsrud, L. H., Jenkins, A., Holland, D. M., and Nøst, O. A.: Modeling ocean processes below Fimbulisen, Antarctica, *J. Geophys. Res.*, 111, C01007, doi:10.1029/2005JC002915, 2006.
- Steinhage, D., Nixdorf, U., Meyer, U., and Miller, H.: Subglacial topography and internal structure of central and western Dronning Maud Land, Antarctica, determined from airborne radio echo sounding, *J. Appl. Geophys.*, 47, 183–189, 2001.
- Taylor, J., Siegert, M., Payne, A., and Hubbard, B.: Regional-scale bed roughness beneath ice masses: measurement and analysis, *Comput. Geosci.*, 30, 899–908, 2004.
- Timmermann, R., Le Brocq, A., Deen, T., Domack, E., Dutrieux, P., Galton-Fenzi, B., Hellmer, H., Humbert, A., Jansen, D., Jenkins, A., Lambrecht, A., Makinson, K., Niederjasper, F., Nitsche, F., Nøst, O. A., Smedsrud, L. H., and Smith, W. H. F.: A consistent data set of Antarctic ice sheet topography, cavity geometry, and global bathymetry, *Earth Syst. Sci. Data*, 2, 261–273, doi:10.5194/essd-2-261-2010, 2010.

Marine ice deformation experiments: an empirical validation of creep parameters

Marie Dierckx¹ and Jean-Louis Tison¹

Received 10 October 2012; revised 7 December 2012; accepted 11 December 2012; published 16 January 2013.

[1] Marine ice is increasingly recognized as an important component of ice shelves in Antarctica. Because it mainly accretes in “weak” locations, it plays a crucial role in ice shelf stability. Little is known however on the rheology of this particular material (low salinity, no bubbles, specific fabrics). We present marine ice deformation experiments in unconfined uniaxial compression at -10°C , -6°C , and -3°C . Generally, marine ice samples confirm the value of $n=3$ for Glen’s power law. It also appears to behave systematically “harder” than artificial or meteoric isotropic ice samples used in the past, in the studied stress condition. Bulk salinity does not seem to have a significant impact on the viscosity. All deformation curves compare well with a generalized empirical temperature/viscosity relationship. They represent the first experimental validation of the lower boundary of this rheological relationship recommended for use in modeling ice dynamics. **Citation:** Dierckx, M., and J.-L. Tison (2013), Marine ice deformation experiments: an empirical validation of creep parameters, *Geophys. Res. Lett.*, 40, 134–138, doi:10.1029/2012GL054197.

1. Introduction

[2] Ice shelves play a major role in the global stability of Antarctica in that they regulate the ice flux from the continent to the ocean. Marine ice is increasingly recognized as an important contributor to the ice shelf mass around Antarctica. It results from the consolidation of loose frazil ice forming under supercooling in the outflowing Ice Shelf Water branch of the Deep Thermohaline Circulation, a feature of ocean circulation in sub-ice shelf cavities [Jacobs *et al.*, 1992]. It accretes, generally rapidly and in large amounts [Morgan, 1972; Oerter *et al.*, 1992; Eicken *et al.*, 1994; Khazendar and Jenkins, 2003; Jansen *et al.*, 2012], in all the “weak” points of the ice shelf such as bottom crevasses at the grounding line, suture zone between individual ice streams feeding into the ice shelf, frontal rifts, and sides of pinning points. It then slowly consolidates under the conductive heat flux towards the colder atmosphere (the ice shelf surface). By nature, and regardless of its rheology, marine ice is therefore a good candidate for stabilizing the ice shelf flow. Several studies have described marine ice properties and compared it to the meteoric ice formed through snow metamorphism on

the continent [Moore *et al.*, 1994; Oerter *et al.*, 1994; Souchez *et al.*, 1995; Tison *et al.*, 1998; Khazendar *et al.*, 2001; Treverrow *et al.*, 2010, and references therein]. The sample properties differ significantly: marine ice is 2 orders of magnitude more saline than meteoric ice (but also 2 orders of magnitude less saline than sea ice), shows a positive $\delta^{18}\text{O}$ signature because it is formed from the freezing of sea water, is devoid of bubbles, and can contain solid inclusions of marine or detritic origin. As can be expected, marine ice presents a whole range of ice fabrics (optic axes orientation) from random to highly oriented. This suggests that besides its “welding” role, marine ice could also impact ice shelf rheology because of its specific properties.

[3] Using inverse modeling, Khazendar *et al.* [2009] has concluded that potential locations of marine ice accretion show lower inferred viscosities, suggesting marine ice deforms faster than meteoric ice. In recent work where they study grain size, texture, and ice fabrics of marine ice in the Amery Ice Shelf, Treverrow *et al.* [2010] suggested that compression experiments be performed on marine ice to characterize its rheological properties. Preliminary tests have already been initiated by Samyn *et al.* [2007] and Dierckx *et al.* [2010] in that respect, but a detailed experimental study is still lacking.

[4] Because of its crucial importance in ice dynamics modeling, much attention has been given to the value of the creep parameter A in Glen’s flow law for ice deformation (equation (1)) [Glen, 1958].

$$\dot{\epsilon} = A\sigma^n \quad (1)$$

[5] In their recent synthesis of prior research [for example, Budd and Jacka, 1989], Cuffey and Paterson [2010] concluded that for practical applications, the parameter A should be dissociated into an effect of the temperature field (Arrhenius law) and effects of intrinsic material properties such as grain size, c axis orientation fabric, impurities, and water content. Their relationship is shown in equation (2),

$$\begin{aligned} \dot{\epsilon}_{jk} &= AE_*\tau_E^{n-1}\sigma'_{jk} \\ A &= A_*\exp\left(-\frac{Q_c}{R}\left[\frac{1}{T_h} - \frac{1}{T_r}\right]\right) \\ \text{with } \tau_E^2 &= \frac{1}{2}\sum_{j,k}(\sigma'_{jk})^2 \\ \text{and } \sigma'_{jj} &= \sigma_{jj} - \frac{1}{3}(\sigma_{ii} + \sigma_{jj} + \sigma_{kk}) \end{aligned} \quad (2)$$

where $\dot{\epsilon}$ is the deformation rate, A the creep parameter, E_* the enhancement factor that takes into account the combined effect of all intrinsic factors, τ_E the effective shear stress, σ' the deviatoric stress (the crossed terms are zero on uniaxial compression), σ the normal stress component, A_* the constant prefactor (the value of A at the reference temperature $T_* = -10^{\circ}\text{C}$), Q_c [Jmol^{-1}] the activation energy for creep, R the universal gas constant, and T_h the pressure dependent

¹Laboratoire de Glaciologie, CP 160/03, Université Libre de Bruxelles, Bruxelles, Belgium.

Corresponding author: Marie Dierckx, Laboratoire de Glaciologie, Département des Sciences de la Terre et de l’Environnement, Université Libre de Bruxelles, CP 160/03, Avenue F.D. Roosevelt 50, B-1050 Brussels, Belgium. (mdierckx@ulb.ac.be)

temperature in Kelvin [Hooke, 1998; Schulson and Duval, 2009; Cuffey and Paterson, 2010]. The octahedral shear stress that will be used in this paper, is defined by $2\tau_E^2 = 3\tau_{\text{oct}}^2$. Considering ice shelf meteoric ice as the best equivalent of typical isotropic meteoric ice ($E^* = 1$), these authors use its observed/ modeled mean A value at -10°C ($A = 3.510 \cdot 10^{-25} \text{ s}^{-1} \text{ Pa}^{-3}$) as the reference value for A^* (with $n = 3$). While field and experimental measurements agree on a value of $Q_c = 60 \text{ kJ mol}^{-1}$ for the activation energy if $T_h < T^*$, they select $Q_c = 115 \text{ kJ mol}^{-1}$ for the temperature range $[-10^\circ\text{C} \text{ to } 0^\circ\text{C}]$ [Weertman, 1983], in order to match the results of inverse modeling of the flow of temperate glaciers. The authors [Cuffey and Paterson, 2010] then recommend different values for the enhancement factor, ranging from 1 to 5, depending of the grain size, impurity content, fabric, etc. Equation (2) presents the advantage of separating the temperature and material dependent parameters A and E^* , respectively.

[6] In this paper, we investigate the rheological properties of marine ice samples originating from the Nansen Ice Shelf (Ross Sea, Antarctica) [Khazendar et al., 2001; Tison and Khazendar, 2001], across the $[-10^\circ\text{C} \text{ to } -3^\circ\text{C}]$ temperature range under vertical compression in unconfined conditions and compare them with both results from artificial and natural isotropic ice (referred here as clean ice) deformation in a similar stress setting [Jacka, 1984; Budd and Jacka, 1989; Jacka and Li, 1994] and predictions from the above described empirical relationship (equation (2)) of Paterson [1994] and Cuffey and Paterson [2010].

2. Site Description

[7] The Nansen Ice Shelf (NIS) is located in Terra Nova Bay, Victoria Land, East Antarctica [Khazendar, 2000; Khazendar et al., 2001; Tison and Khazendar, 2001]. Here marine ice forms in rifts opening throughout the entire ice shelf thickness (few hundred meters) at the grounding line and downstream, outcrops at the ice shelf surface, due to net ablation from severe katabatic wind regimes. Two 45 m ice cores have been collected during the 1995–1996 austral summer in the framework of a Belgo-Italian drilling program. The two ice cores were located along a central flow line of the ice shelf at, respectively, 7.5 km (NIS1 – $74^\circ 51' \text{ S } 162^\circ 50' \text{ E}$) and 24.5 km (NIS2 – $75^\circ 00' \text{ S } 163^\circ 06' \text{ E}$) downstream from the grounding line. All cores had a diameter of 8 cm and were collected with an electro-mechanical (SIPRE-type) ice corer.

3. Experiments and Results

[8] A selection of 10 marine ice samples has been chosen from the NIS1 and NIS2 marine ice cores. Samples were shaped as cylinder of ≈ 3.5 cm diameter and ≈ 7 cm tall. Physical properties along the length of the cores were examined with thin sections following the conventional procedure of Langway [1958] and analyzed for texture and fabric using a G50 LED-White Automated Fabric Analyzer [Russell-Head and Wilson, 2001; Wilson et al., 2003]. The salinity of each sample was deduced from Cl^- anion determination, using HPLC (Dionex 100) measurements (precision $\leq 4\%$). Assuming that the Cl^- /salinity ratio does not change during formation or melting, bulk ice salinity is deduced from the mean Cl^- /salinity ratio in sea water (19.35/35) [Sarmiento and Gruber, 2006]. Although this is clearly an approximation with limited accuracy (0.03 ± 0.0012 to 0.3 ± 0.012), we consider it as sufficient for the purpose of this paper.

[9] We aimed to select samples with ice fabrics as close as possible to a random crystal orientation distribution. The salinity range usually encountered in marine ice (0.03 to 0.3) [e.g., Tison et al., 1993; Tison and Khazendar, 2001] allows us to test the contribution of the salinity to the enhancement factor E^* . Finding marine ice with an isotropic fabric was a significant challenge, given the specific setting of the NIS marine ice outcrops, prone to develop sustained folding [see Khazendar et al., 2001]. Figure 1 shows two examples of textures and fabrics from the NIS1 core. Most of the selected samples showed crystallographic properties similar to sample NIS1-59c, i.e., a fabric reasonably close to random. A few samples had however to be selected in more oriented ice (eigenvector S1 close to 0.77, Figure 1), such as sample NIS1-82b, with sub-vertical folds and crystal elongation.

[10] Samples of low (min 0.027) and high (max 0.234) bulk salinities were chosen for each of the selected temperatures, as shown in Table 1. The experimental temperatures were designed to adequately cover the usual range of observed temperatures within ice shelves [e.g., Zotikov, 1986]. The grain size was homogeneous between samples, with a mean value of 1.65 mm^2 .

[11] The samples were deformed in unconfined uniaxial compression using the pneumatic device developed at the Laboratoire de Glaciologie of the Université Libre de Bruxelles and described in details by Samyn et al. [2011]. As in previous studies, the aim of the deformation experiment is to reach the secondary creep at which the strain rate is minimal. Minimum creep is a unique point within the ice creep curve that allows for comparison between the effects of the properties of one ice type as compared to another. Each sample is submitted stepwise to an increasing stress, beginning with a stress close to 0.1 MPa and incrementing up to a maximum of 0.8 MPa. This procedure allows to keep the same sample for different applied stresses and therefore keep the same parameter “A” to analyze only the parameter “n”. At each step, the secondary creep stage is achieved, with its recorded associated minimum strain rate. It should be noted again that using secondary instead of tertiary creep means that pre-oriented fabric can play a role on the viscosity, resulting in dispersion in the data set. Combining these stepwise records in a log-log plot then allows easy representation of Glen’s flow law and deducing values for the “n” and “A” parameters. We also compared the stepwise load approach with a continuous case to check for the validity of the former. For this, sample NIS1-91b has been directly loaded to 0.67 MPa. The obtained data point perfectly fits with the determined trend.

[12] Figure 2 summarizes the results of our compression deformation tests at the three selected temperatures (red triangles). Each symbol is an experimental data point which represents the minimal strain rate at secondary creep for a given applied stress (octahedral shear stresses and strain rates are used here to ease the comparison with the other data sets) [Schulson and Duval, 2009]. The tabulated values can be found in the auxiliary material.¹ The red lines are linear fits through each of these experimental data sets. Also shown in Figure 2 are (a) previous experimental results obtained in uniaxial compression on clean ice (blue symbols) [Jacka, 1984; Budd and Jacka, 1989; Jacka and Li,

¹Auxiliary materials are available in the HTML. doi:10.1029/2012GL054197.

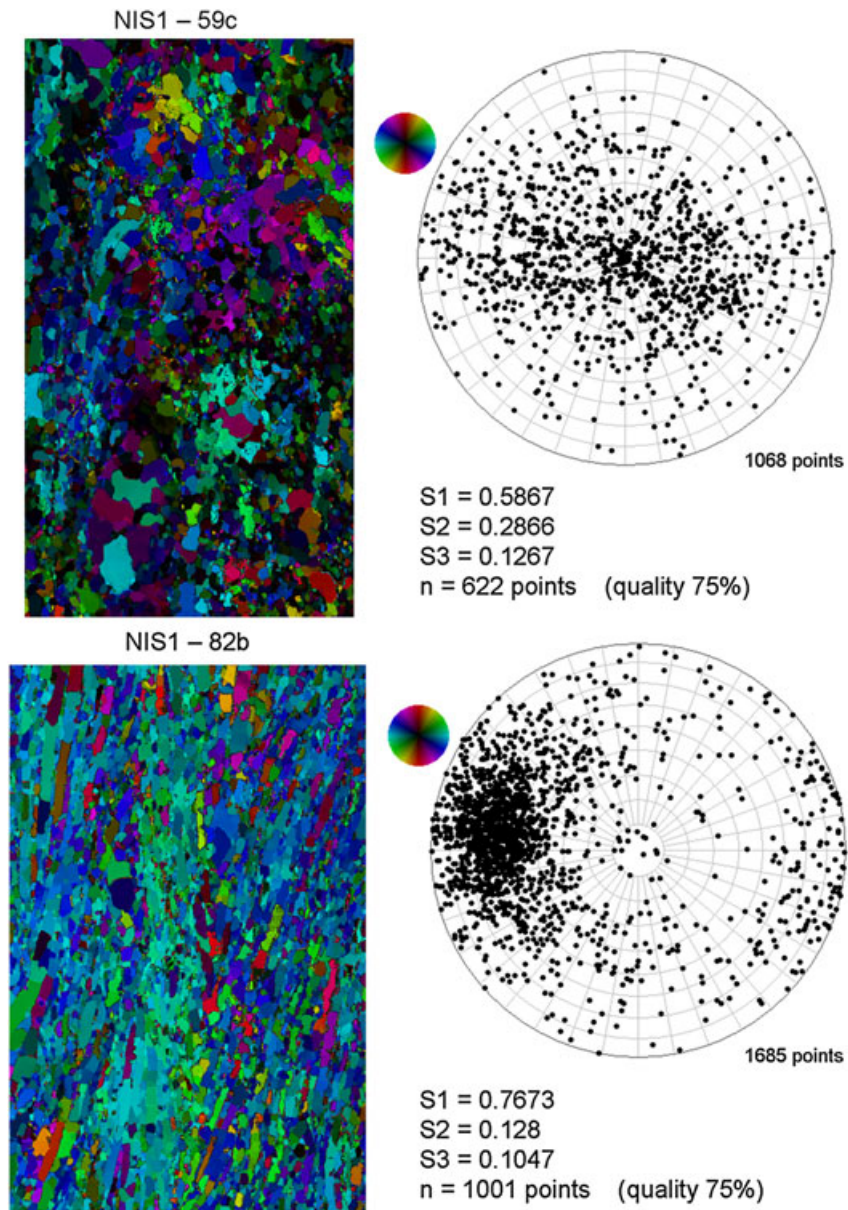


Figure 1. Typical sample fabrics before compression experiment, using an automated fabric analyzer system (G50). Thin sections are in artificial color. Sample NIS1—59c is representative of most of the marine ice samples used. A few samples show a more oriented fabric, as represented by NIS1—82b.

Table 1. Temperature and Salinity of the Marine Ice Samples

Sample ID	Experimental Temperature [°C]	Salinity [—]	Mean Grain Size [mm ²]
NIS2 53c	-3	0.234	2
NIS1 82b	-3	0.047	1.45
NIS2 96a	-3	0.055	1.9
NIS1 97d	-6	0.035	1.45
NIS1 74e	-6	0.051	1.4
NIS1 59c	-6	0.089	1.85
NIS1 91b	-6	0.057	1.5
NIS1 49b	-10	0.131	—
NIS2 53b	-10	0.224	2
NIS2 4a	-10	0.027	1.35

1994] and (b) empirical laws from Paterson [1994] (black dashed line) and Cuffey and Paterson [2010] for $E^*=1$ (black solid line).

4. Discussion

[13] The mean slope of the linear fits through our data sets is 2.93 ± 0.11 , while the equivalent value for clean ice (all temperatures, through all data) [Jacka, 1984; Budd and Jacka, 1989; Jacka and Li, 1994] is 3.29 ± 0.2 but closer to $n=3$ for each data set considered separately. This further supports the choice of $n=3$ in Glen’s flow law, for octahedral stresses ranging between 0.1 and 0.8 MPa.

[14] The variability around each marine ice trend can be explained by the crystal orientation fabric variability of the different samples. Indeed, it can be expected that some samples are harder or softer in compression compared to more isotropic samples. These effects will be discussed in detail in another paper (in preparation).

[15] Clear differences however exist between the various data sets in Figure 2 in terms of the relative position of each

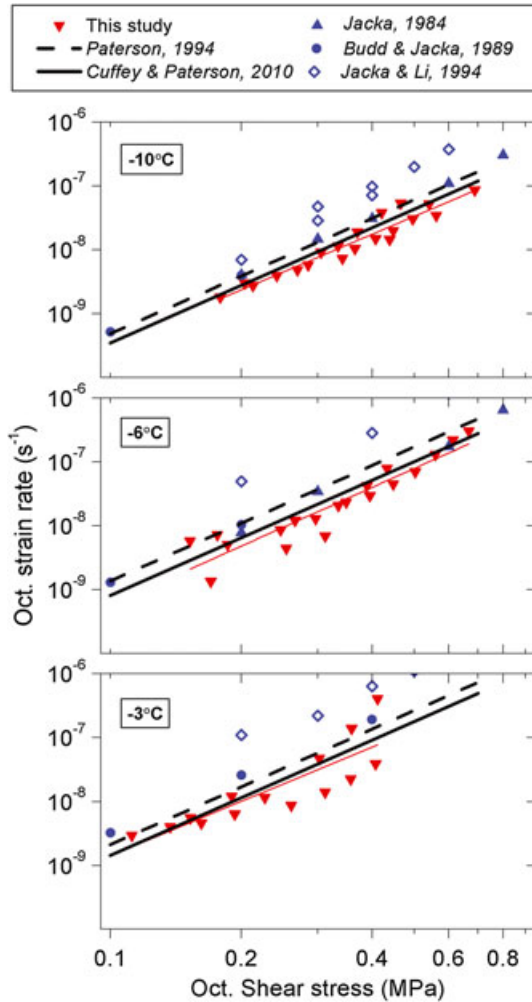


Figure 2. Comparison between this study (marine ice compression experiments, in red), clean ice compression experiments (artificial and natural isotropic ice), Jacka’s data, in blue and literature (Paterson and Cuffey empirical laws, respectively, in dashed and solid black line). The mean slope of all our linear fits is around 2.93 ± 0.11 . Marine ice data match the new calibration established by Cuffey and Paterson [2010].

trend. These differences represent the relative “softness” of the ice, as would be expressed in the enhancement factor E_* of the creep parameter A , following the approach of Cuffey and Paterson [2010]. As underlined in preliminary results from Samyn *et al.* [2007] and Dierckx *et al.* [2010], it appears that at all temperatures, marine ice samples are harder to deform than clean ice. This is therefore also the case, when compared to the relationship proposed by Paterson [1994], drawing considerably from the results of these experiments. However, the linear fits of our datasets are close to the trends of Cuffey and Paterson’s empirical law, calculated for the lower boundary case of an enhancement factor $E_* = 1$, and this throughout the whole temperature range (i.e., using the appropriate values of the activation energy, depending on the temperature range). It therefore appears that marine ice recently consolidated into ice shelves provides an excellent natural example of isotropic ice with minimal viscosity. Our new data set also offers experimental validation of the lower boundary of Cuffey and Paterson [2010] relationship throughout the temperature range, for stresses greater than 0.1 MPa. It follows that isotropic marine

ice does not deform specifically harder than other ice types but rather represents the lower boundary for natural ice deformation, with an enhancement factor equal to 1.

[16] As discussed above, none of the chosen samples has a truly isotropic c axes distribution, which might explain part of the spread of our data points around Cuffey and Paterson’s relationship in Figure 2. These excursions are worth considering further in terms of potential other drivers. A wide range of solid and soluble impurity contents has been described in the marine or meteoric ice literature [e.g., Jones and Glen, 1969; Oerter *et al.*, 1992; Tison *et al.*, 1993; Moore *et al.*, 1994; Trickett *et al.*, 2000; Khazendar *et al.*, 2001; Treverrow *et al.*, 2010], and these can also potentially affect the E_* value. Even though our samples covered a relatively large salinity range, no significant systematic deviation could be isolated in the studied range of temperature and stresses. It therefore seems likely that the soluble impurity content plays a negligible role in the enhancement factor for the whole documented range of marine ice samples. Differences in the concentration or granulometry of the solid impurity content could also be responsible for some deviations in our data set, but this factor could not be quantified in the present study. The ice grain size is shown to be homogeneous within our samples set and cannot therefore be held responsible for the dispersion of the data. Finally, the higher spread is observed at -3°C , indicating a much higher sensitivity to sample and/or experimental conditions at warmer temperatures.

[17] It is also important to underline that our experimental data set covers the range of 0.1 to 0.8 MPa for applied stresses. This is probably a higher boundary for vertical deviatoric stresses in the central part of ice shelves (away from lateral friction, ice streams convergence, rifts, and crevasses suturing). This perspective is important in view of results from the deformation behavior of meteoric ice at low stresses [see, e.g., Montagnat and Duval, 2004; Schulson and Duval, 2009, and references therein], where the n parameter of Glen’s flow law is different and closer to 2. Similarly, it is possible that the response of the E_* parameter to its driving factors might also differ at low stress. It should therefore be beneficial to run further marine ice deformation experiments at very low stress, to extend the validity of the present data set.

5. Conclusion

[18] We have presented here the first comprehensive set of unconfined uniaxial compression experiments on marine ice samples in a range of temperatures (-10°C to -3°C) that is coherent with those encountered in ice shelves. Our initial goal was to figure out how the specific intrinsic properties of marine ice might affect its rheological behavior and eventually corroborate findings from inverse modeling suggesting that marine ice is indeed softer than meteoric ice. Comparing our data set to the results from previous studies working with artificial and natural isotropic ice initially led us to the opposite conclusion, i.e., that marine ice is actually harder to deform than meteoric ice, in the studied stress condition. However, new developments on the calibration of the creep parameter in ice rheology also predict a harder than previously believed behavior for isotropic ice with an enhancement factor equal to unity [Cuffey and Paterson, 2010]. We show that our data set demonstrates the validity of this relationship and that newly formed marine ice can be considered as the lower boundary of the possible viscosities for natural isotropic ice across the

temperature range. This therefore suggests that the lower viscosities invoked for marine ice in inverse modeling exercises mainly results from changes in the temperature field (warmer marine ice embedded in colder meteoric ice) rather than in a specific enhancement factor resulting from the intrinsic properties of marine ice. Theoretical considerations and field observations [e.g., Craven *et al.*, 2009] indeed show that temperature profiles considerably depart from the expected linear gradient when marine ice bottom accumulation occurs below meteoric ice in significant amounts. Bulk salinity does not seem to play a major role in marine ice rheology, in the studied stress condition. However, no impurity specific study has been made. The impurity content may still influence the ice deformation and explain part of the enhancement factor. The role of the development of strong orientation fabrics resulting from folding structures, of the grain size and of solid inclusions often encountered in marine ice cores, still remains to be explored in further deformation tests.

[19] Marine ice is often mistaken for what is referred to as the “ice mélange” in rifts and open crevasses at the surface of the ice shelf. Marine ice is indeed only one potential component of the “ice mélange” which is a composite of various ice types such as fallen meteoric ice blocks, sea ice or snow, and firn, with an expected lower homogeneity and coherence. This difference in filling materials could be responsible for the contrasts in the rheological behavior of rifted areas in ice shelves, as discussed by Rignot and Mac Ayeal [1998] for the Lassiter Coast and the Hemmen ice Rise at the two geographical extremes of the Filchner-Ronne Ice Shelf front. Rifts mainly filled with marine ice bodies would show a coherent rheological behavior with the surrounding ice shelf, while this would lessen or not be the case for rifts filled with an “ice mélange”.

[20] **Acknowledgement.** Marie Dierckx is funded by the IceCubeDyn project (ARC) from the Communauté française de Belgique (Belgium). The compression device was supported by the Belgian Science Policies ASPI program (2006–2008), (SD/CA/02B). The authors would also like to thank the Programma Nazionale di Ricerche in Antartide for their logistics support in collecting the Nansen Ice Shelf cores. Finally, we thank C. Schroeder (ULB) for his availability and valuable advice.

References

- Budd, W. F., and T. H. Jacka (1989), A review of ice rheology for ice sheet modelling, *CRST*, 16(2), 107–144.
- Craven, M., I. Allison, H. A. Fricker, and R. Warner (2009), Properties of a marine ice layer under the Amery Ice Shelf, East Antarctica, *J. Glaciol.*, Vol. 55, 192, 717–728.
- Cuffey, K. M., and W. S. B. Paterson (2010), *The Physics of Glaciers*, fourth edition, Oxford, Butterworth-Heinemann, 693 p.
- Dierckx, M., T. Goossens, D. Samyn, and J. L. Tison (2010), Compression experiments on artificial, alpine and marine ice: Implications for ice-self/continental interactions, *Geophys. Res. Abstr.*, Vol. 12, 761.
- Eicken, H., H. Oerter, H. Miller, W. Graf, and J. Kipfstuhl (1994), Textural characteristics and impurity content of meteoric and marine ice in the Ronne Ice Shelf, Antarctica, *J. Glaciol.*, Vol. 40, 135, 386–398.
- Glen, J. W. (1958), The flow law of ice: A discussion of the assumptions made in glaciers theory, their experimental foundations and consequences, *IASH*, 171–183.
- Hooke, R. L. (1998), *Principles of Glacier Mechanics*, Upper Saddle River, N. J.: Prentice Hall, 248 p.
- Jacka, T. H. (1984), The time and strain required for development of minimum strain rates in ice, *CRST*, 8, 261–268.
- Jacka, T. H., and J. Li (1994), The steady-state crystal size of deforming ice, *J. Glaciol.*, 20, 13–18.
- Jacobs, S. S., H. H. Helmer, C. S. M. Doake, A. Jenkins, and R. M. Frolich (1992), Melting of ice shelves and the mass balance of Antarctica, *J. Glaciol.*, Vol. 38, 130, 375–387.
- Jansen, D., A. Luckman, B. Kulesa, E. C. King, and P. Holland (2012), Flow regime of the Joerg Peninsula suture zone, Larsen C Ice Shelf: The role of marine ice, *Geophys. Res. Abstr.*, Vol. 114, 11685.
- Jones, S. J., and J. W. Glen (1969), The effect of dissolved impurities on the mechanical properties of ice crystals, *Phil. Mag.*, Vol. 19, 157, 13–24.
- Khazendar, A. (2000), Marine ice formation in rifts of Antarctic ice shelves: A combined laboratory study and modeling approach, *PhD thesis, Science Faculty, Université Libre de Bruxelles, Bruxelles, Belgium*.
- Khazendar, A., J. L. Tison, B. Stenni, M. Dini, and A. Bondesan (2001), Significant marine-ice accumulation in the ablation zone beneath an Antarctic ice shelf, *J. Glaciol.*, vol. 47, 158, 359–368.
- Khazendar, A., and A. Jenkins (2003), A model of marine ice formation within Antarctic ice shelf rifts, *J. Geophys. Res.*, vol. 108(C7), 3235.
- Khazendar, A., E. Rignot, and E. Larour (2009), Roles of marine ice, rheology, and fracture in the flow and stability of the Brunt/Stancomb-Wills Ice Shelf, *J. Geophys. Res.*, vol. 114, F04007.
- Langway, C. C. J. (1958), Ice fabrics and the Universal stage, *CRREL Tech. Rep.* 62, pp. 16.
- Montagnat, M., and P. Duval (2004), The viscoplastic behaviour of ice in polar ice sheets: Experimental results and modelling, *C. R. Physique*, 5, 699–708.
- Moore, J. C., A. P. Reid, and J. Kipfstuhl (1994), Microstructure and electrical properties of marine ice and its relationship to meteoric ice and sea ice, *J. Geophys. Res.*, vol. 99(C3), 5171–5180.
- Morgan, V. I. (1972), Oxygen isotope evidence for bottom freezing on the Amery Ice Shelf, *Nature*, vol. 238, 5364, 393–394.
- Oerter, H., J. Kipfstuhl, J. Determann, H. Miller, D. Wagenbach, A. Minikin, and W. Graf (1992), Evidence for basal marine ice in the Filchner-Ronne Ice Shelf, *Nature*, vol. 358, 6385, 399–401.
- Oerter, H., H. Eicken, J. Kipfstuhl, H. Miller, and W. Graf (1994), Comparison between ice core B13 and B15. In Oerter, H., comp. Filchner-Ronne Ice Shelf Programme (FRISP). Report n°7. Bremerhaven, Alfred Wegener Institute for Polar and Marine Research, 29–36.
- Paterson, W. S. B. (1994), *The physics of glaciers*, third edition, Oxford, Butterworth-Heinemann, 481 p.
- Rignot, E., and D. R. Mac Ayeal (1998), Ice Shelf dynamics near the front of the Filchner-Ronne Ice Shelf, Antarctica, revealed by SAR interferometry, *J. Glaciol.*, Vol. 44, 147, 405–418.
- Russell-Head, D. S., and Wilson C. J. L. (2001), Automated fabric analyser system for quartz and ice, *Abstr. Geol. Soc. Aust.*, 64, 159.
- Samyn, D., J. P. Remy, P. Duval, M. Montagnat, and J. L. Tison (2007), Compression experiments on marine ice from Nansen Ice Shelf, Antarctica: Implications for ice-shelf/continent interactions, *Geophys. Res. Abstr.*, Vol. 9, 00803.
- Samyn, D., M. Dierckx, J. P. Remy, T. Goossens, and J. L. Tison (2011), A simple and updated pneumatic method for uniaxial ice compression in the laboratory: Experimental settings and creep test results on glacier ice, *J. Glaciol., Instrum. Meth.*, Vol. 57, 202, 337–344.
- Sarmiento, J. L., and N. Gruber (2006), *Ocean Biogeochemical Dynamics*, Princeton University Press, 503 p.
- Schulson, E. M., and P. Duval (2009), *Creep and Fracture of Ice*, Cambridge University Press, first edition, 401 p.
- Souchez, R., J.-L. Tison, R. Lorrain, C. Fléhoc, M. Stiévenard, J. Jouzel and V. Maggi (1995) Investigating processes of marine ice formation in a floating ice tongue by a high-resolution isotopic study. *J. Geophys. Res.*, vol. 100, C4, 7019–7025.
- Tison, J.-L., D. Ronveaux, and R. D. Lorrain (1993), Low salinity frazil ice generation at the base of a small Antarctic ice shelf, *Antarct. Sci.*, Vol. 5, 3, 309–322.
- Tison, J.-L., R. D. Lorrain, A. Bouzette, M. Dini, A. Bondesan, and M. Stievenard (1998), Linking landfast sea ice variability to marine ice accretion at Hells Gate Ice Shelf, Ross Sea. In Jeffries, M.O., ed. *Antarctic Sea Ice: Physical Processes, Interactions and Variability*. Washington, DC, American Geophysical Union, 375–407. (Antarctic Research Series 74.)
- Tison, J.L., and A. Khazendar (2001), A two phase approach to the simulation of the combined isotope/salinity signal of marine ice, *J. Geophys. Res.*, vol. 106, C12, 31387–31401.
- Treverrow, A., R. C. Warner, W. F. Budd, and M. Craven (2010), Meteoric and marine ice crystal orientation fabrics from the Amery Ice Shelf, East Antarctica, *J. Glaciol.*, Vol. 56, 199, 877–890.
- Trickett, Y. L., I. Baker, and P. M. S. Pradhan (2000), The effects of sulfuric acid on the mechanical properties of ice single crystals, *J. Glaciol.*, Vol. 46, 153, 239–243(5).
- Weertman, J. (1983), Creep deformation of ice, *Annu. Rev. Earth Planet. Sci.*, Vol. 11, 215 p.
- Wilson, C. J. L., D. S. Russell-Head, and H. M. Sim (2003), The application of an automated fabric analyser system to the textural evolution of folded ice layers in shear zones, *Ann. Glaciol.*, Vol. 37, 7–17.
- Zotikov, I. A. (1986), The thermophysics of glaciers, *Glaciol. Quaternary Geol.*, 275 p.

Optical-televviewer-based identification and characterization of material facies associated with an Antarctic ice-shelf rift

Bryn HUBBARD,¹ Jean-Louis TISON,² Frank PATTYN,² Marie DIERCKX,²
Thierry BOEREBOOM,² Denis SAMYN^{2,3}

¹*Centre for Glaciology, Institute of Geography and Earth Sciences, Aberystwyth University, Aberystwyth, UK*

E-mail: byh@aber.ac.uk

²*Département des Sciences de la Terre et de l'Environnement, Faculté des Sciences, Université Libre de Bruxelles, Bruxelles, Belgium*

³*Department of Mechanical Engineering, Nagaoka University of Technology, Nagaoka, Japan*

ABSTRACT. We have drilled 13 boreholes within and around a through-cutting rift on the (unofficially named) Roi Baudouin Ice Shelf, East Antarctica. Logging by optical televviewer (OPTV) combined with core inspection has resulted in the identification and characterization of several material facies. Outside the rift, OPTV-imaged annual layering indicates ~150 years of accumulation over the 66 m length of one of the boreholes. Luminosity analysis of this image also reveals the presence of numerous dark melt layers as well as a systematic decrease in background luminosity, interpreted in terms of a progressive increase in light transmission during firnification. We identify four material facies within the rift: snow, granular ice, marine ice and unconsolidated platelets. We interpret the granular ice facies as snow that has been saturated by percolating sea water, and the underlying marine ice as compacted buoyant platelets that have adhered to the rift base. Core sections reveal the presence of tubular channels within the marine ice, indicating that it is macroporous and permeable to sea water. The lower boundary of this facies merges into a mushy layer of unconsolidated platelets that were successfully imaged by OPTV, revealing irregular sub-horizontal layering similar to that reported previously on the basis of (directional) borehole video.

INTRODUCTION

An increasing body of evidence indicates that ice shelves are not composed exclusively of relatively uniform meteoric snow, firn and ice. Instead, they appear to be characterized by an intricate network of inherited structural weaknesses (e.g. Shabtaie and Bentley, 1982; Glasser and Scambos, 2008) and to be composed of several different material types or facies, including marine ice formed by the aggregation and compaction of buoyant platelets formed within the sub-ice-shelf water cavity (e.g. Morgan, 1972; Engelhardt and Determann, 1987; Oerter and others, 1992; Tison and others, 1993; Eicken and others, 1994; Fricker and others, 2001; Holland and others, 2009). Indeed, this spatial variability in material composition (and therefore response to imposed stresses) may be central to dictating rates and patterns of both normal ice-shelf flow and ice-shelf disintegration during break-up. For example, the break-up pattern of the Larsen B ice shelf, Antarctic Peninsula, could only be modelled successfully upon introducing widespread spatial variations in ice softness, in this case assumed to involve marine or suture ice (Khazendar and others, 2007). Steady-state modelling of the Larsen C ice shelf also shows an improved match between modelled and measured surface velocity vectors once spatial variations in ice softness, principally linear filaments of suture ice, are incorporated into the model (personal communication from D. Jansen, 2011). It is therefore clearly important to our understanding of current and future ice-shelf behaviour that we have a good knowledge of the spatial composition of ice shelves and in particular of zones of basal melting and of marine ice accretion.

One major recent development in terms of identifying and quantifying sub-ice-shelf processes and materials

involves exploration by autonomous vehicles (Jenkins and others, 2010). However, such expeditions are still in their infancy and are logistically demanding, restricting spatial coverage. Further, despite accessing the underside of ice shelves, they do not yet sample ice directly. Options for accessing and sampling from the interior of ice shelves directly therefore rely primarily on borehole drilling from the surface. For example, the Amery Ice Shelf Ocean Research (AMISOR) project (Craven and others, 2004, 2005, 2009; Roberts and others, 2007; Treverrow and others, 2010) drilled to the base of the Amery Ice Shelf, East Antarctica, at two locations along a flowband underlain by marine ice. These borehole logs reveal that continental ice is underlain by a $\leq \sim 200$ m thick layer of marine ice formed by the adhesion of buoyant platelets onto the ice-shelf base. This marine ice layer is also known, from the analysis of core segments and borehole video (Craven and others, 2005), to become progressively more permeable and less consolidated towards its base. Specifically, the video analysis revealed several material properties of both the continental ice and the underlying marine ice, including the presence of frequent (relatively dark) melt layers and lenses within the bubbly (and therefore brighter) continental ice, and the presence of platelet-like crystals both forming the underlying marine ice and suspended within the borehole fluid. Video footage also revealed that the marine ice hosted brine cells and had a layered structure, both of which increased in intensity towards the ice-shelf base until eventually, within some tens of metres of the shelf–water interface, the texture of the ice became flaky and the brine cells opened up to form voids, resulting in highly permeable ‘honeycomb’ ice (Craven and others, 2005).

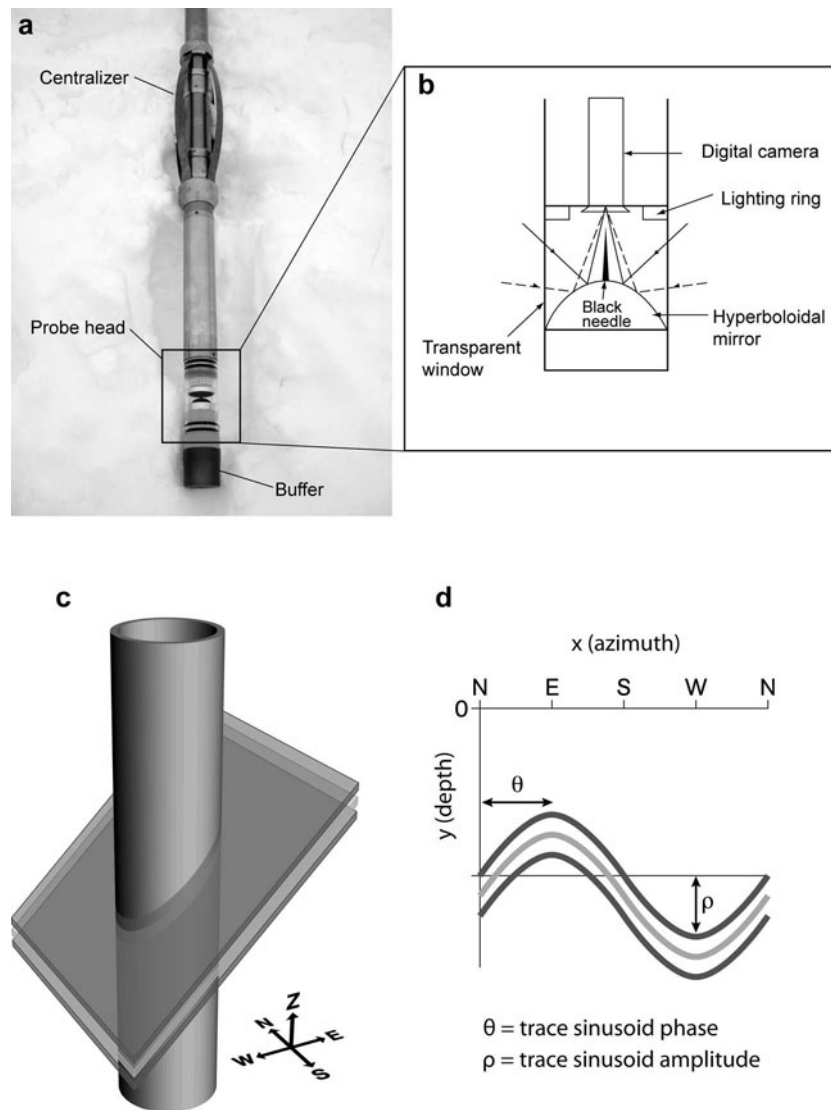


Fig. 1. Illustration of the principles of OPTV operation. (a) Image of OPTV probe and (b) expanded sketch of probe head, (c) schematic illustration of a borehole intersecting three closely spaced layers dipping west and (d) illustration of their equivalent sinusoids on the raw OPTV image.

Drilling through ice shelves is logistically demanding and slow, particularly since most such shelves are several hundred metres thick even at their seaward edge. One means of reducing this demand may be to drill boreholes through the relatively thin base of ice-shelf rifts. Such rifts are common, particularly in zones of high lateral shear near the margins of ice-shelf flow units (Glasser and others, 2009), and the infilling melange may only be some metres to tens of metres thick (e.g. Fricker and others, 2005). Although this melange is largely composed of wind-blown snow, frozen sea water and fragments of ice talus, distinguishing it from the internal composition of the ice shelf proper, Khazendar and others (2001) and Khazendar and Jenkins (2003) demonstrated that rifts are also highly likely to be sites for the rapid formation of marine ice from below. Thus, drilling through the base of a through-cutting rift may well also provide ready access to newly formed and actively forming marine ice, as well as to other melange materials.

Once boreholes have been drilled through an ice shelf, logging by digital optical televiewer (OPTV) has the potential to provide important information in terms of identifying and characterizing the ice types intersected. OPTV differs in one

fundamental respect from traditional (directional) borehole video in that OPTV acquires a geometrically accurate image of the complete borehole wall. This is achieved by the probe's downward-looking digital camera recording a 360° annular image of the borehole wall as reflected in a hyperboloidal mirror (Fig. 1a and b). Accurate winch control then allows the probe to be raised and lowered at a precise rate along the borehole, typically producing images with a vertical resolution that can be user-set to a pixel dimension as small as 1 mm and at a lateral resolution of either 360 or 720 pixels per row (~1.0 mm and ~0.5 mm per pixel, respectively, for a borehole of 12 cm diameter). This geometrical accuracy provides a powerful means of mapping the structures that intersect a borehole wall because each visible intersecting plane appears as a sinusoidal trace on the raw OPTV image. Here, the dip and dip-direction of each such plane (orientated by magnetometers located within the OPTV probe) are represented respectively by the amplitude and phase of the associated sinusoid (Fig. 1c and d). Structural analysis of an OPTV log thereby allows all such features to be located, characterized in terms of their thickness and appearance, and their orientations to be logged.

OPTV was recently applied for the first time to ice boreholes by Hubbard and others (2008). Subsequently, Roberson and Hubbard (2010) applied the technique to an array of boreholes drilled by hot water at Midre Lovénbreen, Svalbard, in an attempt to determine the structural composition of this polythermal valley glacier. Here, OPTV logs successfully revealed bubble-rich layers and bubble clouds, debris bands (including individual clasts) and several generations of stratification and folding. In this case, where boreholes were drilled by hot water and no core was therefore retrieved, the OPTV analysis was particularly valuable in that it allowed 'virtual' core images to be recreated by rolling the raw (outward-looking) images acquired of the borehole walls and viewing them inwards. OPTV analysis can also potentially provide important complementary information from boreholes from which actual ice core has been recovered. First, OPTV views laterally into the ice surrounding the borehole, thereby providing a deep-field image with the capacity to reveal properties not easily identifiable from (or intersected by) a core that is typically 8–12 cm in diameter. Second, OPTV images cover the entire length (and circumference) of a borehole wall, whereas core may not be retrieved from the borehole's full length, for example being absent from englacial channels or voids. Core sections can also be fractured beyond reconstruction. Third, OPTV imaging can view unconsolidated materials that may not be recoverable as a solid core. This facility may be particularly valuable, for example in boreholes that intersect unconsolidated honeycomb ice or sub-ice-shelf platelets. Despite this potential, however, OPTV has not yet been applied to ice-shelf boreholes.

In this paper, we report on the character and genetic interpretation of material facies as revealed by OPTV logs and preliminary core inspection from a series of boreholes drilled in and around a through-cutting rift located near the seaward edge of the Roi Baudouin Ice Shelf (RBIS), Antarctica. The aims of the study are twofold: (1) to evaluate the suitability of OPTV logs for the investigation of ice-shelf facies; and (2) to report on the spatial prevalence of, and to provide preliminary interpretations for, the facies intersected by our boreholes on the RBIS.

FIELD SITE AND METHODS

Field site

The (unofficially named) RBIS is located on the Princess Ragnhild Coast, East Antarctica, at $\sim 70^\circ\text{S}$, 24°E (Fig. 2a). The ice shelf extends southwest–northeast for ~ 350 km along the coast and has a flow-parallel width of ~ 50 – 100 km. The rift investigated herein is located within ~ 5 km of the seaward edge of the ice shelf and both are aligned approximately parallel to each other (Fig. 2b). The rift forms the easternmost limb of a suite of fractures related to the presence of an ice rise located ~ 10 km upflow. Measured ice velocity in the region of the rift is ~ 350 – 380 m a^{-1} (Pattyn and others, 2005), markedly lower than that predicted theoretically in the absence of the ice rise. The ice shelf overlies a relatively shallow ocean cavity with a sub-ice-shelf water column thickness of ~ 200 – 300 m (Pattyn and others, unpublished information). We drilled 13 boreholes, each 5–66 m long, in either the rift or the adjacent ice shelf. Of these, six penetrated the base of the rift, extending

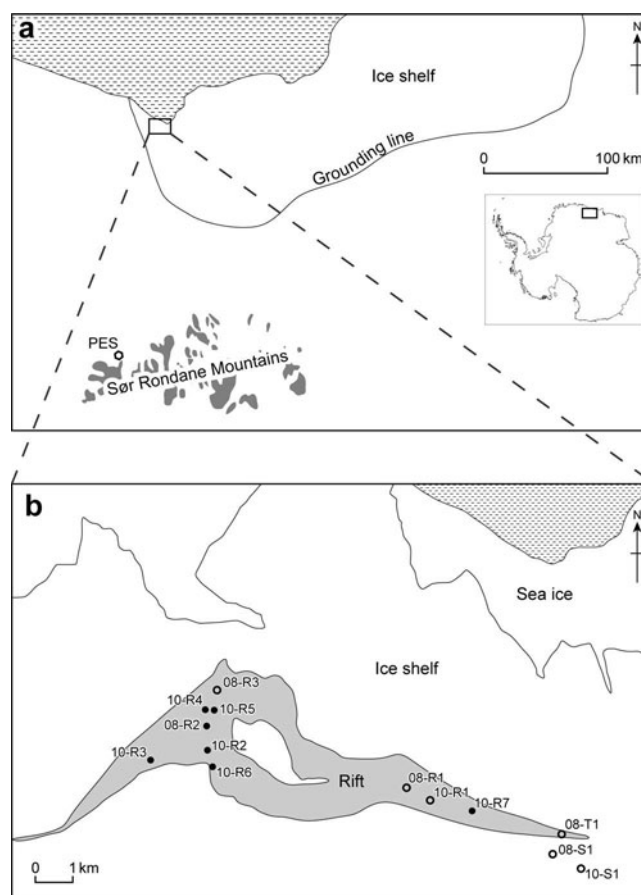


Fig. 2. Location map of (a) the general study site on the Roi Baudouin Ice Shelf (PES is Princess Elisabeth Station) and (b) the individual boreholes reported herein. Boreholes logged by OPTV are represented as open circles.

into the underlying cavity, and six were logged by OPTV (Fig. 2b; Table 1).

Methods

Boreholes were drilled (during December 2008 or December 2010) either by a mechanical SIPRE-type corer or by an adapted Eclipse ice drill. The latter was modified to enable coring through permeable ice saturated with sea water, requiring contacts within the drill assembly (including those within the slip ring) to be electrically isolated. Importantly, these adaptations allow the Eclipse drill to operate in boreholes filled with sea water, permitting coring below the local water level to the base of the ice shelf. Once drilled, OPTV analysis was carried out as soon as possible and usually within some tens of minutes in order to avoid borehole closure by freezing and, where boreholes penetrated the cavity, clogging by buoyant platelets rising up the sea-water column in the boreholes. The latter effect was unfortunately common, generally occurring within some minutes of the corer being removed from the hole and effectively preventing OPTV logging of several rift boreholes. Once logged, OPTV images were collated, analysed and prepared for presentation (including rolling to create virtual core images) using WellCAD software. This analysis included calculating the luminosity (expressed in non-dimensional units of RGB pixel brightness) of each 1 mm depth step, represented by the mean value of each ring of 720 pixels. Within some metres (depending on the optical

Table 1. Summary data for boreholes cored on the RBIS in 2008 and 2010

Borehole	Location	Northing*	Easting*	Length m	OPTV	Note
08-S1	Shelf	70 21 40.7	24 27 11.3	15.24	Yes	Terminated englacially in water-saturated firn
08-T1	Rift tip	70 21 25.0	24 27 33.0	38.28	Yes	Terminated englacially in firn
08-R1	Rift	70 21 14.5	24 25 37.6	9.65	Yes	Terminated englacially in water-saturated ice
08-R2	Rift	70 20 12.5	24 13 09.2	18.40	No	Penetrated rift base into platelet ice/cavity
08-R3	Rift	70 19 28.6	24 13 22.4	13.26	Yes	Penetrated rift base into platelet ice/cavity
10-S1	Shelf	70 21 38.9	24 27 14.9	66.40	Yes	Terminated englacially in ice-shelf ice
10-R1	Rift	70 20 44.4	24 21 07.8	13.56	Yes	Penetrated rift base into platelet ice/cavity
10-R2	Rift	70 20 05.6	24 12 06.2	7.29	No	Penetrated rift base into platelet ice/cavity
10-R3	Rift	70 20 13.8	24 09 48.1	29.71	No	Penetrated rift base into platelet ice/cavity
10-R4	Rift	70 19 32.3	24 12 00.0	19.19	No	Terminated englacially in water-saturated rift ice
10-R5	Rift	70 19 32.3	24 12 21.3	21.44	No	Terminated englacially in water-saturated rift ice
10-R6	Rift	70 20 20.1	24 12 11.9	4.86	No	Penetrated rift base into platelet ice/cavity
10-R7	Rift	70 20 53.2	24 22 49.4	11.02	No	Terminated englacially in water-saturated rift ice

*These locations were recorded at the time of coring. They have since been advected with the motion of the ice shelf, which in this area is moving in an approximately northerly direction by $\sim 350\text{--}380\text{ m a}^{-1}$ (Pattyn and others, 2005).

transmissivity of the material being cored) of the borehole surface, recorded light is dominated by that transmitted from the surface, but below this zone it is exclusively composed of that reflected back from the borehole walls to the OPTV sensor. Since borehole illumination, achieved by a circular array of white LEDs, is uniform in time and therefore also in space as the probe moves along a borehole, the net luminosity of the recorded signal varies with the reflectivity of the material forming the borehole wall.

RESULTS

Ice-shelf boreholes

The OPTV logs of the two boreholes cored into the ice shelf proper, 08-S1 and 10-S1 (Fig. 2b; Table 1), reveal similar material properties, with 66 m long 10-S1 providing the longer record. The log of 10-S1 (Figs 3 and 4), has three notable features. First, regularly repeated dark layers, which have a typical luminosity of ≤ 100 units lower than the local image background, can be observed along most of the length of the core. The spacing of these layers gradually decreases from ~ 1.0 m near the borehole's upper surface (e.g. five regularly spaced darker layers between 4 and 9 m depth in Fig. 3) to ~ 0.15 m near its base (e.g. seven regularly spaced darker layers between 51.5 and 52.5 m depth in Figs 3 and 4b). Although still visible, these layers are more difficult to distinguish from the (now darker) background towards the base of the borehole. Second, sharply defined very dark layers, typically with a luminosity that is >100 units lower than the local image background, are observed intermittently along the full length of the borehole. For example, four distinctive dark bands are located between 30 and 31 m depth, each of which is 5–20 cm thick (Figs 3 and 4a). Thus, the luminosity of these layers is typically similar to, or darker than, that of the thinner and more regular layers noted above. Finally, if both the above sets of dark layers are removed from the analysis, the background reflected light intensity of the OPTV log of 10-S1 decreases consistently down the borehole, from typical values of ~ 400 near the ice-shelf surface to ~ 150 at the base of the borehole, visible in both Figures 3 and 4.

Rift boreholes

We drilled ten boreholes into the base of the rift proper and one was drilled into the ramp formed in the rift tip (Fig. 2b; Table 1). Several of these boreholes intersected apparently fundamentally different material facies. The OPTV log of 08-T1, cored for 38 m into the rift tip, was of uniformly high luminosity, similar to the material forming the matrix between the dark layers in 10-S1 (above). Indeed, the OPTV log of 08-T1 contrasts with that of 10-S1 in that the former is characterized by (1) fewer dark layers and (2) no apparent systematic decrease in the intensity of the background reflected light with depth.

All of the remaining ten boreholes were drilled directly into the base of the rift (Fig. 2b), intersecting a series of material facies which always appeared in the same order but which were not all present at every borehole. These facies are as described below.

Surface snow

Snow was present in the uppermost sections of most rift boreholes and was identified visually at the surface and as a very bright backscatter in OPTV logs. Where present, this layer extended only for a few metres below the surface.

Granular ice

This facies, defined by a distinctively granular structure, was relatively massive and appeared highly uniform on OPTV logs. However, it did occasionally contain isolated bubble clusters, particularly at depth. It was present in most rift boreholes, but generally decreased in representation westwards, away from the rift tip. The upper surface of the granular ice also commonly coincided with the level of the saline-water table (sea level) within the rift and the two were always observed to be in close proximity. This facies typically extended for some metres below sea level.

Marine ice

Progressing down-borehole, granular ice gradually gave way to a less massive and more strongly layered ice facies that was very similar in character to the marine ice imaged on the Amery Ice Shelf (Craven and others, 2005, 2009). This facies was present in all rift boreholes, either on its own or

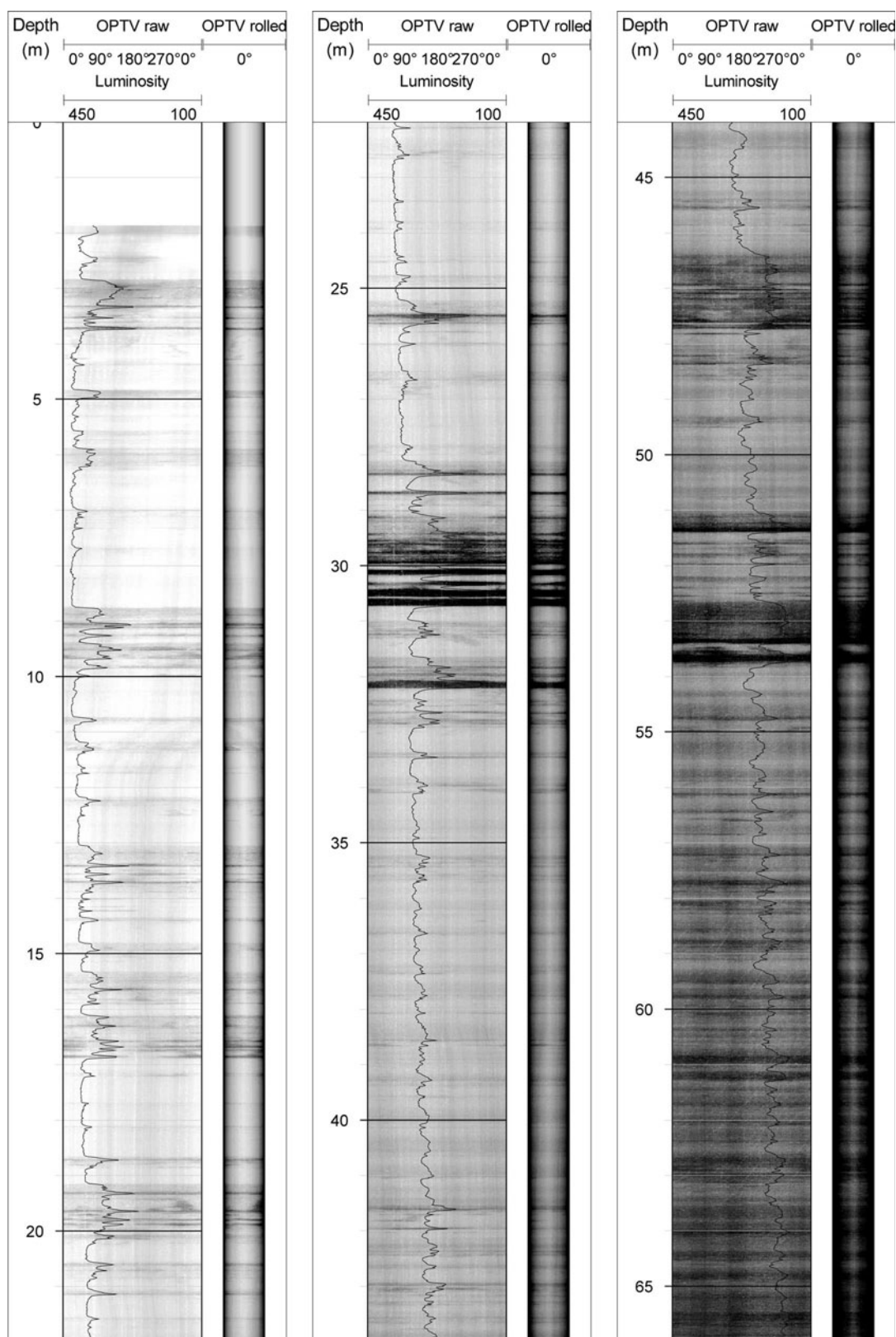


Fig. 3. OPTV log of the full length of ice-shelf core 10-S1. The raw OPTV image is plotted on the left-hand side of each panel and its rolled equivalent is plotted on the right. The luminosity trace overlaid on the raw OPTV image is sampled each millimetre in the vertical and is scaled to decrease, over the range 450–100 (non-dimensional) units, to the right.

beneath the granular facies (and never above it), and showed an increased prevalence further west, away from the rift tip, as the thickness of the granular ice diminished. Indeed, in some of the most westerly boreholes (e.g. 08-R3), the marine ice facies extended the full thickness of the rift, cropping out

at its upper surface (Fig. 5). Although this facies appeared to be homogeneous in OPTV images, containing no notable bubble-defined layering, it was characterized by a green hue, particularly under transmitted light near the surface. We interpreted this as due to the presence of a low

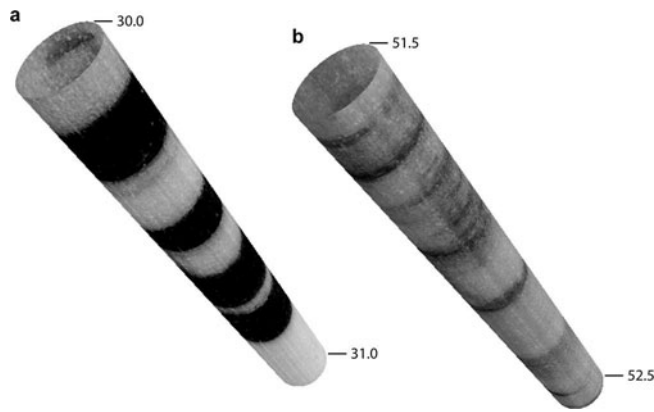


Fig. 4. Expanded rolled OPTV images of two 1 m long virtual core segments from ice-shelf core 10-S1 (Fig. 3): (a) 30–31 m depth and (b) 51.5–52.5 m depth.

concentration of chlorophyll-bearing marine algae, supported by occasional observations of dense patches of algae in core sections recovered from this facies. Such algae were not observed within the overlying granular ice. Although not clearly imaged by OPTV, core sections of marine ice did reveal the development of a strong sub-horizontal crystal alignment with depth, giving the facies a fissile texture.

One further notable aspect of this facies is that it contained sinuous tubular channels, similar in appearance to large worm-holes (Fig. 6). These tubes were intersected by our cores on several occasions (e.g. 10-R3) and are typically 1–3 cm in diameter and appear to have no preferential orientation. Unfortunately, no OPTV log was recovered from a borehole segment intersecting such a tube, principally because most of the rift holes became blocked with buoyant ice platelets before OPTV logging was possible. However, the tubes were observed directly in the recovered core sections (Fig. 6).

Ice platelets

Towards the base of the rift cores, the marine ice became so fragile that it formed only a weakly consolidated mass of thin platy crystals (Fig. 7). Below this point, the crystals were effectively unconsolidated and samples could no longer be retrieved by traditional coring (since the retaining core dogs could no longer hold the unconsolidated slurry within the barrel), effectively forming a sea-water-saturated ‘mushy layer’ (Feltham and others, 2006). This transition marked the indistinct interface between the base of the solid ice shelf and the platelet-rich uppermost layers of the underlying sea water. One OPTV log, recovered from 08-R3 (Figs 5 and 8), did extend for ~4 m below the point at which solid core was no longer retrievable, thereby presumably penetrating the uppermost layers of the platelet-rich cavity. This lowermost section of the OPTV log of 08-R3 revealed the presence of unconsolidated material that was characterized by small-scale sub-horizontal wavy layering (Fig. 8), strikingly similar in appearance to that imaged by directional video at the base of the Amery Ice Shelf (fig. 13 in Craven and others, 2005). These layers were repeated every few centimetres throughout the facies. Unfortunately, OPTV images could not be obtained from deeper into this facies because the buoyancy of the unconsolidated mass prevented further OPTV probe penetration.

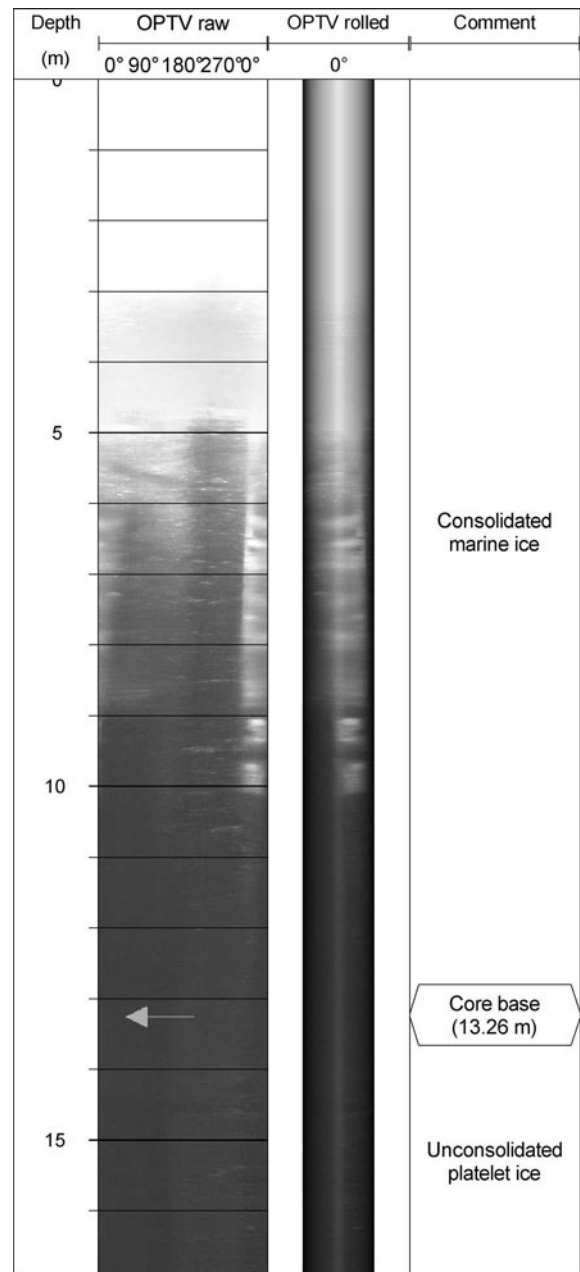


Fig. 5. OPTV log of the full length of rift core 08-R3 with (progressing left to right) the raw OPTV image, the rolled OPTV image and annotations. Note that no solid core was retrieved from below 13.26 m depth where unconsolidated platelet ice was encountered. Although not visible in the OPTV log, the ‘core base’ at 13.26 m marks the point at which no more core could be recovered by mechanical coring. An annotated expansion (represented in three dimensions as a virtual core) of the unconsolidated platelet ice forming the lowermost part of this log is presented in Figure 8.

INTERPRETATION

Ice-shelf boreholes

The ice-shelf cores (08-S1 and 10-S1) both began in surface snow. However, while the former terminated in firn, the latter (being >66 m long) penetrated through the firn and into the underlying ice. Three specific characteristics of the OPTV images retrieved from 10-S1 were reported: (1) regular layering by dark bands, (2) intermittent layering by thicker dark bands and (3) a general down-core decrease in

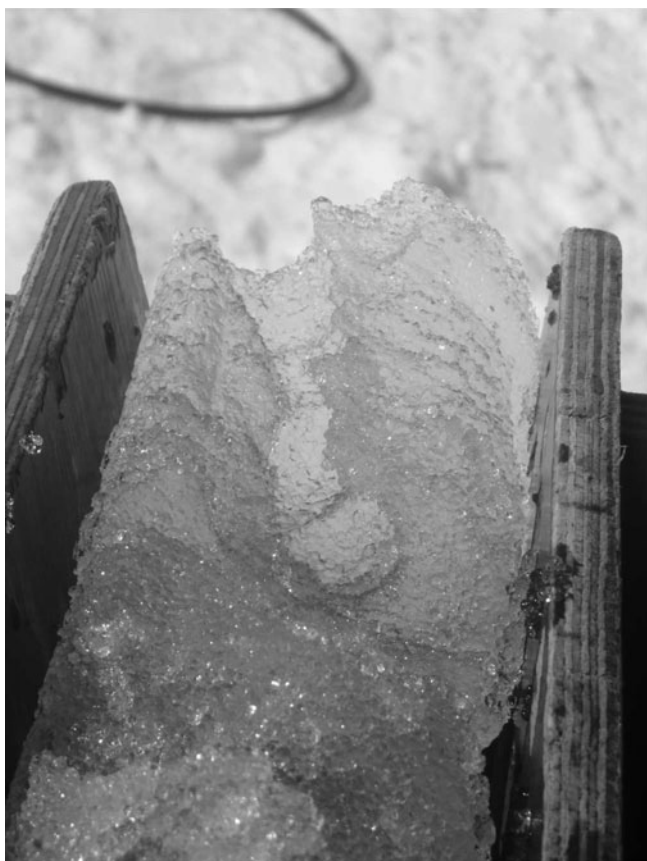


Fig. 6. Photographic image of a typical worm-hole-like tubular conduit located within core 10-R3. The core is retained within a wooden core holder and the tube extends approximately vertically along the top of the core. The tube is ~25 mm in diameter.

luminosity. We interpret the first of these, the ‘primary’ layering, as annual layers similar to those previously identified on the basis of directional video by for example Hawley and others (2003) and Hawley and Morris (2006). In such logs, the darker zones mark the more melt-influenced icy layers formed during the summer, and the lighter zones the colder winter accumulation. The summer layer spacing of ~1.0 m near the surface of 10-S1 accords with regional mass-balance approximations which indicate an accumulation of ~0.3 m w.e. a⁻¹ (Van de Berg and others, 2006). However, this primary layering was frequently disrupted by the second layer type, which was darker (indicating less reflected light, consistent with bubble-poor ice) and had sharper boundaries with the matrix material. These characteristics, along with the intermittent occurrence of this ‘secondary’ layering along the borehole, are consistent with an interpretation as refrozen surface melt layers. Although comparison with the spacing of annual layers (below) suggests that these melt events do not occur each summer, they do appear throughout the full borehole length. The presence of these secondary melt layers also makes it difficult to derive an age–depth relationship for 10-S1 by primary-layer counting. However, the age range of this borehole may be approximated by interpolating primary-layer spacing from zones that are devoid of melt layers (e.g. 5–9, 17–19, 22–25, 36–40, 50–51 and 56–60 m in Fig. 3), suggesting that the record extends back for ~150 years from present. Although the frequent melt layers disrupt the core’s potential to provide an undisturbed palaeoenvironmental

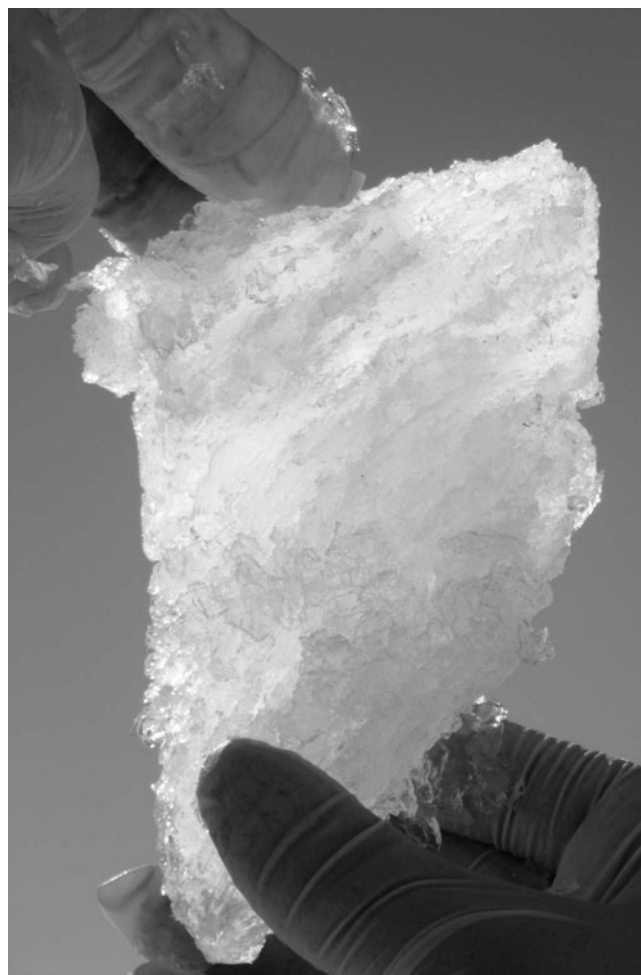


Fig. 7. Photographic image of a sample of highly flaky marine ice just above the point at which it becomes completely unconsolidated and can no longer be retrieved by coring.

record, they do provide independent information on the scale and timing of major surface melting events and directly affect only a minor proportion of the core’s total length. Palaeoenvironmental reconstructions should therefore still

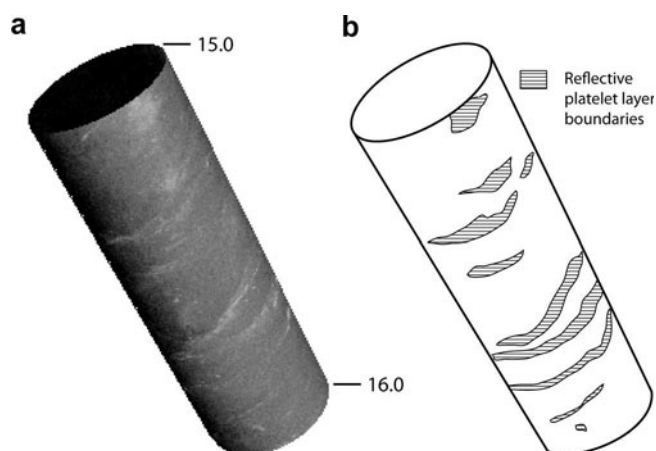


Fig. 8. Rolled OPTV virtual core image of a 1 m interval (15–16 m) near the base of core 08-R3 (Fig. 5): (a) actual OPTV image, (b) interpretative sketch. Brighter light reflected off repeated irregular sub-horizontal layering is interpreted as marking the boundary of layers of aggregated sub-ice-shelf platelets.

be possible from cores such as this, as long as the physical influence of melting events is isolated and removed from the analysis. Finally, we interpret the general down-hole decrease in the luminosity of the OPTV image of 10-S1 (at a rate of 3.5 units m^{-1} depth, averaged linearly over the full 66 m borehole length; Fig. 3) in terms of progressive firnification, specifically the gradual isolation and coalescence of bubbles resulting in a net increase in the optical transmissivity (and concomitant decrease in reflectivity) of the borehole wall.

Rift boreholes

The material imaged in the rift tip (08-T1) was similar to that forming the matrix of 10-S1. However, in contrast to the OPTV log of 10-S1, that of 08-T1 is uniform and includes only three slightly darker layers that are each only a few centimetres thick. Further, luminosity does not decrease measurably with depth along 08-T1. We interpret these properties, in association with the location of the borehole in the rift tip, as indicative of infilling by blown snow (as opposed to surface firnification on the ice shelf; see above). This process, described by Leonard and others (2008) for a rift on the Ross Ice Shelf, would result in little or no seasonal signal, while the possible rapidity of aeolian infilling may also explain the absence of firnification-related bubble nucleation with depth.

Within the rift proper, we interpret the uppermost granular ice facies as snow and firn that have become saturated by percolating saline water, causing the observed grain rounding. This interpretation is also consistent with the general thinning of this facies westwards, away from the apex of the rift, where the rate of surface accumulation by snow trapping is expected to be lower. Progressing westwards and with depth into the base of the rift, this facies gives way to the marine ice facies. All of the properties of this facies, and in particular its occasional high algal content and gradual disintegration into unconsolidated platelets at the base of the rift boreholes, suggest formation by the progressive accumulation and compaction of buoyant platelets formed within the sub-ice-shelf cavity, consistent with previous interpretations. The fact that these platelets rose up the water column rapidly in completed boreholes, commonly preventing OPTV access within some minutes of drilling penetrating the cavity (08-R3 being the sole exception in this study), indicates that the platelets were both buoyant and mobile. The ubiquitous presence of this facies within our rift boreholes, typically to a thickness of some metres to tens of metres, also indicates that platelet marine ice formed throughout the rift.

Finally, the unique observations of worm-hole-like tubes within the granular ice and marine ice facies provide clear evidence of conduit-based water flow through the lowermost layers of the rift melange. We assume that these conduits are formed during the early stages of ice formation when the material is still erodible and then become frozen-in as the material consolidates and (possibly) de-waters. It is therefore apparent that this marine ice is highly porous and permeable, consistent with previous indications (e.g. Craven and others, 2005). One characteristic of marine ice that remains poorly understood is its very low measured bulk salinity (typically 0.05–0.5‰; e.g. Tison and others, 2001) relative to that measured in sea ice (typically 1–20‰; Weeks, 2010), despite both ice types being formed by the aggregation and consolidation of frazil ice frozen from sea

water. Eicken and others (1994) argued that the standard mechanisms of post-formational desalination proposed for sea ice are in fact insufficiently effective to reduce the salinity of marine ice to measured values. Instead, these authors tentatively invoked a mechanism of salt-water expulsion from already low-salinity platelets during buoyancy-driven aggregation and densification. Tabraham (1998) introduced the 'mushy layer' concept into a solidification model for marine ice. In this approach, relatively recently proposed to describe the desalination process in sea ice, convective movements in the interstitial liquid are driven by density instabilities due to salinity gradients in a temperature field increasing downwards. This leads to the development of convective 'chimneys' known as 'brine channels' in sea ice, exporting salts from the mushy layer to the ocean below. However, Tabraham (1998) also recognized that, although the model of drainage through channels produced some desalination in marine ice, the amount of desalination was found to be less than the levels observed within actual marine ice, the main problem being shutdown of the flow with continuing solidification. The author suggested that combining mushy-layer desalination with compaction might be sufficiently efficient to reach the observed low salinity values. Alternatively, Tison and others (2001) showed that by treating marine ice as a two-phase compound (pure frazil ice crystals in a consolidating interstitial fluid) and applying a boundary-layer model for consolidation of the interstitial liquid, marine ice salinities could be reproduced if fractionation coefficients derived from the solidification of fresh-water ice were used rather than those for columnar (dendritic skeletal layer) sea-water ice.

The 0.05–0.5‰ salinity range discussed above has generally been observed in thick (10^2 – 10^3 m) marine ice layers, and to the best of our knowledge no internal desalination chimneys (either active or relict) have been described in such layers. The marine ice salinity range in our RBIS dataset covers a range more typical of sea ice (≤ 9 ‰ in the lower layers), with very low salinities (0.1‰) only being measured in the upper few metres over a total thickness of a maximum of 10–20 m (Pattyn and others, unpublished information). The occurrence of the worm-hole-like tubes in the less consolidated lower layers could therefore represent the signature of mushy-layer-like convection processes in the early stages of consolidation of the marine ice layer. The fact that these tubes lack the typical vertical tree-like structure of sea-ice brine channels might reflect the geometrical control of the sub-horizontal accumulation pattern of the loose large frazil ice platelets. An alternative, or supplementary, hypothesis is that once the marine ice layer is formed, salt would continue to be expelled from the layer by freezing-front rejection accompanying ongoing recrystallization within the layer. The removal of that salt-rich water through an effective internal drainage system would then decrease the bulk salinity of the remaining marine ice. Such a process would also involve the delivery of relatively high-salinity water to the underlying water column.

SUMMARY AND DISCUSSION

OPTV logging of 13 boreholes, supplemented by visual analysis of their associated cores, from within and around a rift on the seaward edge of the RBIS has revealed the presence and stratigraphy of several distinctive material

facies. OPTV has the capacity to image these material types along with their internal variability, such as that associated with annual layering in snow, firn and ice. The technique may also have the capacity to provide a rapid borehole-based approximation of firn/ice reflectivity and therefore, indirectly, density. Importantly, the technique also has the capacity to image the immediate sub-ice-shelf cavity which may otherwise be extremely difficult to investigate.

Beyond technique evaluation, this study has resulted in the following glaciological findings and associated implications:

1. That annual layering is present at least in the uppermost layers of the ice shelf (at least for 66 m) and that this depth covers a time range of ~150 years. As anticipated, layer spacing decreases with depth.
2. That surface accumulation has been, for the full length of the record, interrupted by frequent episodes of summer melting. These events have commonly resulted in the formation of ice layers that are several centimetres thick and introduce additional complications in terms of obtaining continuous undisturbed palaeoclimatic records from such cores. Nonetheless, such cores may well be used to provide detailed palaeoclimatic information as long as the firn and ice influenced by the melt layers is excluded from the analysis. OPTV logging can assist in this.
3. That the OPTV logs of ice-shelf snow and firn darken with depth as bubble nucleation causes the reflectance of these materials to decrease. It is therefore possible that borehole-based OPTV luminosity could provide a proxy for the near-surface density of continental snow and ice.
4. That the material filling in the rift tip is blown snow that has been deposited rapidly and which shows very little variation in internal structure.
5. That the melange forming the floor of the rift is composed of distinctive material facies in the following stratigraphic arrangement: surface snow overlies granular ice overlies marine ice overlies unconsolidated platelets. The first two of these facies become less prevalent moving away from the rift tip, such that only marine ice and unconsolidated platelets were present in the westernmost boreholes. We hypothesize that the granular ice forms by the saturation of snow/firn by percolating sea water, while the underlying marine ice forms by the accumulation of buoyant platelets at the base of the solid ice shelf, consistent with previous investigations.
6. That marine ice contains organic matter, presumably of marine origin, giving it a distinctive green hue in OPTV images. Towards its base, marine ice also becomes mushy and is increasingly penetrated by tubular conduits, making the layer highly permeable.
7. That platelet ice is present ubiquitously in thicknesses of at least several metres beneath the rift. These platelets consolidate at the rift base as irregular sub-horizontal layers, but individual crystals appear to be both mobile and buoyant.

These findings and implications are based on OPTV and visual analysis alone and are therefore tentative. Future efforts will focus on direct core sampling in order to evaluate these interpretations by rigorous multi-parameter analysis. Nonetheless it is clear from this research that OPTV-based

borehole analysis has a significant contribution to make to the investigation of ice-shelf properties. In particular, the reconstruction of internal layering, which may not always be readily achievable from core analysis, has potential implications for topics such as the interpretation of internal reflecting horizons revealed by ice radar and as a check on core-derived palaeoclimatic reconstructions. Finally, the technique may represent the principal analytical tool in borehole sections from which core segments are missing or broken and in boreholes drilled by steam or hot water from which no ice core may be recovered.

ACKNOWLEDGEMENTS

This paper forms a contribution to the Belgian Research Programme on the Antarctic (Belgian Federal Science Policy Office), project No. EA/11/3A 'Belgian Ice Sheet Shelf Ice Measurements in Antarctica (BELISSIMA)' and to UK Royal Society grant RG1430. B.H. was also supported by the Climate Change Consortium of Wales (C3W). We thank the International Polar Foundation for Antarctic for support, and A. Hubert, R. Wagemans and K. Soete for invaluable assistance in the field. We also thank two anonymous reviewers and the scientific editor, Helen Fricker, for comments that led to the improvement of the manuscript.

REFERENCES

- Craven M and 6 others (2004) Initial borehole results from the Amery Ice Shelf hot-water drilling project. *Ann. Glaciol.*, **39**, 531–539 (doi: 10.3189/172756404781814311)
- Craven M and 7 others (2005) Borehole imagery of meteoric and marine ice layers in the Amery Ice Shelf, East Antarctica. *J. Glaciol.*, **51**(172), 75–84 (doi: 10.3189/172756505781829511)
- Craven M, Allison I, Fricker HA and Warner R (2009) Properties of a marine ice layer under the Amery Ice Shelf, East Antarctica. *J. Glaciol.*, **55**(192), 717–728 (doi: 10.3189/002214309789470941)
- Eicken H, Oerter H, Miller H, Graf W and Kipfstuhl J (1994) Textural characteristics and impurity content of meteoric and marine ice in the Ronne Ice Shelf, Antarctica. *J. Glaciol.*, **40**(135), 386–398
- Engelhardt H and Determann J (1987) Borehole evidence for a thick layer of basal ice in the central Ronne Ice Shelf. *Nature*, **327**(6120), 318–319
- Feltham DL, Untersteiner N, Wettlaufer JS and Worster MG (2006) Sea ice is a mushy layer. *Geophys. Res. Lett.*, **33**(14), L14501 (doi: 10.1029/2006GL026290)
- Fricker HA, Popov S, Allison I and Young N (2001) Distribution of marine ice under the Amery Ice Shelf, East Antarctica. *Geophys. Res. Lett.*, **28**(11), 2241–2244 (doi: 10.1029/2000GL012461)
- Fricker HA, Bassis JN, Minster B and MacAyeal DR (2005) ICESat's new perspective on ice shelf rifts: the vertical dimension. *Geophys. Res. Lett.*, **32**(23), L23S08 (doi: 10.1029/2005GL025070)
- Glasser NF and Scambos TA (2008) A structural glaciological analysis of the 2002 Larsen B ice-shelf collapse. *J. Glaciol.*, **54**(184), 3–16 (doi: 10.3189/002214308784409017)
- Glasser N and 7 others (2009) Surface structure and stability of the Larsen C ice shelf, Antarctic Peninsula. *J. Glaciol.*, **55**(191), 400–410 (doi: 10.3189/002214309788816597)
- Hawley RL and Morris EM (2006) Borehole optical stratigraphy and neutron-scattering density measurements at Summit, Greenland. *J. Glaciol.*, **52**(179), 491–496 (doi: 10.3189/172756506781828368)

- Hawley RL, Waddington ED, Alley RA and Taylor KC (2003) Annual layers in polar firn detected by borehole optical stratigraphy. *Geophys. Res. Lett.*, **30**(15), 1788 (doi: 10.1029/2003GL017675)
- Holland PR, Corr HFJ, Vaughan DG, Jenkins A and Skvarca P (2009) Marine ice in Larsen Ice Shelf. *Geophys. Res. Lett.*, **36**(11), L11604 (doi: 10.1029/2009GL038162)
- Hubbard B, Roberson S, Samyn D and Merton-Lyn D (2008) Digital optical televiewing of ice boreholes. *J. Glaciol.*, **54**(188), 823–830 (doi: 10.3189/002214308787779988)
- Jenkins A and 6 others (2010) Observations beneath Pine Island Glacier in West Antarctica and implications for its retreat. *Nature Geosci.*, **3**(7), 468–472 (doi: 10.1038/ngeo890)
- Khazendar A and Jenkins A (2003) A model of marine ice formation within Antarctic ice shelf rifts. *J. Geophys. Res.*, **108**(C7), 3235 (doi: 10.1029/2002JC001673)
- Khazendar A, Tison JL, Stenni B, Dini M and Bondesan A (2001) Significant marine-ice accumulation in the ablation zone beneath an Antarctic ice shelf. *J. Glaciol.*, **47**(158), 359–368 (doi: 10.3189/172756501781832160)
- Khazendar A, Rignot E and Larour E (2007) Larsen B Ice Shelf rheology preceding its disintegration inferred by a control method. *Geophys. Res. Lett.*, **34**(19), L19503 (doi: 10.1029/2007GL030980)
- Leonard KC, Tremblay L-B, MacAyeal DR and Jacobs SS (2008) Interactions of wind-transported snow with a rift in the Ross Ice Shelf, Antarctica. *Geophys. Res. Lett.*, **35**(5), L05501 (doi: 10.1029/2007GL033005)
- Morgan VI (1972) Oxygen isotope evidence for bottom freezing on the Amery Ice Shelf. *Nature*, **238**(5364), 393–394
- Oerter H and 6 others (1992) Evidence for basal marine ice in the Filchner–Ronne Ice Shelf. *Nature*, **358**(6385), 399–401
- Pattyn F, de Brabander S and Huyghe A (2005) Basal and thermal control mechanisms of the Ragnhild Glaciers, East Antarctica. *Ann. Glaciol.*, **40**, 225–231 (doi: 10.3189/172756405781813672)
- Roberson S and Hubbard B (2010) Application of borehole optical televiewing to investigating the 3-D structure of glaciers: implications for the formation of longitudinal debris ridges, Midre Lovénbreen, Svalbard. *J. Glaciol.*, **56**(195), 143–156 (doi: 10.3189/002214310791190802)
- Roberts D, Craven M, Cai M-H, Allison I and Nash G (2007) Protists in the marine ice of the Amery Ice Shelf, East Antarctica. *Polar Biol.*, **30**(2), 143–153 (doi: 10.1007/s00300-006-0169-7)
- Shabtaie S and Bentley CR (1982) Tabular icebergs: implications from geophysical studies of ice shelves. *J. Glaciol.*, **28**(100), 413–430
- Tabraham J (1998) The desalination of marine ice. (PhD thesis, University of Cambridge)
- Tison J-L, Ronveaux D and Lorrain RD (1993) Low salinity frazil ice generation at the base of a small Antarctic ice shelf. *Antarct. Sci.*, **5**(3), 309–322
- Tison JL, Khazendar A and Roulin E (2001) A two-phase approach to the simulation of the combined isotope/salinity signal of marine ice. *J. Geophys. Res.*, **106**(C12), 31 387–31 401 (doi: 10.1029/2000JC000207)
- Treverrow A, Warner RC, Budd WF and Craven M (2010) Meteoric and marine ice crystal orientation fabrics from the Amery Ice Shelf, East Antarctica. *J. Glaciol.*, **56**(199), 877–890 (doi: 10.3189/002214310794457353)
- Van de Berg WJ, Van den Broeke MR, Reijmer CH and Van Meijgaard E (2006) Reassessment of the Antarctic surface mass balance using calibrated output of a regional atmospheric climate model. *J. Geophys. Res.*, **111**(D11), D111104 (doi: 10.1029/2005JD006495)
- Weeks WF (2010) *On sea ice*. University of Alaska Press, Fairbanks, AK

Radar characterization of the basal interface across the grounding zone of an ice-rise promontory in East Antarctica

Kenichi MATSUOKA,¹ Frank PATTYN,² Denis CALLENS,^{1,2} Howard CONWAY³

¹Norwegian Polar Institute, Fram Centre, Tromsø, Norway

²Laboratoire de Glaciologie, Université Libre de Bruxelles, Brussels, Belgium

³Department of Earth and Space Sciences, University of Washington, Seattle, WA, USA

ABSTRACT. Radar power returned from the basal interface along a 42 km long profile over an ice-rise promontory and the adjacent Roi Baudouin ice shelf, Dronning Maud Land, East Antarctica, is analyzed to infer spatial variations in basal reflectivity and hence the basal environment. Extracting basal reflectivity from basal returned power requires an englacial attenuation model. We estimate attenuation in two ways: (1) using a temperature-dependent model with input from thermomechanical ice-flow models; and (2) using a radar method that linearly approximates the geometrically corrected returned power with ice thickness. The two methods give different results. We argue that attenuation calculated using a modeled temperature profile is more robust than the widely used radar method, especially in locations where depth-averaged attenuation varies spatially or where the patterns of basal reflectivity correlate with the patterns of the ice thickness.

INTRODUCTION

Grounding zones are located between the most landward site of ice flexure from tidal movement and the most landward site where the ice reaches approximate hydrostatic equilibrium (Vaughan, 1994; Fricker and Padman, 2006). They are typically several kilometers long (Brunt and others, 2010), but can be as long as 20–30 km depending on the strength of tides and the elastic properties of ice (Sykes and others, 2009). Because the flow of upstream ice is strongly controlled by the grounding zones (e.g. Schoof, 2007) there is strong motivation to improve understanding of conditions at the basal interface across the grounding zones.

Interpretation of basal conditions across grounding lines from radar data is complicated because the basal interface in the vicinity of grounding zones is subject to influences from ocean water, sediment-rich glacier meltwater from upstream, sediments and bedrock properties. For example, MacGregor and others (2011) examined radar power returned from the basal interface along 11 profiles across the Siple Coast (West Antarctica) grounding zone. Results showed no strong contrast in basal reflectivity, which was attributed to a thin (~ 0.2 m) water film that extended several kilometers upstream of the grounding zone.

Here we present radar data collected across an ice-rise promontory and the adjacent ice shelf in Dronning Maud Land, East Antarctica (Fig. 1). To derive a proxy of basal conditions, we calculated englacial attenuation using two different methods: one employs a widely used radar algorithm and the other uses a temperature-dependent attenuation model with input from thermomechanical ice-flow models. We discuss the differences in basal conditions inferred from these methods.

METHODS

Radar/GPS profiling

A 42 km long profile was made from the ice-rise promontory to the adjacent ice shelf (Figs 1 and 2). We used a 5 MHz ground-based radar-profiling system positioned with a geodetic L1 GPS receiver (Pattyn and others, 2010). Radio-wave

propagation speed in ice is assumed to be $168.4 \text{ m } \mu\text{s}^{-1}$, which corresponds to permittivity of 3.17. Surface topography was determined by a kinematic GPS survey using a temporary base station located near the crest of the ice promontory. The position of the base station in the International Terrestrial Reference Frame was determined by the Precise Point Positioning method. Earth Gravitational Model 1996 (EGM96) shows that the geoid height is ~ 24 m above the World Geodetic System 1984 ellipsoidal elevation (WGS84) in the vicinity of the grounding zone and the floating ice that we surveyed. Therefore, we added 24 m to the GPS-measured elevations in order to derive elevations relative to regional sea level.

The measured radar power P_{basal} returned from the base of the ice column is affected by instrumental factors S , geometrical factors G_{basal} , two-way englacial attenuation L_{ice} and basal reflectivity R_{basal} . The relationship between these factors in the decibel scale ($[x]_{\text{dB}} = 10 \log_{10} x$) can be written as (e.g. Matsuoka and others, 2010)

$$[P_{\text{basal}}]_{\text{dB}} = [S]_{\text{dB}} - [G_{\text{basal}}]_{\text{dB}} - [L_{\text{ice}}]_{\text{dB}} + [R_{\text{basal}}]_{\text{dB}}. \quad (1)$$

Figure 2a shows the absence of englacial scatters such as buried crevasses, so losses from L_{ice} and G_{basal} are expected to dominate. The ratio of the ice thickness (up to 700 m) to the radio-wave wavelength (~ 30 m) is small, so extinction of power due to birefringence caused by alignments of ice crystals is probably insignificant (Matsuoka and others, 2009a). Therefore, Equation (1) is a reasonable approximation for our analysis.

The geometric factor G_{basal} is a function of ice thickness H and depth-averaged permittivity ε (assumed to be 3.17): $[G_{\text{basal}}]_{\text{dB}} = 2[H/\sqrt{\varepsilon}]_{\text{dB}}$. $[G_{\text{basal}}]_{\text{dB}}$ varies by ~ 10 dB for ice-thickness variations between 200 and 700 m, but it is negligibly affected by possible variations of the depth-averaged permittivity (i.e. density). Therefore, assuming that instrumental factors S remain stable over time, variations in the geometrically corrected returned power P_{basal}^c are caused by variations in englacial attenuation and basal reflectivity:

$$[P_{\text{basal}}^c]_{\text{dB}} \propto -[L_{\text{ice}}]_{\text{dB}} + [R_{\text{basal}}]_{\text{dB}}. \quad (2)$$

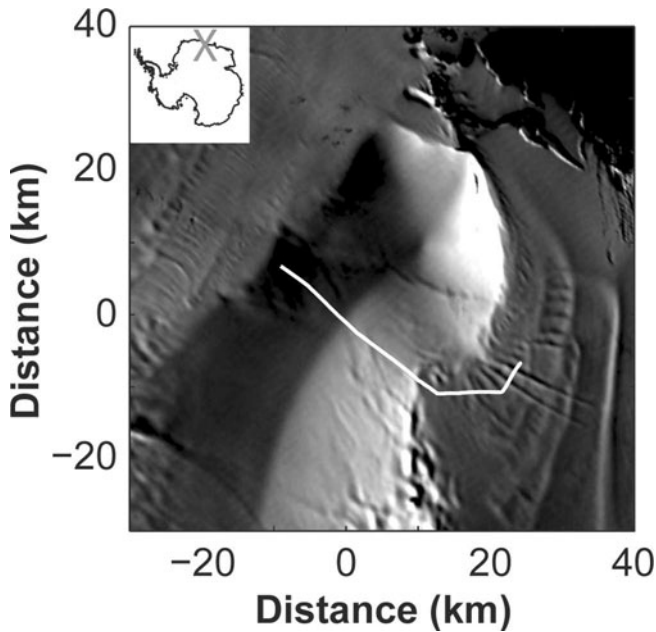


Fig. 1. Study area. The radar profile crosses an ice-rise promontory and the adjacent Roi Baudouin ice shelf in Dronning Maud Land. Background image is a Moderate Resolution Imaging Spectroradiometer (MODIS) satellite mosaic (Haran and others, 2006). Origin of the local coordinate is the site where the radar profile crosses the topographical crest (70.66° S, 23.92° E). Inset shows the location in Antarctica.

Values for $\mathcal{P}_{\text{basal}}^c$ come from measurements of returned power and ice thickness (calculated from the two-way travel time). Here we derive an accurate estimate L_{ice} in order to calculate $[\mathcal{P}_{\text{basal}}^c]_{\text{dB}} + [L_{\text{ice}}]_{\text{dB}}$ along the profile, thereby providing a proxy of spatial variations of $[R_{\text{basal}}]_{\text{dB}}$.

Attenuation estimates

We estimated depth-averaged englacial attenuation rates in two ways. The first method uses measurements of the geometrically corrected returned power as a function of ice thickness (e.g. Winebrenner and others, 2003; Jacobel and others, 2009). The thickness dependence of the returned power $\langle d[\mathcal{P}_{\text{basal}}^c]_{\text{dB}}/dH \rangle$ can be used as a proxy for englacial attenuation if the basal reflectivity is independent of ice thickness, that is when $\langle d[R_{\text{basal}}]_{\text{dB}}/dH \rangle = 0$, $\langle d[\mathcal{P}_{\text{basal}}^c]_{\text{dB}}/dH \rangle = \langle -d[L_{\text{ice}}]_{\text{dB}}/dH \rangle$ (Equation (2)). This method is appropriate when englacial losses (e.g. scattering from buried crevasses) other than C_{basal} and L_{ice} are significant (e.g. Raymond and others, 2006).

The second method uses an attenuation model that depends on depth profiles of ice temperature and chemistry. Englacial attenuation is a result of contributions from pure ice, acidity and sea salt in the ice column, which have different temperature dependences. However, the lack of information on depth profiles of chemistry precludes calculating the contributions from acidity and sea salt, and here we consider only the pure-ice contribution. Acidity and sea salt contribute 26% and 21% of the total depth-averaged attenuation rate at Siple Dome and Vostok ice-core sites, respectively (Matsuoka and others, 2011). The local one-way attenuation rate N (dB km^{-1}) is

$$N = 0.914\sigma_{\text{pure}} \exp \left[-E_{\text{pure}}/k(1/T - 1/T_r) \right]. \quad (3)$$

Here $\sigma_{\text{pure}} = 9.2 \mu\text{s m}^{-1}$, $E_{\text{pure}} = 0.51 \text{ eV}$, $T_r = 251 \text{ K}$ and k is

the Boltzmann constant (MacGregor and others, 2007; Matsuoka, 2011). These values have significant uncertainties because there are few published measurements of the temperature dependence of dielectric properties. Consequently, uncertainty in attenuation sensitivity to ice temperature and in estimated attenuation is also large. We ignore this uncertainty in the analysis below.

The ice temperature T for the attenuation model (Equation (3)) is calculated using a two-dimensional (2-D) thermomechanical high-order model (Pattyn, 2002, 2003). The model calculates the horizontal velocity field in the ice sheet using higher-order physics, taking into account vertical shearing as well as longitudinal stress gradient. The velocity fields for both the ice sheet and ice shelf are derived simultaneously. Vertical velocities are obtained from mass conservation and by considering the present-day ice topography in steady state (Hindmarsh, 1999). The velocity field is fully coupled to the temperature field, based on vertical diffusion, horizontal and vertical advection and friction. Flow enhancement factor m is assumed to be uniform at 0.8 or 1.0. Boundary conditions to the ice-flow field are obtained from balance velocity calculations at either side of the profile presented in Figure 2, and a basal friction parameter at the bottom, relating basal velocities to basal shear stress (Pattyn and others, 2006). Basal friction in the ice shelf is set to be zero.

Surface temperature T_s over the entire profile and geothermal flux GF over the grounded ice are assumed to be uniform: $T_s = -12^\circ\text{C}$ and $\text{GF} = 42$ or 54 mW m^{-2} . Since the model is not coupled with the ocean, a temperature of -2°C , an approximate melting point of sea water corrected for pressure at depth, is prescribed at the ice–water interface of floating ice. In this area, neither measurements nor model estimates of ocean temperature have been made. Surface accumulation rates are determined from the shallowest radar-reflector pattern and a regional mean of the recent accumulation rate of 0.27 m a^{-1} from a continental mass-balance model (Pattyn and others, in press). For each geothermal flux and flow-enhancement factor, the model was run more than 20 000 years until the ice-flow and temperature fields reached a steady state.

The radar transect across the ice promontory was aligned perpendicular to surface contours, which is an approximation of the ice-flow direction. However, the radar transect on the ice shelf may deviate from the flowline. There are no depth variations of ice-flow speed over the ice shelf (plug flow), so the vertical velocity profile is linear so that the steady-state depth profile of temperature is a function of vertical advection rates and constrained by the upper and lower surface temperatures, regardless of the upstream ice-flow field (e.g. Hindmarsh, 1999). Therefore, the effects of transverse stress coupling and the deviation of the radar profile from the true flowline on the estimated temperature field are expected to be small, as horizontal (advection) effects are negligible.

RESULTS AND DISCUSSION

Radar and GPS measurements

Figure 2a shows a radargram with surface elevation adjustments using GPS-measured surface elevations z_s . Figure 2b shows details of the surface topography in the vicinity of the grounding zone, and Figure 2c shows $\delta z = z_s - z_{\text{float}}$, where

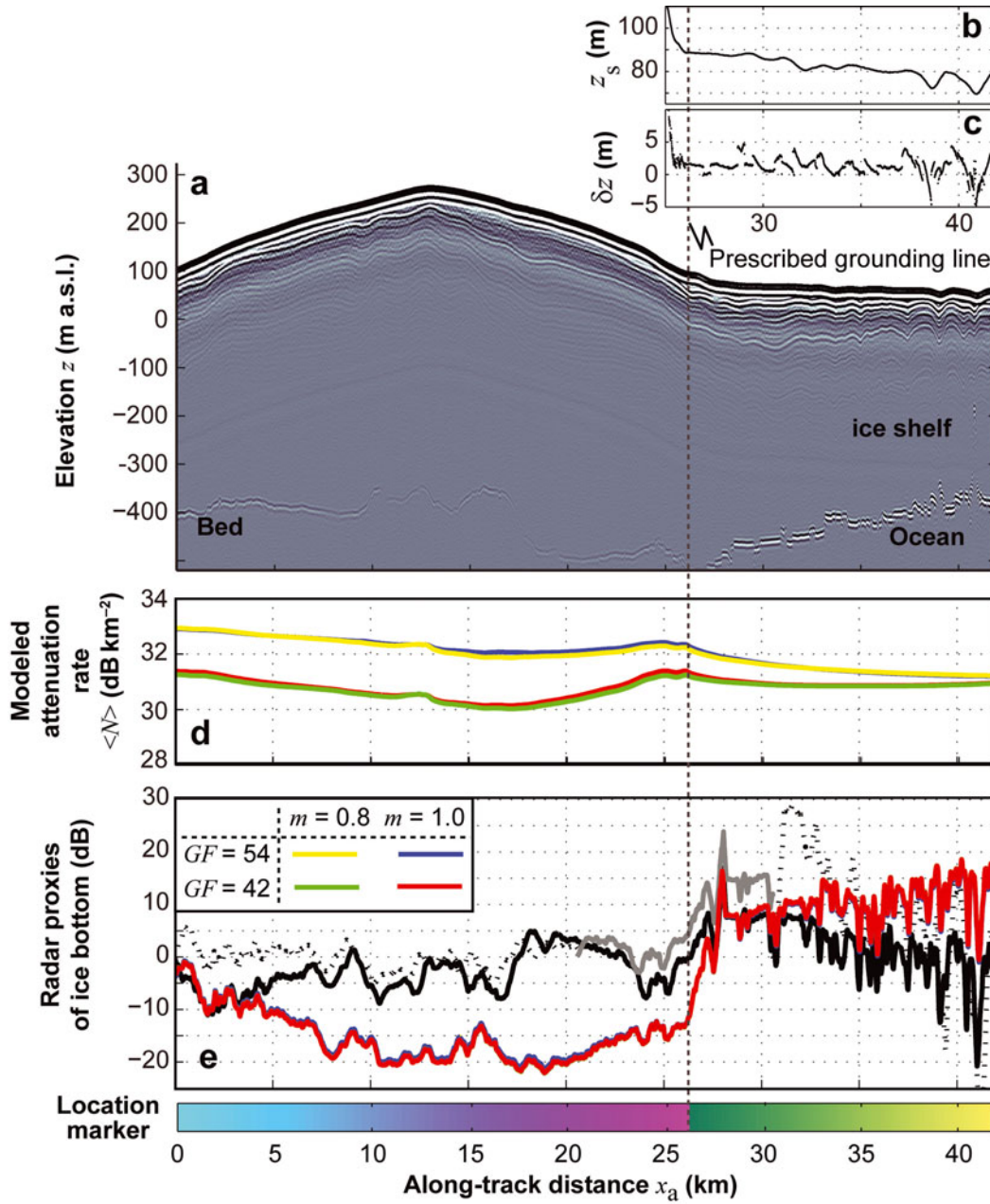


Fig. 2. Observed and modeled properties along the radar profile. The location marker is referred to in Figure 4. (a) Radargram is adjusted to account for surface elevation variations. (b) Detailed surface topography of the grounding zone and floating ice. (c) $\delta z = z_s - z_{\text{float}}$, where z_s is the measured ice-surface elevation and z_{float} is the thickness of freely floating ice (Equation (4)). Vertical gray dashed line shows where ice becomes freely floating. (d) Depth-averaged attenuation rates $\langle N \rangle$ estimated using ice-flow models for geothermal fluxes $GF = 42$ and 54 mW m^{-2} and for ice-flow enhancement factors m of 0.8 and 1.0. Results for different m are nearly identical. Color legend is as shown in (e). (e) Estimated relative reflectivity $[R_{\text{basal}}]_{\text{dB}}$ using attenuation models. Also shown are anomalous basal returned power ($\Delta[P_{\text{basal}}]_{\text{dB}}$) values (Equation (5)) estimated using a widely used radar method for four data ensembles (Fig. 4): the black solid curve is for the entire dataset, the two dashed curves are for grounded and floating ice, respectively, excluding the vicinity (5 km) of the grounding line, and the gray curve is for the vicinity (± 5 km) of the grounding line. $[R_{\text{basal}}]_{\text{dB}}$ and $\Delta[P_{\text{basal}}]_{\text{dB}}$ shown here are filtered with a 1 km running average.

z_{float} is the thickness of freely floating ice that can be derived from the ice thickness H and densities of ice ρ_i and of ocean water ρ_w :

$$z_{\text{float}} = (\rho_w - \rho_i) / \rho_w \times H. \quad (4)$$

When ice is in hydraulic equilibrium (and all ρ_i , ρ_w and H are accurate), δz is zero. In earlier work we showed that δz is minimal over the downstream side ($x_a > 25.6$ km) of this profile (Pattyn and others, in press). At landward sites ($x_a < 25.6$ km), δz increases rapidly, so the ice is no longer

in hydrostatic equilibrium. Therefore, we determined that the most landward site of freely floating ice is at $x_a = 25.6$ km.

We did not find a topographic minimum or a break in slope associated with the non-hydrostatic ice flexure response typically found in grounding zones (Brunt and others, 2010). Although our repeat GPS profiles between the ice promontory and the ice shelf do show some changes in elevation at sites landward of freely floating ice, they do not allow us to determine the most landward site affected by tidal forcing.

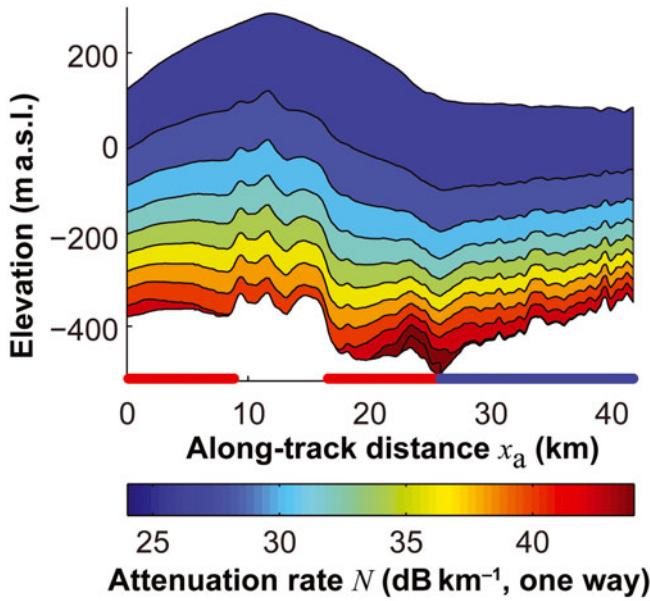


Fig. 3. Variations in local attenuation rate N estimated for geothermal flux of 54 mW m^{-2} and flow-enhancement factor of 1.0. Red and blue markers along the abscissa show locations where the basal ice is at the (pressure-)melting point over grounded and floating ice, respectively.

Attenuation estimates using thermomechanical model

Figure 3 shows englacial attenuation rates N estimated using the thermomechanical model for $(GF, m) = (54 \text{ mW m}^{-2}, 1.0)$. In the model, we prescribe the grounding line at $x_a = 25.6 \text{ km}$, although in reality it is slightly landward of this position. Ice temperature increases with depth monotonically, as does the attenuation rate. The model predicts that the basal temperature of grounded ice is at the pressure-melting point, except for the vicinity of the ice-rise crest when the geothermal flux is 54 mW m^{-2} regardless of the flow-enhancement factor. For a geothermal flux of 42 mW m^{-2} , the basal temperature of the grounded ice is below the pressure-melting point by several degrees.

Figure 2d shows the spatial pattern of depth-averaged attenuation rate $\langle N \rangle$, which is derived by integrating local attenuation rates N (Fig. 3) vertically at sites along the profile. Total attenuation $[L_{\text{ice}}]_{\text{dB}}$ is proportional to the ice thickness H and the depth-averaged attenuation rate $\langle N \rangle$: $[L_{\text{ice}}]_{\text{dB}} = 2\langle N \rangle H$ (the factor of 2 is to account for the two-way travel). Although $\langle N \rangle$ increases with geothermal flux GF and decreases with flow-enhancement factor m , the amplitudes of $\langle N \rangle$ variations along the profile are 1.3–1.7 dB km^{-1} and the spatial pattern remains similar regardless of GF and m (Fig. 2d). Differences in the flow-enhancement factors have negligible effects on $\langle N \rangle$.

It is still an open question whether the temperature in Equation (3) is relative to the pressure-melting point, because all dielectric properties used to determine σ_{pure} and E_{pure} were measured with meteoric or laboratory-grown ice at the standard atmospheric pressure, so the (pressure-)melting point of the ice specimen for those measurements is close to 0°C . If an attenuation approximation (Equation (3)) is more appropriate for temperature relative to the pressure-melting point, then the estimated variations in $\langle N \rangle$ over the shelf ice would be larger than those shown in Figure 2 by $\sim 1 \text{ dB km}^{-1}$. This difference is nearly uniform along the

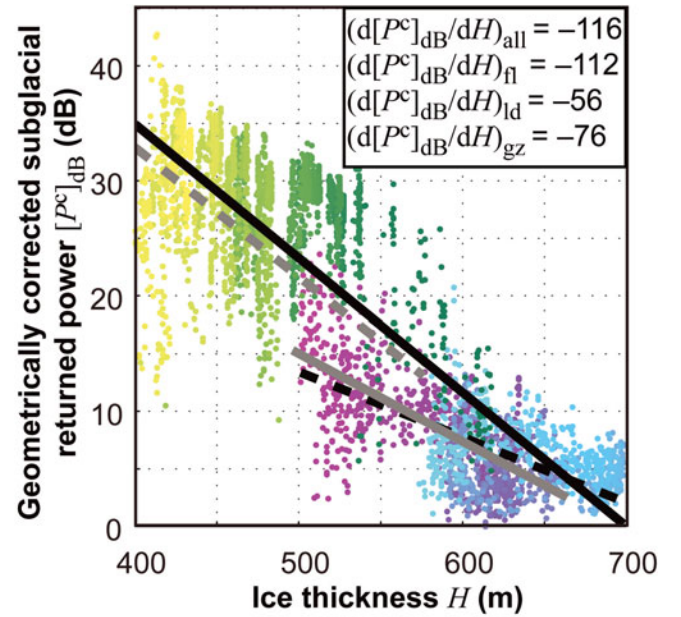


Fig. 4. Ice-thickness dependence of geometrically corrected radar power returned from the basal interface. Colors represent the location along the profile (Fig. 2). Solid black line shows linear fit for the entire dataset. Black and gray dashed lines show fits for grounded and floating ice, respectively, excluding the grounding-line vicinity (5 km). Solid gray line shows fit in the vicinity ($\pm 5 \text{ km}$) of the grounding line. Inset shows the slope of these lines (unit: dB km^{-1} for round trip); half of these values are frequently used as one-way attenuation rate $\langle N \rangle$.

profile, so this uncertainty in the attenuation parameterization (Equation (3)) does not significantly affect our interpretations of the basal environment.

Basal returned power dependence on ice thickness

Figure 4 shows basal returned power dependence on ice thickness $\langle d[P_{\text{basal}}^c]_{\text{dB}}/dH \rangle$ for four linear fits: (1) for the entire dataset; (2) for floating ice 5 km or more seaward of the prescribed grounding line; (3) for grounded ice 5 km or more landward of the grounding line; and (4) in the vicinity ($\pm 5 \text{ km}$) of the grounding line. The attenuation rate $\langle N \rangle$ ($= -\langle d[P_{\text{bed}}^c]_{\text{dB}}/dH \rangle/2$) varies by a factor of 2, depending on the choice of data ensembles used in the fit (Fig. 4): 58 dB km^{-1} (all data), 56 dB km^{-1} (floating ice), 38 dB km^{-1} (grounding zone) and 28 dB km^{-1} (grounded ice). In contrast, results from the temperature-dependent attenuation model (Equation (3)) indicate relatively uniform depth-averaged values, 30–33 dB km^{-1} (Fig. 2d). As discussed earlier, the temperature-dependent attenuation model used here does not account for contributions from ice chemistry, which could increase these calculated $\langle N \rangle$ by $\sim 10 \text{ dB km}^{-1}$ if sea salt of $17 \mu\text{mol L}^{-1}$ is included in the ice.

The thickness dependence of the basal returned power does not give a regional mean attenuation rate when the attenuation rates vary significantly in the data ensemble or the bed reflectivity depends on ice thickness (Matsuoka, 2011). Along our profile, the attenuation rate estimated from the attenuation temperature model is nearly uniform within $\pm 1 \text{ dB km}^{-1}$ (Fig. 2d). However, the grounded ice is generally thicker than the floating ice, and a significant thickness variation is found in the floating ice (Fig. 4; color of markers show the locations along the profile (see Fig. 2)). These

features yield apparent thickness dependence of the basal reflectivity, which is a likely reason why attenuation rates estimated with the thickness dependences of the basal returned power do not match well with the model estimates.

Inferring conditions at the basal interface

Although the radar instrument factor is unknown, the transmitter used here is known to be stable (Matsuoka and others, 2009b). So, $[P_{\text{basal}}^c]_{\text{dB}} + [L_{\text{ice}}]_{\text{dB}}$ provides a proxy of spatial variations of $[R_{\text{basal}}]_{\text{dB}}$ (Equation (1)). The anomalous basal returned power $\Delta[P_{\text{basal}}^c]_{\text{dB}}$ from values predicted with the traditional radar method (Fig. 4) also provides a proxy of spatial variations of $[R_{\text{basal}}]_{\text{dB}}$:

$$\Delta[P_{\text{basal}}^c]_{\text{dB}} = [P_{\text{basal}}^c]_{\text{dB}} - \langle d[P_{\text{basal}}^c]_{\text{dB}}/dH \rangle H. \quad (5)$$

Figure 2e shows $\Delta[P_{\text{basal}}^c]_{\text{dB}}$ anomalies from the mean of $[P_{\text{basal}}^c]_{\text{dB}}$ for each data ensemble along the profile as a proxy of relative basal reflectivity. Attenuation-rate estimates depend on the geothermal flux (Fig. 2d), but the spatial patterns of $[R_{\text{basal}}]_{\text{dB}}$ estimated here are not sensitive to the magnitude of the geothermal flux because the ‘pattern’ of $\langle N \rangle$ is controlled primarily by the ‘pattern’ of ice thickness and accumulation rate.

Figure 2e shows four distinct features in $[R_{\text{basal}}]_{\text{dB}}$ estimated with attenuation modeling and in $\Delta[P_{\text{basal}}^c]_{\text{dB}}$. First, $\Delta[P_{\text{basal}}^c]_{\text{dB}}$ for the entire dataset show similar values for the grounded ice and floating ice in general, although basal conditions for the grounded and floating ice are presumably distinct. Near the profile end on the floating ice ($x_a > \sim 35$ km), $\Delta[P_{\text{basal}}^c]_{\text{dB}}$ for the entire profile and for the floating ice are smaller than for the grounded ice. However, radar-measured ice thickness gives surface elevation for the freely floating ice consistent with the GPS-measured elevation over this area (Fig. 2b). The presence of marine ice is therefore unlikely, and basal conditions should be more or less constant over the floating ice. Also, attenuation estimates used for these $\Delta[P_{\text{basal}}^c]_{\text{dB}}$ over the entire profile and over the floating ice are extremely high (56–58 dB km⁻¹ for one way). Therefore, we conclude that these $\Delta[P_{\text{basal}}^c]_{\text{dB}}$ values for the entire dataset and for the floating ice do not represent variations in the basal conditions.

Second, $\Delta[P_{\text{basal}}^c]_{\text{dB}}$ for the grounding-line vicinity varies ~ 20 dB. This variation happens in the horizontal distance of ~ 5 km. A similar feature is found in $[R_{\text{basal}}]_{\text{dB}}$ estimated with attenuation modeling. In the grounding-line vicinity, the modeling predicts an attenuation variation less than 1 dB km⁻¹ for one way; the ice thickness varies < 150 m in this area, giving minimal variations in the total attenuation $[L_{\text{ice}}]_{\text{dB}}$ within the grounding zone. Thus, the predicted variations in $[R_{\text{basal}}]_{\text{dB}}$ are essentially identical to variations in $[P_{\text{basal}}^c]_{\text{dB}}$. In practice, basal reflectivity is insensitive to the attenuation estimates in such areas where the ice thickness and attenuation rate vary little.

Third, $[R_{\text{basal}}]_{\text{dB}}$ estimated with attenuation modeling has a broad minimum near the crest ($x_a = \sim 12$ km). It becomes larger towards both ends of the profile over the grounded ice. This pattern is also found in the modeled basal temperature, when geothermal flux is 54 mW m⁻² (Fig. 3). The range of $[R_{\text{basal}}]_{\text{dB}}$ over the grounded ice is ~ 20 dB from the crest to the western end of the profile and 10 dB from the crest to the grounding line. However, basal reflectivity is related to the local amount of water, rather than local melting rate, so our 2-D modeling cannot be used to constrain the flow-model parameters such as geothermal

flux, which alter the ice temperature, using the pattern of the observed bed reflectivity.

Finally, variations of $\Delta[P_{\text{basal}}^c]_{\text{dB}}$ depend on data ensembles used for constructing the fit between returned power and ice thickness (Fig. 4). For example, $\langle d[P_{\text{basal}}^c]_{\text{dB}}/dH \rangle H$ derived for the floating ice is -144 or -112 dB km⁻¹ when the data ensemble includes or excludes, respectively, the 5 km portion of the profile close to the grounding line. However, $\langle d[P_{\text{basal}}^c]_{\text{dB}}/dH \rangle H$ derived for the grounded ice varies only 3 dB km⁻¹ if the data ensemble includes or excludes the grounding-line vicinity. Therefore, the analysis of the spatial pattern of $\Delta[P_{\text{basal}}^c]_{\text{dB}}$ is not rigorous. $[R_{\text{basal}}]_{\text{dB}}$ derived from four modeled temperature-dependent attenuation rates show similar spatial patterns (Fig. 2e). These results suggest that basal conditions revealed by the temperature-dependent attenuation modeling are robust despite uncertainties in the modeling parameters and boundary conditions.

CONCLUSIONS

A sharp increase in basal reflectivity was found in the vicinity of the grounding zone using a temperature-dependent attenuation model in combination with a thermomechanical model to estimate temperature profiles in the ice. This increase is consistent with a step change in the basal environment from a grounded (possibly wet) bed to an ice–ocean interface. This conclusion is robust even with the inherent uncertainties in the model, such as geothermal flux, flow-enhancement factor and location of the grounding line. Such a step change is also detected using a traditional radar method that assumes uniform attenuation rate, probably because variations in attenuation in this area are minimal. However, the radar method and temperature-dependent modeling give distinctly different patterns of anomalous basal reflectivity over the grounded ice and over the floating ice. The results argue strongly for a temperature-dependent attenuation model, when the radar returned power is analyzed to extract a proxy of basal conditions.

ACKNOWLEDGEMENTS

We acknowledge logistic support from the Belgian Antarctic Research Expedition (BELARE). This project was supported by the Belgian Federal Science Policy Office (grant No.: EA/11/3A), the University of Washington Royalty fund (grant No.: 4208) and the Center for Ice, Climate and Ecosystems at the Norwegian Polar Institute. We are indebted to A. Hubert, R. Wagemans, K. Soete and other BELARE field participants for assistance in the field. D.C. is funded by an FNRS–FRIA scholarship and by the YGGDRASIL mobility program, Research Council of Norway. Comments by Sasha Carter, an anonymous reviewer and the scientific editor, Poul Christoffersen, improved the paper significantly.

REFERENCES

- Brunt KM, Fricker HA, Padman L, Scambos TA and O’Neel S (2010) Mapping the grounding zone of Ross Ice Shelf, Antarctica, using ICESat laser altimetry. *Ann. Glaciol.*, **51**(55), 71–79
- Fricker HA and Padman L (2006) Ice-shelf grounding zone structure from ICESat laser altimetry. *Geophys. Res. Lett.*, **33**(15), L15502 (doi: 10.1029/2006GL026907)

- Haran T, Bohlander J, Scambos T, Painter T and Fahnestock M (2006) *MODIS mosaic of Antarctica (MOA) image map*. National Snow and Ice Data Center, Boulder, CO. Digital media
- Hindmarsh RCA (1999) On the numerical computation of temperature in an ice sheet. *J. Glaciol.*, **45**(151), 568–574
- Jacobel RW, Welch BC, Osterhouse D, Pettersson R and MacGregor JA (2009) Spatial variation of radar-derived basal conditions on Kamb Ice Stream, West Antarctica. *Ann. Glaciol.*, **50**(51), 10–16
- MacGregor JA, Winebrenner DP, Conway H, Matsuoka K, Mayewski PA and Clow GD (2007) Modeling englacial radar attenuation at Siple Dome, West Antarctica, using ice chemistry and temperature data. *J. Geophys. Res.*, **112**(F3), F03008 (doi: 10.1029/2006JF000717)
- MacGregor JA, Anandakrishnan S, Catania GA and Winebrenner DP (2011) The grounding zone of the Ross Ice Shelf, West Antarctica, from ice-penetrating radar. *J. Glaciol.*, **57**(205), 917–928
- Matsuoka K, Gades A, Conway H, Catania G and Raymond C (2009a) Radar signatures beneath a surface topographic lineation near the outlet of Kamb Ice Stream and Engelhardt Ice Ridge, West Antarctica. *Ann. Glaciol.*, **50**(51), 98–104
- Matsuoka K, Wilen L, Hurley SP and Raymond CF (2009b) Effects of birefringence within ice sheets on obliquely propagating radio waves. *IEEE Trans. Geosci. Remote Sens.*, **47**(5), 1429–1443
- Matsuoka K, Morse D and Raymond CF (2010) Estimating englacial radar attenuation using depth profiles of the returned power, central West Antarctica. *J. Geophys. Res.*, **115**(F2), F02012 (doi: 10.1029/2009JF001496)
- Matsuoka K (2011) Pitfalls in radar diagnosis of ice-sheet bed conditions: lessons from englacial attenuation models. *Geophys. Res. Lett.*, **38**(5), L05505 (doi: 10.1029/2010GL046205)
- Matsuoka K, MacGregor JA and Pattyn F (2011) Using englacial radar attenuation to better diagnose the subglacial environment: a review. In Crocco L ed. *Proceedings of the 13th International Conference on Ground Penetrating Radar (GPR), 21– 25 June 2010, Lecce, Italy*. Institute of Electrical and Electronics Engineers, Piscataway, NJ, 1–5
- Pattyn F (2002) Transient glacier response with a higher-order numerical ice-flow model. *J. Glaciol.*, **48**(162), 467–477
- Pattyn F (2003) A new three-dimensional higher-order thermo-mechanical ice-sheet model: basic sensitivity, ice stream development, and ice flow across subglacial lakes. *J. Geophys. Res.*, **108**(B8), 2382
- Pattyn F, Huyghe A, de Brabander S and De Smedt B (2006) Role of transition zones in marine ice sheet dynamics. *J. Geophys. Res.*, **111**(F2), F02004 (doi: 10.1029/2005JF000394)
- Pattyn F, Matsuoka K and Berte J (2010) Glacio-meteorological conditions in the vicinity of the Belgian Princess Elisabeth Station, Antarctica. *Antarct. Sci.*, **22**(1), 79–85
- Pattyn F and 8 others (in press) Radar and ice-core evidence for active ice–ocean interaction under the Roi Baudouin Ice Shelf, East Antarctica. *J. Geophys. Res. Earth Surf.*
- Raymond CF, Catania GA, Nereson N and Van der Veen CJ (2006) Bed radar reflectivity across the north margin of Whillans Ice Stream, West Antarctica, and implications for margin processes. *J. Glaciol.*, **52**(156), 3–10
- Schoof C (2007) Ice-sheet grounding-line dynamics: steady states, stability, and hysteresis. *J. Geophys. Res.*, **112** (F3), F03S28 (doi: 10.1029/2006JF000664)
- Sykes HJ, Murray T and Luckman A (2009) The location of the grounding zone of Evans Ice Stream, Antarctica, investigated using SAR interferometry and modelling. *Ann. Glaciol.*, **50**(52), 35–40
- Vaughan DG (1994) Investigating tidal flexure on an ice shelf using kinematic GPS. *Ann. Glaciol.*, **20**, 372–376
- Winebrenner DP, Smith BE, Catania GA, Conway HB and Raymond CF (2003) Radio-frequency attenuation beneath Siple Dome, West Antarctica, from wide-angle and profiling radar observations. *Ann. Glaciol.*, **37**, 226–232

Glacio-meteorological conditions in the vicinity of the Belgian Princess Elisabeth Station, Antarctica

FRANK PATTYN^{1*}, KENICHI MATSUOKA² and JOHAN BERTE³

¹Laboratoire de Glaciologie, Département des Sciences de la Terre et de l'Environnement, Université Libre de Bruxelles, CP 160/03, Avenue F.D. Roosevelt 50, B-1050 Brussels, Belgium

²Department of Earth and Space Sciences, University of Washington, Box 35130, Seattle, WA 98195, USA

³International Polar Foundation, Rue des deux gares 120A, B-1070 Brussels, Belgium

*fpattyn@ulb.ac.be

Abstract: During two consecutive reconnaissance surveys in 2004 and 2005 and a revisit in 2008, the glaciological and meteorological conditions in the vicinity of the new Belgian Princess Elisabeth Station (71°57'S; 23°20'E) on Utsteinen Ridge were investigated. We set up an automatic weather station, measured the ice thickness around the Utsteinen Ridge, and established a mass balance stake network. These baseline investigations show that Utsteinen Ridge is a relatively sheltered spot from the main katabatic winds. Furthermore, winter temperature conditions are rather mild, confirming the coreless winter conditions of the Antarctic ice sheet. Mass balance is generally low (near zero) with a small accumulation to the east and relatively little ablation to the west of Utsteinen Ridge. Ice flow in the vicinity of the station is also minimal, since the Sør Rondane Mountains upstream of the station block most of the ice flow, a feature that is most apparent in the area where the station is situated. Measurements of the surface topography separated by four years show that the construction of the station seems to have a limited effect on the redistribution of snow around it. In view of the sheltered and safe ice conditions, the area is an ideal place for deploying field activities.

Received 13 February 2009, accepted 19 June 2009

Key words: glaciology, ice dynamics, mass balance, meteorology

Introduction

The East Antarctic ice sheet (EAIS) is traditionally considered a stable feature characterized by slow-moving interior ice with drainage through ice shelves across a grounding line and by a few faster-moving outlet glaciers. This idea of stability is based on the fact that the ice sheet is not a marine ice sheet, in contrast to the West Antarctic ice sheet (WAIS), which is grounded well below sea level in much of its interior (Weertman 1974, Mercer 1978, Schoof 2007). However, in many places in Dronning Maud Land, the EAIS is drained by large outlet glaciers with their bedrock lying well below sea level. Most of these so-called continental ice streams also exhibit a rather complex ice flow, where effects of longitudinal stress coupling cannot be ignored (Rippin *et al.* 2003, Pattyn & Naruse 2003, Pattyn *et al.* 2005). These ice streams cut through large gaps within a chain of mountains surrounding the East Antarctic continent that stretches from the Borg Massif in western Dronning Maud Land (5°W, 73°S) to the Yamato Mountains in eastern Dronning Maud Land (35°E, 72°S). Most of the ice flowing from the polar plateau is blocked by mountain ranges, which force ice flow either around (Pattyn *et al.* 2005) or through the mountain terrain (Pattyn *et al.* 1992, Pattyn & Declair 1995).

East Antarctic outlet glaciers of Dronning Maud Land show signs of accelerated mass loss. The Shirase Glacier

drainage basin, making up the border between eastern Dronning Maud Land and Enderby Land, drains through one of the fastest Antarctic glaciers, at flow speeds of $> 2700 \text{ m a}^{-1}$ (Fujii 1981). The central basin is characterized by large submergence velocities (Naruse 1979, Pattyn & Naruse 2003), and measurements further downstream (Nishio *et al.* 1989, Toh & Shibuya 1992) record thinning rates of 0.5 to 2.0 m a^{-1} below the 2800 m elevation contour. This thinning rate is confirmed by satellite radar altimetry for the period 1992–2003 (Wingham *et al.* 2006). However, no distinctive increase in net mass loss across the grounding line has been observed (Rignot *et al.* 2008). The thinning upstream and the associated increase in mass transport toward the grounding line may be counterbalanced by large melting rates at the grounding line. Large melting rates underneath the Shirase Glacier ice tongue have been reported by Rignot & Jacobs (2002). The result is a negative mass balance, but a relatively stable grounding line position.

Further to the east, the Ragnhild Glaciers (Fig. 1) are the major drainage features, diverting flow around the Sør Rondane massif. Flow speeds attain 100 m a^{-1} more than 200 km upstream of the grounding line (Pattyn *et al.* 2005), relatively high for East Antarctic glaciers. The ice shelf downstream of the Ragnhild glaciers shows signs of change: a comparison between 1965 Belgian maps and recent RADARSAT imagery (Jezek & RAMP Product

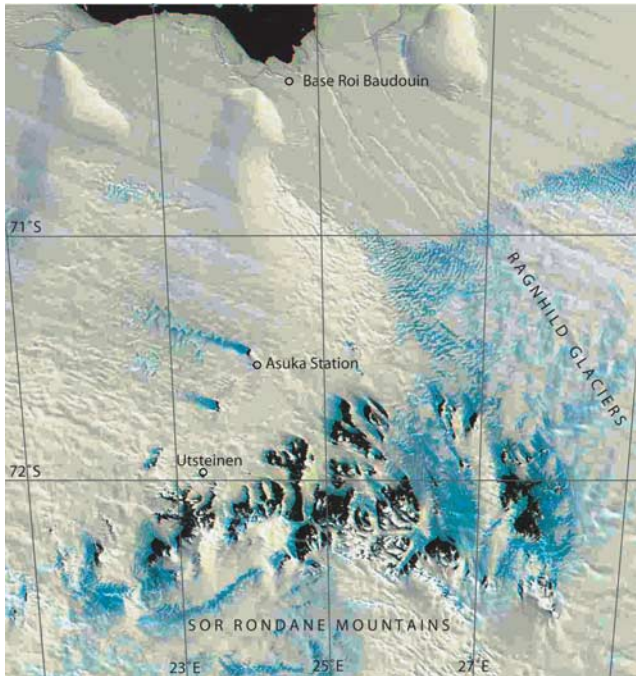


Fig. 1. MODIS image of the Sør Rondane Mountains including Breid Bay. Situation of the former Belgian Roi Baudouin Base, the former Japanese Asuka Station and the Utsteinen site of the new Belgian Princess Elisabeth Station ($71^{\circ}57'S$; $23^{\circ}20'E$).

Team 2002; <http://nsidc.org/data/nsidc-0103.html>) points to an acceleration in the west and a deceleration toward the east along the Princess Ragnhild Coast, indicating an eventual stoppage of the glaciers in the centre and the east of the catchment area. This may be provoked by ice piracy due to increased subglacial melting over the whole drainage basin (Pattyn *et al.* 2005).

The Sør Rondane Mountains are a 220 km long, east–west trending mountain range, situated 200 km from the coast. These mountains dam the main flow coming from the polar plateau (Fig. 1). This damming effect is clearly depicted by i) the stepwise topography of the glaciers (“ice fall”) at the southern rim where they cut through the Sør Rondane (Fig. 2), ii) the divergent ice flow pattern, and iii) the reduced mass transport through the mountain range (Pattyn *et al.* 1992).

Construction of Princess Elisabeth Station (PES) began just north of the Sør Rondane Mountains in 2006. This new Belgian research station is situated on a small, relatively flat, granite ridge (Utsteinen Ridge, $71^{\circ}57'S$; $23^{\circ}20'E$; 1390 m a.s.l.), approximately 1 km north of Utsteinen Nunatak, 173 km inland from the former Roi Baudouin base and 55 km from the former Japanese Asuka Station (Figs 1 & 3). Utsteinen Ridge - oriented in a north–south direction - is 700 m long, approximately 16 m wide and protrudes 20 m above the surrounding snow surface. The nearby Utsteinen Nunatak lies a few kilometres north of the

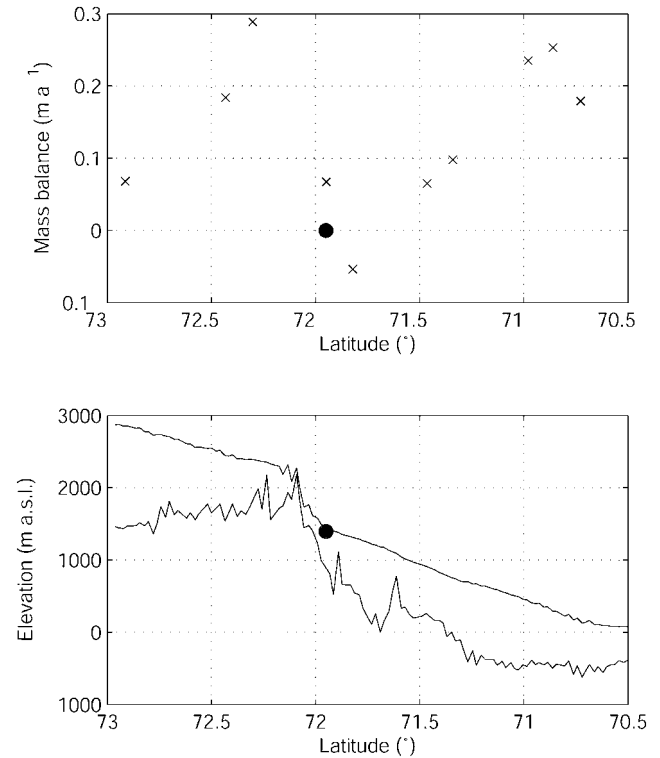


Fig. 2. Upper: Surface mass balance between $73^{\circ}S$ and $70^{\circ}S$ along the $23^{\circ}E$ meridian, based on regional atmospheric climate modelling (van de Berg *et al.* 2006). The grey dot shows the mass balance at Utsteinen. Lower: Surface and bedrock topographic profile along the same transect, based on Bamber *et al.* (2009) (surface topography) and Lythe & Vaughan (2001) (BEDMAP bed topography).



Fig. 3. View to the north of the Utsteinen Ridge and the Princess Elisabeth Station. The main wind direction is from the east (right side of the picture). Drifting snow fills the west side (left side of the picture) of the ridge. The main structure is 22 by 22 m and elevates 2–5 m above Utsteinen Ridge.

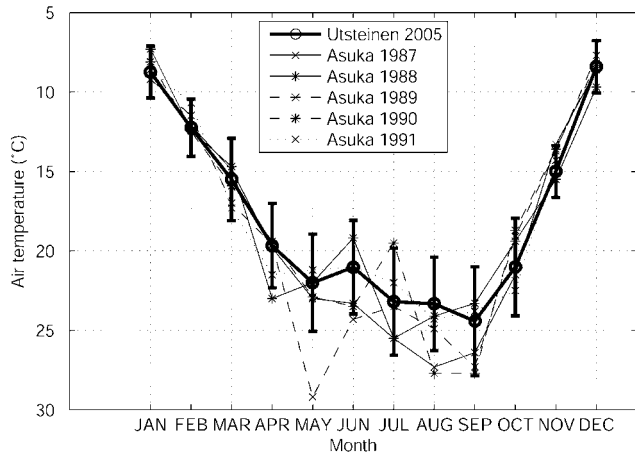


Fig. 4. The 2005 record of monthly mean air temperatures at Utsteinen compared to the temperatures recorded at Asuka station in the period 1987–91. Error bars show the standard deviation of daily average temperatures.

Sør Rondane Mountains. This granite rock culminates at an elevation of 1564 m a.s.l.

During two consecutive reconnaissance surveys in November 2004 and 2005, the initial glaciological and meteorological conditions of the vicinity of the station were investigated. We set up an automatic weather station, measured the ice thickness around the nunatak, and established a snow-stake network. In November 2008 the site was revisited and completely remeasured.

In this paper we report on the glaciological and meteorological results obtained from these three field seasons, which aims at defining the initial environmental conditions. We will show that this particular area i) experiences little effect of ice flow and ice flow change, due to the unique position of the Sør Rondane Mountains with respect to the overall dynamics of the Antarctic ice sheet, and ii) is very well sheltered from direct katabatic wind exposure.

Meteorological conditions

From December 2004 to February 2006, an Automatic Weather Station (Aanderaa AWS 2700) was operational on the ridge. It measured the 2 m air temperature (range: -60 to -30°C ; accuracy: 0.1°C), atmospheric pressure, wind speed and gust (range: 79 m s^{-1} ; accuracy: 0.2 m s^{-1}), and wind direction (threshold speed $< 0.3\text{ m s}^{-1}$; accuracy: $< 5^{\circ}$) at 10 min time intervals.

Figure 4 shows the monthly mean air temperatures compared to the measured temperatures at Asuka Station, recorded more than a decade earlier (JARE 1993). Although Utsteinen Ridge lies 466 m higher than Asuka, the 2005 air temperatures are in close agreement with the Asuka measurements. Moreover, during the winter months, Utsteinen temperatures are close to the warmest winter records of the former Japanese station. A reason may be the

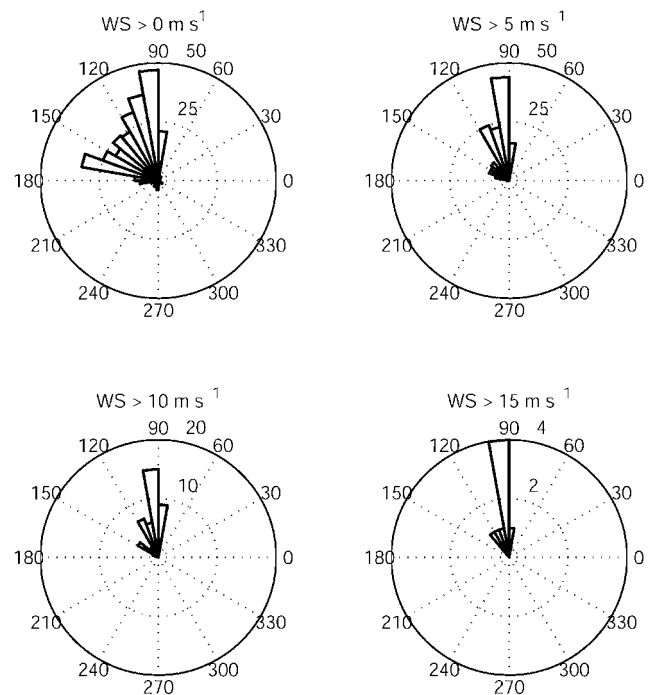


Fig. 5. Wind direction histograms for different wind speeds at Utsteinen, compiled from mean daily values (0° = north, 90° = east).

relatively low adiabatic gradient in the foothills of the mountains. Annual mean temperatures extracted from a regional climate model (van den Broeke 2008) along the 23°E meridian yield a temperature gradient of 4.5 K km^{-1} for elevations below 2000 m, while for elevations higher than 2300 m, this gradient is 17.1 K km^{-1} .

Although the Utsteinen temperature regime is relatively mild compared to the lower lying Asuka Station and to Roi Baudouin Station (-15°C , near sea level and 173 km further north), the yearly variation of the temperature curve exhibits the typical coreless winter of more continental stations (Thompson 1970, Connolley & Cattle 1994), i.e. a winter with no well defined minimum temperature. It is characterized by a rapid drop in temperature in autumn, a first minimum in May, a second (more important) minimum in August–September and a very steep rise toward the December–January maximum. The day-to-day variability in atmospheric temperature is much greater during winter than during summer as shown by the error bars in Fig. 4, again very similar to continental stations, such as South Pole (Town *et al.* 2008). The reason for both the coreless nature and higher temperature variability in winter is given by Town *et al.* (2008): i) winters in the southern hemisphere are stormier than summers, ii) the larger cyclonic activity results in more heat and moisture advection to the interior, iii) due to the lack of solar heating in winter, temperature inversions are more frequent under clear skies. Because these inversions are sensitive to

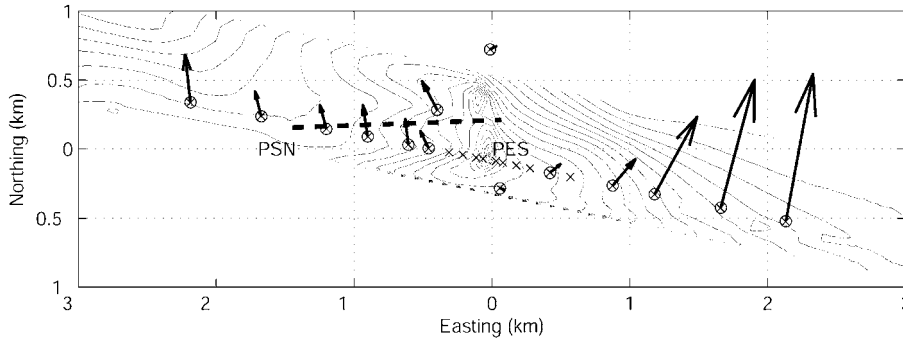


Fig. 6. Position and horizontal flow speed of the stake network near Utsteinen Ridge. Contours show the topography with an interval of 2.5 m. Maximum horizontal flow speed is 1.13 m a^{-1} . Stakes that are marked by a cross only (without circle), did not exist in 2008. The thick dashed line shows the position of the radar profile given in Fig. 8. PSN = Pink Shrimp Nunatak.

changes in wind speed, more short timescale fluctuation arise in winter than in summer. This larger variability biases the mean temperature during winter, hence the lack of a well-defined minimum temperature. While one year of measurements is not representative to define the climate of the Utsteinen area, comparison with long-term datasets of other stations in the Antarctic revealed that 2005 was a 'normal' year with respect to temperature and wind speed.

Utsteinen Ridge benefits from the protection of the mountains and is, due to its position at the western side of the range, less influenced by high katabatic wind speeds. Nevertheless, the site is not overprotected as it protrudes northwards from the northern rim of nunataks and therefore still benefits from a more constant wind flow. The mean wind speed recorded at Utsteinen is 6 m s^{-1} , which is half the mean wind speed recorded at Asuka Station. Mean summer wind speeds are around 4.5 m s^{-1} .

The primary wind direction at Utsteinen is from the east, a katabatic wind regime coming from Jenningsbreen, one of the major outlet glaciers cutting through the range. Somewhat less frequent are winds from the south-east, coming from Gunnestadbreen, the outlet glacier closest to the site. The whole sector E–SSE accounts for more than 90% of winds at Utsteinen (Fig. 5). Variable winds occur only at very low wind speeds, while higher wind speeds ($> 15 \text{ m s}^{-1}$) are dominantly from the E and ESE (Fig. 5). The near absence of a northerly component indicates little near-surface influence of cyclones or air masses associated with the low pressure trough bordering Antarctica.

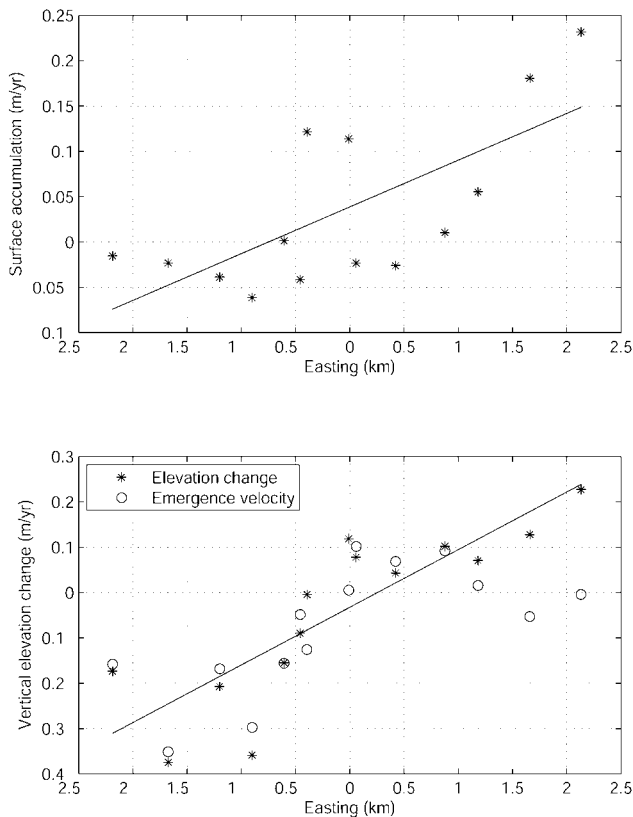


Fig. 7. Surface mass balance (snow depth) derived from stake length changes (upper panel) and vertical elevation change/emergence velocity (lower panel) for the stakes depicted in Fig. 6. The ridge is situated at the origin of the abscissa. Regression lines are shown to underline the general east–west tendency.

Mass balance and ice flow

In 2005 a series of stakes were set out perpendicular to Utsteinen Ridge extending more than 2 km to the east and west, respectively, hence aligned with the main wind direction (Fig. 6). Their position was precisely measured using a Leica System 1200 differential GPS (L1/L2). They were remeasured exactly three years later with a Leica SR20 differential GPS (L1 only). The same reference point was used on solid rock (Utsteinen Ridge) and baselines were less than 5 km. Horizontal position errors with the GPS system are of the order of 10–20 cm (measurement based on known geodetic points using the lowest accuracy system, SR20). The height of the stakes was also recorded. Local mass balance rates were inferred from the latter (Fig. 7). The reported values are not corrected for snow density, hence given in snow depth. They show accumulation to the east of the ridge and ablation to the west, at the downwind side of the ridge. This spatial pattern is also

confirmed from the GPS-measured elevation changes (see below).

The relatively low local mass balance in this area of the foothills of the Sør Rondane Mountains is not abnormal. Figure 2 displays the surface mass balance between 73°S and 70°S along the 23°E meridian, determined by regional atmospheric climate modelling (van de Berg *et al.* 2006). The coastal area - ice shelf and inland slope - is characterized by accumulation rates of $0.2\text{--}0.3\text{ m a}^{-1}$ w. eq. Values of around 0.2 m a^{-1} occur upstream from the mountain range, decreasing toward the interior ice sheet. The foothill area, just downstream of the Sør Rondane, is characterized by very low to negative surface accumulation rates, in agreement with our mass balance stake measurements. Ablation is a very common feature in this region, as witnessed by the occurrence of extensive blue ice fields. These bare ice areas occur where the accumulation is reduced due to wind scouring and reduced snowdrift at the lee sides of nunataks. Once they are established they survive by increased ablation, due to the low surface albedo, longwave radiation of the nearby rocks, high temperatures caused by adiabatic heating, and wind erosion (Pattyn & Declerq 1993). Some surficial lakes are observed on the outlet glaciers, reaching depths of 5–10 cm. Year-to-year variations in blue ice extension occur, but the main ice areas remain persistent features (Pattyn & Declerq 1993). Near Utsteinen, however, the whole area is covered by a substantial layer of snow, albeit that 3 km to the west of Utsteinen blue ice patches appear, hence confirming the ablation characteristics.

Horizontal velocity markers show a diverging pattern of ice flow around the ridge, characterized by very low velocities closest to the ridge, increasing both east- and westward. Highest velocities are encountered at the eastern side, as the ice flow in the west is buttressed by Pink Shrimp nunatak (unofficial name), a small nunatak 1.5 km to the west of Utsteinen Ridge. The maximum ice flow speed is 1.13 m a^{-1} , more than 2 km east from the ridge. Contrasting with the slow horizontal speeds, vertical elevation change on both sides of the ridge is quite substantial, leading to submergence velocities of the order of 0.2 to 0.3 m a^{-1} in the west (Fig. 7). This probably points to extensional flow as the ice passes through the corridor between Utsteinen Ridge and Pink Shrimp nunatak. To the east of the ridge emergence/submergence velocities are close to zero.

The low horizontal ice velocities in this area arise from the damming effect of the mountain range (Van Aulenboer & Declerq 1974, 1978). The total ice discharge, based on measurements of ice flux on each of the outlet glaciers that cut through the range, amounts to $1.76\text{ km}^3\text{ a}^{-1}$, which corresponds to a mean mass flux of $0.01\text{ km}^2\text{ a}^{-1}$, calculated over the 180 km long northern boundary of the mountains (Pattyn *et al.* 1992). This mass flux is especially low if we compare this value with the mean mass flux for the periphery of Antarctica. As noted by Van Aulenboer (1964) and Nishio *et al.* (1984), the reduced ice flow through the

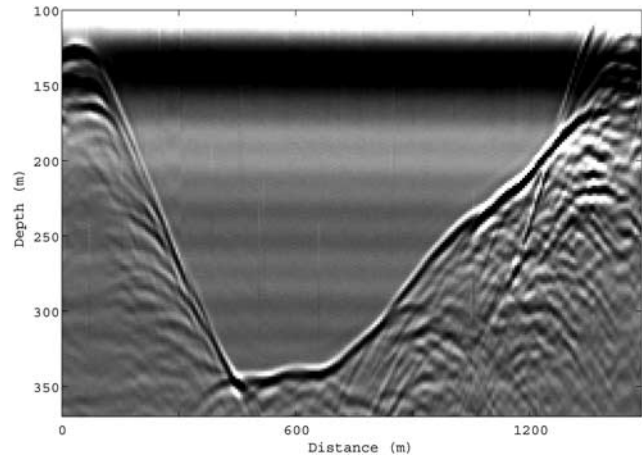


Fig. 8. Radargram showing the ice thickness variations. Depth is derived for the propagation speed of $179\text{ m }\mu\text{s}^{-1}$. The position of the profile is given in Fig. 6, starting near Pink Shrimp Nunatak (left) and running to Utsteinen Ridge.

mountains is probably the reason for the sheltered and crevasse-free inland ice slopes, northwards from the mountains to the coast. The mass flux of the ice shelf at the coast is much larger than the $0.01\text{ km}^2\text{ a}^{-1}$ and estimated at $0.06\text{ km}^2\text{ a}^{-1}$ for the length of the shelf (Pattyn *et al.* 1992). Therefore, the horizontal mass divergence of $0.05\text{ km}^2\text{ a}^{-1}$ should - in case of equilibrium - be balanced by both the accumulation between the mountains and the coast and the flow of glaciers around the mountain range. In view of the relative low accumulation rates (Fig. 2), the mass transport by the outlet glaciers surrounding the mountains should be quite substantial. Balance flux calculations confirm that the area is close to equilibrium conditions (Pattyn *et al.* 2005), but future measurements should narrow down the uncertainties, in view of the already observed mass changes of the glaciers diverting the mountain range.

Radar profiling

Preliminary radar profiles were obtained in 2005 using a 5 MHz (central frequency) ice penetrating radar (Narod & Clarke 1994), consisting of a monopulse transmitter generating 1600 V pulses across a resistively-loaded 10 m dipole antenna. These preliminary data gave a first idea of the ice thickness in the vicinity of Utsteinen Ridge (not shown). Subsequent radar profiling was made in 2008 with a 5 MHz impulse radar system (Matsuoka *et al.* 2007). The transmitter and receiver were put in line and separated by 45 m. Radio wave propagation speed is assumed $179\text{ m }\mu\text{s}^{-1}$ to account for the densification process (Herron & Langway 1980), and the associated uncertainty in bedrock elevation is $\sim 6\%$.

The radar profile (Fig. 8) starts at Pink Shrimp nunatak (see Fig. 6 for profile location). From here, the ice thickens

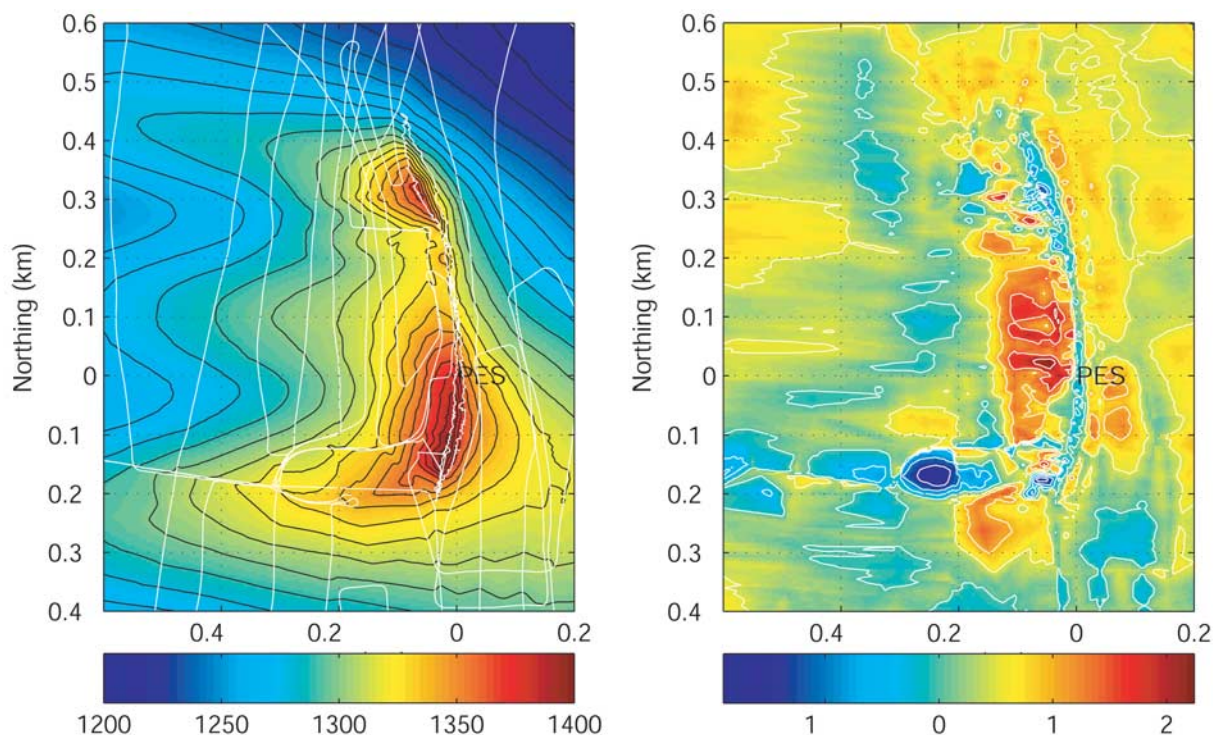


Fig. 9. Surface topography measured in 2008 of the Utsteinen Ridge and immediate surroundings. Contour interval is 2 m. Measurement tracks are displayed in white (left), Height difference (m) between 2008 and 2004 (right).

rapidly, reaching a depth of approximately 350 m, from where it rises again toward Utsteinen Ridge. This ice thickness is rather shallow compared to the ice thickness of the larger outlet glaciers that cut through the range. The major outlet glaciers are more than 1000 m thick and have a bedrock lying well below sea level (Van Autenboer & Declair 1978, Pattyn & Declair 1995), revealing a fjord-like subglacial landscape. These shallow depths in combination with low surface slopes limit the ice motion in the area around Utsteinen.

Snow surface elevation change

The expected lifetime of the Princess Elisabeth Station is estimated at 25 years, so accumulation of drifting snow around the construction should be limited. Several design characteristics were tested in a series of wind tunnel experiments during the development phase of the project (Sanz *et al.* unpublished). Prior to the construction of the station, a kinematic GPS survey was made using a Ski-Doo travelling at 10 km h^{-1} in order to measure the surface topography in the vicinity of Utsteinen Ridge. However, the error in such kinematic measurements is much higher than the one obtained from static GPS measurements. Using two consecutive measurements of the same profile, we calculated an RMS error of 15.23 cm. In 2008, the snow surface was remeasured to evaluate the impact of the

construction of the station on the (re)distribution of snow in its vicinity (Fig. 9). We are at present lacking precise measurements of wind speed during the 2008 winter season, but comparison with other stations reveals that 2008 was not an exceptional year.

The impact of the construction of the station on the surrounding snow surface is essentially concentrated near the station site itself, mainly due to the construction of the garage just below the ridge and the snow platform in front that elevates 2.5 m higher than before. Other changes are apparent in the southern sector of the ridge where the temporary camp is built every year. However, further downwind the station's effect is marginal and within the error of the measurements. It can thus be concluded that the new station has minimal influence on patterns of snowdrift, accumulation, and ablation.

Conclusions

Basic meteorological and glaciological parameters of the site of the Princess Elisabeth Station, Antarctica, were measured in 2004, 2005 (prior to the construction) and 2008 (after the construction). The site is well protected from katabatic winds coming down from the polar plateau, with the major wind component from east to south-east. The lack of northern winds points to the limited influence of coastal storms. The temperature record reveals the

coreless winter, typical for inland stations. Air temperatures are comparable with those measured at the former Japanese Asuka Station, although PES lies 466 m higher. Utsteinen Ridge is situated in a low mass balance area (ablation island), characterized by a slight positive mass balance to the east (windward side) and a slight negative balance to the west of the ridge. Due to the small ice thickness and surface slopes, ice motion around the station is low, with maximum values $\sim 1 \text{ m a}^{-1}$ 2 km to the east, and diverting around the ridge. Finally, a comparison of the snow surface topography before and after the construction of the station reveals that only the immediate site is influenced due to construction works, but that further away from the ridge the drifting snow pattern is hardly influenced.

Acknowledgements

This paper forms a contribution to the Belgian Research Programme on the Antarctic (Belgian Federal Science Policy Office), Project no. EA/11/3A 'Belgian Ice Sheet - Shelf Ice Measurements in Antarctica (BELISSIMA)'. K.M. was partly supported by a University of Washington Royalty Research Fund (project #4208). The authors are indebted to Alain Hubert, Nathalie Pattyn and Maike Vancauwenberghe for their valuable assistance with field measurements. The authors wish to thank Christina Hulbe and an anonymous referee for their remarks that considerably improved the manuscript.

References

- BAMBER, J.L., GOMEZ-DANS, J.L. & GRIGGS, J.A. 2009. A new 1 km digital elevation model of the Antarctic derived from combined satellite radar and laser data - Part 1: data and methods. *The Cryosphere*, **3**, 101–111.
- CONNOLLEY, W.M. & CATTLE, H. 1994. The Antarctic climate of the UKMO Unified Model. *Antarctic Science*, **6**, 115–122.
- FUJII, Y. 1981. Aerophotographic interpretation of surface features and estimation of ice discharge at the outlet of the Shirase drainage basin, Antarctica. *Nankyoku Shiryo*, **72**, 1–15.
- HERRON, M.M. & LANGWAY, C.C. 1980. Firn densification: an empirical model. *Journal of Glaciology*, **25**, 373–385.
- JARE. 1993. Meteorological data at Asuka Station, Antarctica in 1991. *JARE Data Reports*, **190**.
- LYTHE, M.B. & VAUGHAN, D.G. 2001. BEDMAP: a new ice thickness and subglacial topographic model of Antarctica. *Journal of Geophysical Research*, **106**, 11 335–11 351.
- MATSUOKA, K., THORSTEINSSON, T., BJORNSSON, H. & WADDINGTON, E.D. 2007. Anisotropic radio-wave scattering from glacial water regimes, Myrdalsjokull. *Journal of Glaciology*, **53**, 473–478.
- MERCER, J. 1978. West Antarctic Ice Sheet and CO₂ greenhouse effect: a threat of disaster. *Nature*, **271**, 321–325.
- NAROD, B.B. & CLARKE, G.K.C. 1994. Miniature high-power impulse transmitter for radio-echo sounding. *Journal of Glaciology*, **40**, 190–194.
- NARUSE, R. 1979. Thinning of the ice sheet in Mizuho Plateau, East Antarctica. *Journal of Glaciology*, **24**, 45–52.
- NISHIO, F., ISHIKAWA, M., OHMAE, H., TAKAHASHI, S. & KATSUSHIMA, T. 1984. A preliminary study of glacial geomorphology in area between Breid Bay and the Sør Rondane Mountains in Queen Maud Land, East Antarctica. *Nankyoku Shiryo*, **83**, 11–28.
- NISHIO, F., MAE, S., OHMAE, H., TAKAHASHI, S., NAKAWO, M. & KAWADA, K. 1989. Dynamical behavior of the ice sheet in Mizuho Plateau, East Antarctica. *Proceedings of the NIPR Symposium on Polar Meteorology & Glaciology*, **2**, 97–104.
- PATTYN, F. & DECLEIR, H. 1993. Satellite monitoring of ice and snow in the Sør Rondane Mountains, Antarctica. *Annals of Glaciology*, **17**, 41–48.
- PATTYN, F. & DECLEIR, H. 1995. Subglacial topography in the central Sør Rondane Mountains, East Antarctica: configuration and morphometric analysis of valley cross profiles. *Nankyoku Shiryo*, **39**, 1–24.
- PATTYN, F. & NARUSE, R. 2003. The nature of complex ice flow in Shirase Glacier catchment, East Antarctica. *Journal of Glaciology*, **49**, 429–436.
- PATTYN, F., DE BRABANDER, S. & HUYGHE, A. 2005. Basal and thermal control mechanisms of the Ragnhild Glaciers, East Antarctica. *Annals of Glaciology*, **40**, 225–231.
- PATTYN, F., DECLEIR, H. & HUYBRECHTS, P. 1992. Glaciation of the central part of the Sør Rondane, Antarctica: glaciological evidence. In YOSHIDA, Y., KAMINUMA, K. & SHIRAIISHI, K., eds. *Recent progress in Antarctic earth science*. Tokyo: Terra Scientific Publishing Company, 669–678.
- RIGNOT, E. & JACOBS, S.S. 2002. Rapid bottom melting widespread near Antarctic ice sheet grounding lines. *Science*, **296**, 2020–2023.
- RIGNOT, E.J., BAMBER, J.L., VAN DEN BROEKE, M.R., DAVIS, C., LI, Y., VAN DE BERG, W.J. & VAN MELGAARD, E. 2008. Recent Antarctic ice mass loss from radar interferometry and regional climate modelling. *Nature Geoscience*, **1**, 106–110.
- RIPPIN, D.M., BAMBER, J.L., SIEGERT, M.J., VAUGHAN, D.G. & CORR, H.F.J. 2003. Basal topography and ice flow in the Bailey/Slessor region of East Antarctica. *Journal of Geophysical Research*, **108**, 10.1029/2003JF000039.
- SCHOOF, C. 2007. Ice sheet grounding line dynamics: steady states, stability and hysteresis. *Journal of Geophysical Research*, **112**, 10.1029/2006JF000664.
- THOMPSON, D.C. 1970. The coreless winter at Scott Base, Antarctica. *Quarterly Journal of the Royal Meteorological Society*, **96**, 556–557.
- TOH, H. & SHIBUYA, K. 1992. Thinning rate of ice sheet on Mizuho Plateau, East Antarctica, determined by GPS differential positioning. In YOSHIDA, Y., KAMINUMA, K. & SHIRAIISHI, K., eds. *Recent progress in Antarctic earth science*. Tokyo: Terra Scientific Publishing Company, 579–583.
- TOWN, M.S., WADDINGTON, E.D., VON WALDEN, P. & WARREN, S.G. 2008. Temperatures, heating rates and vapour pressures in near-surface snow at the South Pole. *Journal of Glaciology*, **54**, 487–498.
- VAN AUTENBOER, T. 1964. The geomorphology and glacial geology of the Sør Rondane, Dronning Maud Land. In ADIE, R., ed. *Antarctic geology*. Amsterdam: North Holland, 81–103.
- VAN AUTENBOER, T. & DECLEIR, H. 1974. Mass transport measurements in the Sør Rondane, Dronning Maud Land, Antarctica. *Service Geologique de Belgique, Professional Paper*, No. 6, 1–25.
- VAN AUTENBOER, T. & DECLEIR, H. 1978. Glacier discharge in the Sør Rondane, a contribution to the mass balance of Dronning Maud Land, Antarctica. *Zeitschrift für Gletscherkunde und Glazialgeologie*, **14**, 1–16.
- VAN DE BERG, W.J., VAN DEN BROEKE, M.R., REIJMER, C.H. & VAN MELGAARD, E. 2006. Reassessment of the Antarctic surface mass balance using calibrated output of a regional atmospheric climate model. *Journal of Geophysical Research*, **111**, 10.1029/2005JD006495.
- VAN DEN BROEKE, M.R. 2008. Depth and density of the Antarctic firn layer. *Arctic, Antarctic, and Alpine Research*, **40**, 432–438.
- WEERTMAN, J. 1974. Stability of the junction of an ice sheet and an ice shelf. *Journal of Glaciology*, **13**, 3–11.
- WINGHAM, D., SHEPHERD, A., MUIR, A. & MARSHALL, G. 2006. Mass balance of the Antarctic ice sheet. *Philosophical Transactions of the Royal Society*, **A364**, 1627–1635.

Melting and refreezing beneath Roi Baudouin Ice Shelf (East Antarctica) inferred from radar, GPS, and ice core data

F. Pattyn,¹ K. Matsuoka,² D. Callens,¹ H. Conway,³ M. Depoorter,¹ D. Docquier,¹ B. Hubbard,⁴ D. Samyn,^{1,5} and J. L. Tison¹

Received 14 July 2011; revised 2 September 2012; accepted 5 September 2012; published 11 October 2012.

[1] Ice-penetrating radar profiles across the grounding line of a small ice-rise promontory located within the Roi Baudouin Ice Shelf in the Dronning Maud Land sector of East Antarctica show downward dipping englacial radar-detected reflectors. Model results indicate that this reflector pattern is best fit by including basal melting of at least 15 cm a^{-1} . This rate of melting is low compared with rates observed on larger ice shelves in both West and East Antarctica. Ice cores extracted from a rift system close to the ice-rise promontory show several meters of marine ice accreted beneath the shelf. These observations of low rates of basal melting, and limited distribution of accreted marine ice suggest that either Antarctic surface water may reach the ice shelf base or that circulation beneath the shelf is likely dominated by the production of high salinity shelf water rather than the incursion of circumpolar deep water, implying a weak sub-shelf circulation system here. Many of the ice shelves located along the coast of Dronning Maud Land are, like Roi Baudouin Ice Shelf, characterized by frequent ice rises and promontories. Therefore, it is highly likely that these are also of shallow bathymetry and are subject to similarly weak side-shelf basal melting and refreezing.

Citation: Pattyn, F., K. Matsuoka, D. Callens, H. Conway, M. Depoorter, D. Docquier, B. Hubbard, D. Samyn, and J. L. Tison (2012), Melting and refreezing beneath Roi Baudouin Ice Shelf (East Antarctica) inferred from radar, GPS, and ice core data, *J. Geophys. Res.*, 117, F04008, doi:10.1029/2011JF002154.

1. Introduction

[2] Marine ice sheets that terminate in the ocean are particularly sensitive to perturbations at the grounding line [Weertman, 1974; Dupont and Alley, 2005; Pattyn *et al.*, 2006; Schoof, 2007; Gagliardini *et al.*, 2010]. Sub-shelf melting occurs near the grounding lines of many of the major outlet glaciers throughout Antarctica [Rignot and Jacobs, 2002; Pritchard *et al.*, 2012]. High melt rates underneath ice shelves have been measured in both West Antarctica [Payne *et al.*, 2007; Thoma *et al.*, 2008; Jenkins *et al.*, 2010], and East Antarctica [Smedsrud *et al.*, 2006; Nicholls *et al.*,

2006, 2008]. Observations of synchronous rapid thinning of the floating termini of several glaciers in a region are generally taken to be an indication that the changes are being forced by the ocean [Shepherd *et al.*, 2004; Thoma *et al.*, 2008]. Such forcing leads to increased discharge of inland ice across the grounding line [Schoof, 2007; Rignot *et al.*, 2008; Pritchard *et al.*, 2012]. Sub-shelf melting near grounding lines is linked to patterns of large-scale water circulation [Lewis and Perkins, 1986; Jacobs *et al.*, 1992; Holland, 2008]. Sub-shelf melt rates are relatively high when circumpolar deep water (CDW) reaches the continental shelf, and generally lower when sea ice formation results in high salinity shelf water (HSSW). Melting and freezing along the shelf interface are part of the “ice pump” that is controlled in part by the intensity of HSSW circulation [Lewis and Perkins, 1986].

[3] However, the most common water mass over the narrow continental shelves of East Antarctica is the Antarctic Surface Water (ASW) [Whitworth *et al.*, 1998]. At the coast this surface layer deepens as a result of downwelling forced by the easterly winds blowing along the coast. Where the ice sheet topography is steep and the continental shelf narrow (i.e. around East Antarctica) the downwelling is so effective that the whole of the water column over the continental shelf is comprised of ASW [Nøst *et al.*, 2011]. Similar to HSSW,

¹Laboratoire de Glaciologie, Université Libre de Bruxelles, Brussels, Belgium.

²Norwegian Polar Institute, Tromsø, Norway.

³Department of Earth and Space Sciences, University of Washington, Seattle, USA.

⁴Centre for Glaciology, Institute of Geography & Earth Sciences, Aberystwyth University, Ceredigion, UK.

⁵Glaciology Research Group, University of Uppsala, Uppsala, Sweden.

Corresponding author: F. Pattyn, Laboratoire de Glaciologie, Université Libre de Bruxelles, Av. F.D. Roosevelt 50, B-1050 Brussels, Belgium. (fpattyn@ulb.ac.be)

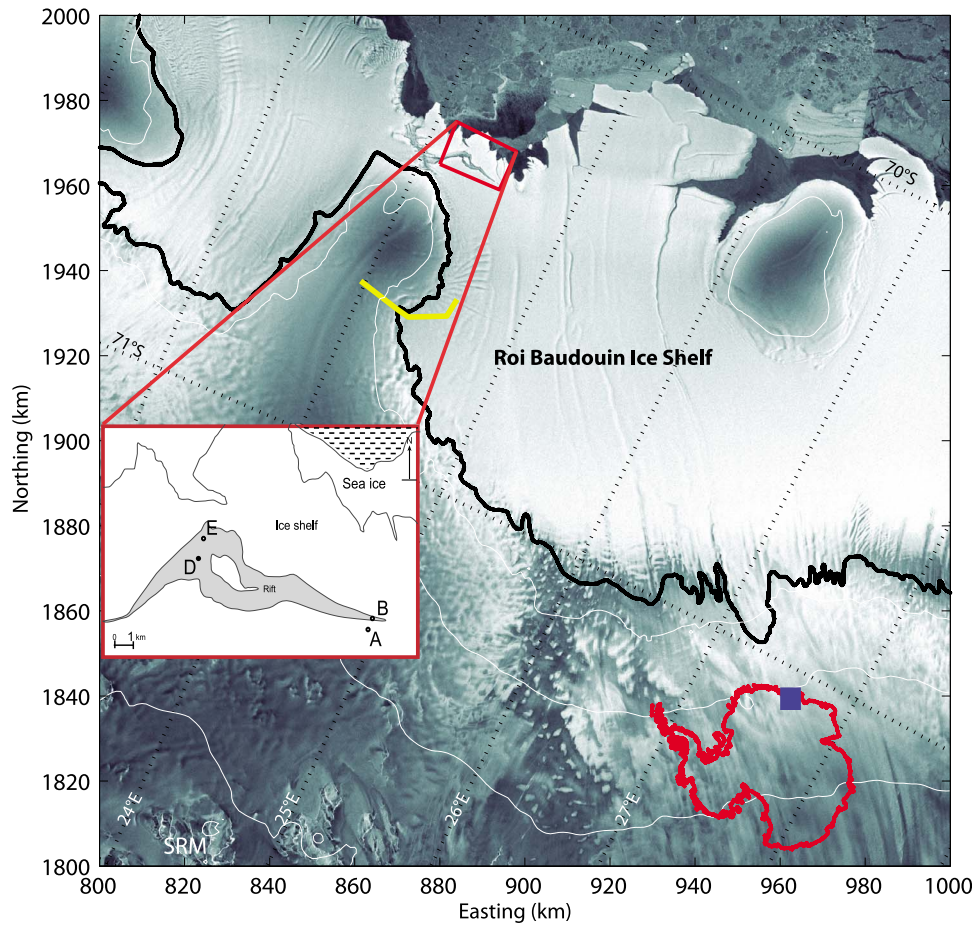


Figure 1. Location of the ice-rise promontory and the Roi Baudouin Ice Shelf (RBIS), Dronning Maud Land, East Antarctica. Contour lines are in white (contour interval is 300 m, starting at 200 m a.s.l.) [Bamber *et al.*, 2009]. The grounding line is given in black [Bindshadler *et al.*, 2011]. The yellow line is the radar traverse. Location of the boreholes in the rift are shown in the inset figure. RAMP (Radarsat) is used as a background image. SRM = Sør Rondane Mountains.

this cold ASW can also melt the ice shelf base [Hattermann *et al.*, 2012], producing Ice Shelf Water (ISW). This ISW, derived from melting meteoric ice and mixing with HSSW/ASW, is also an important component of the ocean circulation. It is known that ISW production varies for different ice shelves but relative contributions from HSSW and CDW are not known for much of East Antarctica.

[4] Most of the evidence for ice-ocean interactions comes from the large Antarctic ice shelves or from ice shelves of the West Antarctic Ice Sheet, but apart from studies on Fimbul ice shelf [Nicholls *et al.*, 2006, 2008; Hattermann *et al.*, 2012], little is known about the ice shelves in the Dronning Maud Land (DML) sector of East Antarctica, although most of the DML coast is characterized by marine-terminating glaciers in ice shelves.

[5] Herein, we combine several empirical lines of evidence to investigate the nature of sub-shelf circulation beneath an ice shelf on the Princess Ragnhild Coast, i.e., Roi Baudouin Ice Shelf (RBIS), DML, East Antarctica. We use ice-penetrating radar, GPS measurements and ice core drilling to investigate ice-ocean interactions on RBIS. Comparison of

observed radar-detected englacial reflectors with results from an ice flow model is used to infer basal melting across the grounding line. Direct evidence of sub-shelf marine ice accretion comes from four ice cores drilled through the shelf.

2. Study Area

[6] During the Austral summer 2008–09, we conducted field work in the vicinity of a small ice-rise promontory in RBIS, East Antarctica. Surface topography shows that the ice-rise promontory has a local flow pattern (Figure 1). Downstream of the promontory, a large rift system ~ 5 km from the ice shelf edge has a maximum width of 2 km and is filled with well consolidated “ice mélange”. The bathymetry beneath the ice shelf is relatively shallow; it is 200–300 m b.s.l. near the shelf front [Nishio *et al.*, 1984], and it approaches 500 m b.s.l. near the grounding line [Nishio *et al.*, 1984; Timmermann *et al.*, 2010]. In view of our measured ice thickness, water column thickness beneath the shelf varies between 0 and 200 m. The ice velocity in this area is several tens of meters per year, but reaches values up to 350 m a^{-1} in the central part

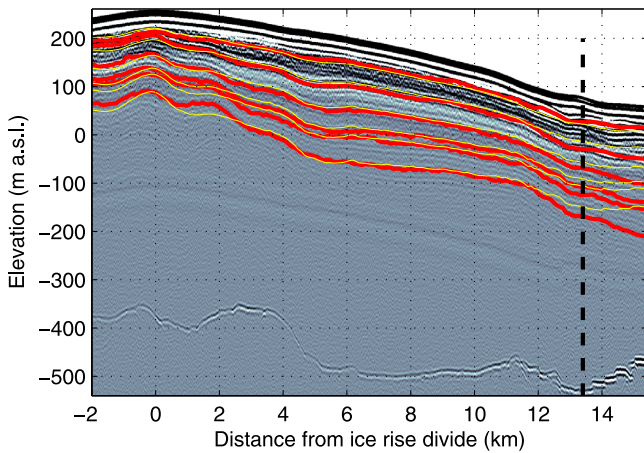


Figure 2. Section of radar profile (location shown in Figure 1) across the ice-rise promontory and the grounding line (vertical dashed line). Comparison of radar-detected reflectors (red), and modeled isochrones (yellow) for the standard experiment (no basal melting) shows large mismatch at the grounding line and within the ice shelf; the mismatches for different model runs are shown in Figure 3.

of RBIS, further to the east of our study area [Rignot *et al.*, 2011].

3. Field Measurements

3.1. Ice-Penetrating Radar and GPS Profiling

[7] We collected ice-penetrating radar profiles across the ice-rise promontory and the ice shelf (Figure 1), using a 5-MHz impulse radar system [Matsuoka *et al.*, 2012]. The transmitter and receiver were separated by 45 m and towed in line. Each record consists of several hundred stacked (averaged) waveforms to improve the signal-to-noise ratio. Additional processing includes bandpass filtering, corrections for surface topography and conversion of two way travel time to depth. We assume the wave speed in ice is $169 \text{ m } \mu\text{s}^{-1}$. Uncertainty in thickness comes from uncertainty in the wave speed (about $2 \text{ m } \mu\text{s}^{-1}$) and from picking the two-way travel time from the surface to the bed. The former corresponds to 1.2% of the ice thickness and the latter is about $0.1 \text{ } \mu\text{s}$ for 5 MHz, which corresponds to $\sim 8.5 \text{ m}$. Assuming the errors are uncorrelated, total uncertainty on the ice-rise promontory ($<600 \text{ m}$ thick) is up to $\sim 11 \text{ m}$. On the ice shelf ($\sim 250 \text{ m}$ thick), total uncertainty is $\sim 9 \text{ m}$.

[8] Radar profiles show both reflections from the bed and englacial reflectors. Ice thickness is $\sim 600 \text{ m}$ between the crest of the ice-rise promontory and the grounding line (Figure 2). Downstream from the grounding line on the ice shelf, ice thickness decreases rapidly to $\sim 250 \text{ m}$. At some locations on the shelf, clutter from multiple hyperbolic echoes beneath surface rumples hampered detection of the basal interface. In previous work we found an abrupt increase in basal reflectivity (near km 13), which is within a kilometer of where the shelf is freely floating [Matsuoka *et al.*, 2012]. The magnitude of this reflectivity change is consistent with a change from a grounded (possibly wet) environment to an ice-ocean interface [Matsuoka *et al.*, 2012].

[9] Profiles were positioned using a roving Leica SR20 differential GPS (L1) referenced to a base station located on the grounded ice-rise promontory. The absolute position of the base station on the ice-rise promontory was obtained from Precise Point Processing, and further adjusted to the EGM96 geoid model to obtain a position relative to mean sea level. The EGM96 model has a discrepancy of 0.27 m compared to measured geoid heights in Breid Bay, near our field site [Shibuya *et al.*, 1999]. A tide model [Padman *et al.*, 2002] was employed to further correct elevations of the roving station on the ice shelf. The tide model predicts tidal amplitudes of less than 1.6 m , with changes of less than 0.4 m predicted over the 5-hour period of our radar and GPS measurements across the ice shelf. Horizontal and vertical position errors for the roving GPS are of the order of $0.1\text{--}0.2 \text{ m}$ [Pattyn *et al.*, 2010]. For subsequent analyses, we prescribed the grounding line to be the position where the ice becomes freely floating.

3.2. Ice Core Drilling

[10] To determine the presence of marine ice, four ice cores between 10 and 38 m long were drilled north of the ice-rise promontory using either an Eclipse or a SIPRE-based electro-mechanical drill (The Eclipse drill allows drilling down to several hundred meters, while the SIPRE-type drill is more portable and specially equipped for drilling into water saturated permeable ice, such as ice shelf ice and rift ice would be. Both were used in the field.) (Figure 1): (i) on the ice shelf (core A); (ii) on the slope entering the apex of the rift (core B); (iii) within the rift system (cores D and E). An optical televiewer [Hubbard *et al.*, 2008, 2012] was deployed in each of the boreholes. Core samples were generally analyzed at $0.5\text{--}1.0 \text{ m}$ depth intervals for their isotopic composition ($\delta^{18}\text{O}$, δD), bulk density, salinity and ice texture. Bulk salinity was measured according to standard procedure [Khazendar *et al.*, 2001], with precision of $\pm 0.05 \text{ psu}$. Bulk density was measured with the mass/volume technique (± 0.05 precision). Isotopic measurements were made using a Thermo-Finnigan Mass Spectrometer Delta Advantage ($\delta^{18}\text{O} \pm 0.05\text{‰}$, $\delta\text{D} \pm 1.00\text{‰}$). On core A, samples of isotopes and density of the meteoric ice collected at 100 mm resolution (not shown) reveal a clear seasonal signal. The accumulation rate (0.27 m a^{-1} w.e.) derived from the measurements is in accordance with regional mass balance modeling results [van de Berg *et al.*, 2006].

4. Ice-Flow Modeling

4.1. Model Setup

[11] Englacial reflectors detected with 5-MHz radar are principally caused by changes in ice density and acidity [Fujita *et al.*, 1999], and they are generally considered to be isochrones. In this section we generate isochrones using a numerical ice flow model and conduct experiments with different boundary conditions to determine the range of conditions that minimize the mismatch between the spatial pattern of modeled and measured reflectors.

[12] In regions where radar-detected reflectors are at shallow depths (and given the low ice flow velocities of the grounded ice sheet) the recent spatial pattern of accumulation can be inferred using the local-layer approximation [Haefeli, 1963; Waddington *et al.*, 2007]. We scale the local

accumulation pattern across the ice-rise promontory using the regional value of 0.27 m a^{-1} w.e. [van de Berg *et al.*, 2006].

[13] We use an isothermal higher-order, steady state ice sheet model [Pattyn, 2002a, 2010], constrained by the local surface mass balance obtained from the local-layer approximation, to reconstruct the age distribution across the ice-rise promontory and shelf. In a Cartesian coordinate system, the horizontal velocity field along a flowline and under plane strain conditions is [Pattyn, 2002a]:

$$4 \frac{\partial}{\partial x} \left(\eta \frac{\partial u}{\partial x} \right) + \frac{\partial}{\partial z} \left(\eta \frac{\partial u}{\partial z} \right) = \rho g \frac{\partial(b+H)}{\partial x}, \quad (1)$$

where u is the horizontal velocity along the flowline, b and H the bottom of the ice and the ice thickness, respectively, and where the effective viscosity η is defined by

$$\eta = \frac{1}{2} A^{-1/n} \left[\left(\frac{\partial u}{\partial x} \right)^2 + \frac{1}{4} \left(\frac{\partial u}{\partial z} \right)^2 \right]^{(1-n)/2n}. \quad (2)$$

Here, A and n are the flow parameter and the exponent in Glen's flow law, respectively ($A = 10^{-17} \text{ Pa}^{-n} \text{ a}^{-1}$; $n = 3$). The value of A corresponds to ice with a mean temperature of -10°C , which is consistent with the balance velocities imposed at the boundaries of the domain (see below). At this point, thermomechanical coupling is not considered; the effect of including this coupling on the modeled spatial pattern of isochrones would influence the absolute age of the lower layers, where the highest temperature gradients occur. However, since detected reflectors are restricted to the upper half of the ice column, this effect is therefore limited.

[14] For modeling purposes it is convenient to scale the velocity field in the vertical dimension to the ice thickness. Defining $\zeta = (b + H - z) / H$, the surface transforms to $\zeta = 0$, while the bottom of the ice mass becomes $\zeta = 1$. The horizontal flow field (1) is therefore rewritten as [Pattyn, 2003]:

$$4 \frac{\partial}{\partial x} \left(\eta \frac{\partial u}{\partial x} + a_x \eta \frac{\partial u}{\partial \zeta} \right) + 4 a_x \frac{\partial}{\partial \zeta} \left(\eta \frac{\partial u}{\partial x} + a_x \eta \frac{\partial u}{\partial \zeta} \right) + \frac{1}{H^2} \frac{\partial}{\partial \zeta} \left(\eta \frac{\partial u}{\partial \zeta} \right) = \rho g \frac{\partial(b+H)}{\partial x}, \quad (3)$$

where

$$a_x = \frac{1}{H} \left(\frac{\partial b}{\partial x} + (1 - \zeta) \frac{\partial H}{\partial x} \right), \quad (4)$$

while (2) transforms to

$$\eta = \frac{1}{2} A^{-1/n} \left[\left(\frac{\partial u}{\partial x} + a_x \frac{\partial u}{\partial \zeta} \right)^2 + \frac{1}{4 H^2} \left(\frac{\partial u}{\partial \zeta} \right)^2 \right]^{(1-n)/2n}. \quad (5)$$

Boundary conditions for the model are obtained from balance velocities derived by integrating the surface mass balance from the ice divide to the end of the surveyed profile. The velocity at the model domain boundary is then fixed to the balance velocity. Basal velocities are kept zero at the base, except in the ice shelf, where basal friction is set to zero so that velocities at the base equal those at the surface [Pattyn, 2003].

[15] The vertical velocity field is derived from mass conservation combined with the incompressibility condition for ice. Given an ice sheet in steady state, a simple analytical expression can be obtained, based on the horizontal velocity field [Hindmarsh, 1999], i.e.

$$w(x, \zeta) = - \left[\frac{\zeta^{n+2} - 1 + (n+2)(1-\zeta)}{n+1} \right] \dot{a} - \dot{m} + u \nabla b + (1-\zeta) u \nabla H, \quad (6)$$

where w is the vertical velocity, \dot{a} is the local accumulation rate, and \dot{m} is the basal melting rate. For plug flow (ice shelf), (6) reduces to $w(x, \zeta) = (\zeta - 1) \dot{a} - \zeta \dot{m}$ [Hindmarsh, 1999].

[16] The age calculation within the ice sheet is written as an advection equation with a small diffusion term added in order to stabilize the numerical solution [Huybrechts, 1994; Greve, 1997; Pattyn, 2002b]:

$$\frac{\partial \mathcal{A}}{\partial t} = 1 - u \frac{\partial \mathcal{A}}{\partial x} - w \frac{\partial \mathcal{A}}{\partial z} + D_a \frac{\partial^2 \mathcal{A}}{\partial z^2} \quad (7)$$

where \mathcal{A} is the ice age (a), and D_a a diffusion coefficient ($5 \times 10^{-8} \text{ m}^2 \text{ a}^{-1}$) [Mügge *et al.*, 1999]. Written in the scaled coordinate system, (7) becomes

$$\frac{\partial \mathcal{A}}{\partial t} = 1 - u \frac{\partial \mathcal{A}}{\partial x} + \left(\frac{w}{H} - a_x \right) \frac{\partial \mathcal{A}}{\partial \zeta} + \frac{D_a}{H^2} \frac{\partial^2 \mathcal{A}}{\partial \zeta^2}. \quad (8)$$

Boundary conditions to this equation are $\mathcal{A}(0) = 0$ at the surface and the age of the integration time at the bottom of the ice mass (typically 10 ka). The choice of this value has no effect on the age of the identified isochrones. The model is solved numerically on a finite difference grid, equally spaced in x and unequally spaced in ζ , providing a higher resolution approaching the base of the ice mass [Pattyn, 2002a].

4.2. Replicating Englacial Radar Reflectors

[17] Based on the inferred accumulation pattern from the shallow radar reflectors, each observed isochrone was dated using a minimization procedure by reducing the mismatch between observed and modeled isochrone depth, leading to ages ranging from 175 to 957 a BP for the uppermost and lowermost isochrones, respectively. This procedure consists of calculating the misfit between an observed isochrone and a series of modeled isochrones of different age. The smallest misfit then corresponds to the age of the observed isochrone. In general, the model produces a good fit between observed and calculated isochrone depths for the grounded ice sheet profile, except for the area around the grounding line where radar-detected reflectors dip downward (Figure 2).

4.3. Causes of Downwarped Reflectors Near the Grounding Line

[18] This anomaly could be caused by several processes, including subglacial melting at the grounding line or a local increase in surface accumulation, both of which could cause downward motion of the reflectors. Other possible processes could be related to temporal variability in surface accumulation (unlikely since the grounded part would be equally affected by this effect), or to the convergent flow as the

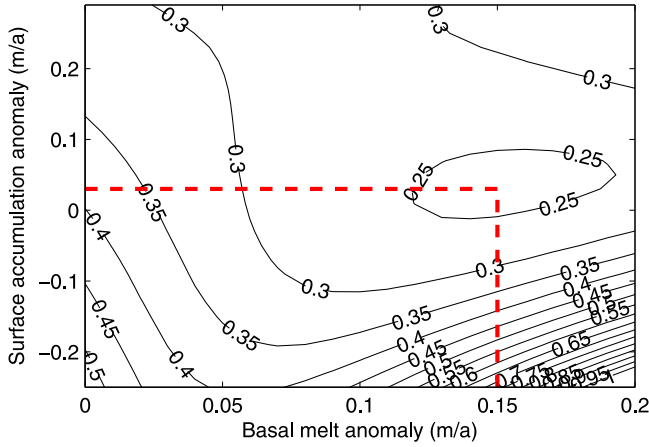


Figure 3. Minimization of the RMS error (m) between observed and modeled isochrones for different combinations of accumulation/ablation and basal melting near the grounding line. The best fit is obtained with basal melting of 15 cm a^{-1} and no accumulation anomaly.

flowline turns into the main ice shelf (three-dimensional effects, Figure 1). These are discussed below.

[19] In order to examine possible effects from sub-shelf melting and surface accumulation, we follow the approach of others [e.g., Catania et al., 2006, 2010] and conduct a series of sensitivity experiments using the ice-flow model. We forced the model with anomalies in surface accumulation/ablation (ranging from -0.25 to 0.25 m a^{-1}) and basal melting (0 to 0.25 m a^{-1}) for the ice shelf (between the grounding line and a distance of 2 km downstream) and calculated the RMS error between observed and calculated isochrone depths (Figure 3). For each experiment shown, we assume that the basal melting and accumulation anomalies are constant through time and spatially distributed over a zone of 2 km . The best fit to the data is obtained with no surface accumulation anomaly and basal melting of 0.15 m a^{-1} (Figure 3). Reasonable fits can be obtained with small surface anomalies and slightly lower or higher values of basal melting (0.1 to 0.2 m a^{-1}), but all results indicate that basal melting is required.

[20] The experiments above consider a continuously applied anomaly over a sustained period of time. We therefore tested applying anomalies over shorter time spans as well, but all led to worse misfits. Due to horizontal ice flow, any anomaly is advected downstream, hence the upwarping of the deeper layers at and downstream from the grounding line disappears when the anomaly is applied for any given period in the past.

[21] Conditions of plane strain are valid for the grounded ice flow in the saddle area of the ice-rise promontory (where flowlines are strictly parallel to each other), but do not apply in the ice shelf because of the turning of ice flow (indicated by the flow stripes evident on the ice shelf, Figure 1). In this area, ice flows convergently. Since mass conservation implies that $\nabla \cdot \mathbf{v} = 0$, we obtain for a flowline [Reeh, 1988; Pattyn, 2002a]:

$$\frac{\partial w}{\partial \zeta} = H \left(\frac{\partial u}{\partial x} + a_x \frac{\partial u}{\partial \zeta} \right) + H \dot{\epsilon}_{yy}, \quad (9)$$

where $\dot{\epsilon}_{yy} = \partial v / \partial y$ is the transverse strain rate and v the velocity in the y direction. Plug flow of the ice shelf implies

that $\partial w / \partial \zeta = \dot{a} - \dot{m}$ and that $\partial u / \partial \zeta = 0$. Under simplified conditions of plane strain, $\dot{\epsilon}_{yy} = 0$, it is therefore safe to say that

$$H \frac{\partial u}{\partial x} = \dot{a} - \dot{m}. \quad (10)$$

However, for convergent flow, $\dot{\epsilon}_{yy} < 0$, so the vertical velocity gradient $\partial w / \partial \zeta$ is reduced. Since $\partial w / \partial \zeta - \dot{a} = -\dot{m}$, this implies a higher basal melt rate to match the downwarping pattern than that calculated above. Conversely, divergent flow would have the opposite effect (i.e., less basal melt needed to explain the pattern). Although it is difficult to estimate the amount of buttressing due to the convergent flow, we can consider the calculated basal melt anomaly of 0.15 m a^{-1} is a lower bound and actual melt rates are likely higher.

5. Sub-shelf Accretion of Marine Ice

[22] Sub-shelf melting at the grounding line can result in accretion of marine ice beneath the shelf caused by consolidation of frazil ice that originates in supercooled water. $\delta^{18}\text{O}$ values for marine ice are close to $+2\%$, proving that it originated from freezing seawater [Gow and Epstein, 1972; Morgan, 1972; Oerter et al., 1992]. Bulk salinity of consolidated marine ice at depth varies between 0.03 and 0.3 psu , which is two or three orders of magnitude higher than meteoric ice and one or two orders of magnitude lower than sea ice [Souchez et al., 1991; Tison et al., 1993; Khazendar et al., 2001; Tison and Khazendar, 2001].

[23] In principle, the thickness of a marine ice layer beneath an ice shelf that is in hydrostatic equilibrium could be determined by comparing the measured surface elevation of the floating shelf with the surface elevation calculated from buoyancy [Corr et al., 1995; Fricker et al., 2001]. In practice, the calculation is hampered by large uncertainty in the density profile through the shelf, and uncertainties and ambiguities in the radar-detected ice thickness (Section 3.1). Our measurements of temperature, bulk salinity, ice texture, and stable isotopes from the ice cores (Figure 4) offer another way to investigate marine ice accretion.

[24] Firn and meteoric ice in the region have negative $\delta^{18}\text{O}$ values (mean = $-21.5 \pm 2.2\%$), negligible (below detection limits) salinity, and a polygonal granular texture. When soaked with seawater (as seen in the lower section of Core B, Figure 4), the ice temperature increases to the freezing point of seawater (-1.9°C), causing crystals to become more rounded. Bulk salinity also increases (typically to $0.3\text{--}2 \text{ psu}$) in this facies, as does $\delta^{18}\text{O}$, indicating mixing between meteoric ice crystals and frozen seawater.

[25] The contribution from firn to the “ice mélange” decreases westward within the rift zone. Core D shows a transition below $\sim 5 \text{ m}$ with a sharp increase in $\delta^{18}\text{O}$ (becoming less negative), and slowly increasing salinities, down to $8\text{--}9 \text{ m}$ depth (Figure 4). This transition zone could be caused by recrystallized soaked firn, or by snow ice (top layer of sea ice formed by flooding of the snow). The lower 10 m section shows a granular texture with constant positive $\delta^{18}\text{O}$ values and salinities ranging from 1 to 9 , which is more typical of sea ice rather than marine ice. It is however highly unlikely that granular frazil sea ice (typically formed under conditions of

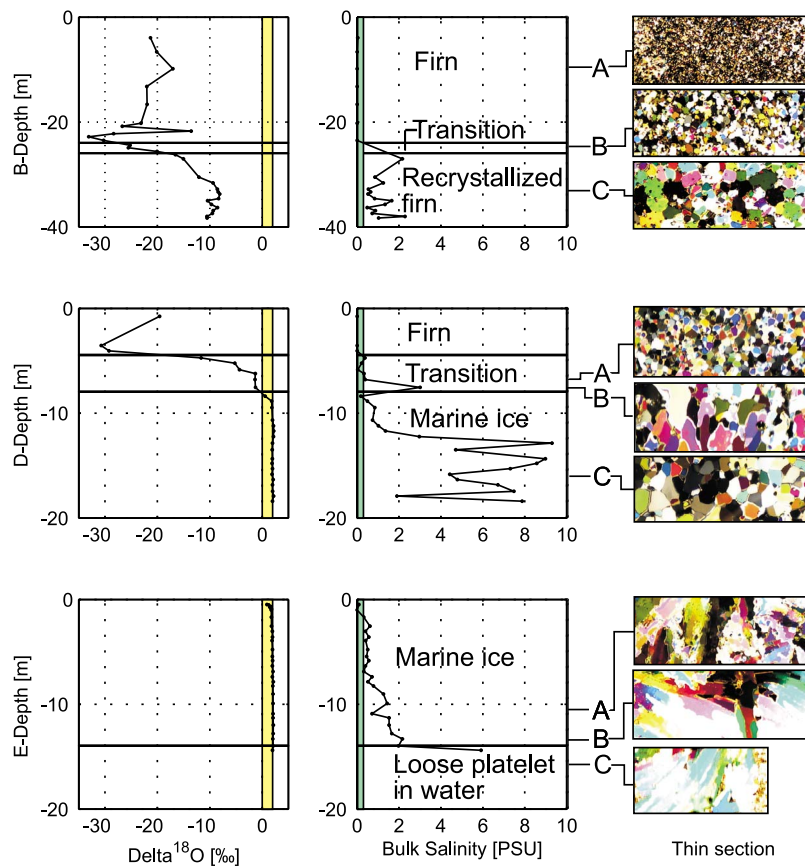


Figure 4. Isotopic composition, bulk salinity and texture for Cores B, D, and E drilled in the rift. The yellow and green bands show the reported ranges of $\delta^{18}\text{O}$ and bulk salinity for marine ice, i.e., 0–2‰ and 0.03–0.3 psu, respectively. Long axis side of thin sections is 4.5 cm. See Figure 1 for location of the drill sites.

turbulent winds) could accumulate to a total thickness of nearly 10 m. Under a turbulent regime, granular sea ice is quickly formed but can never attain depths of several meters, as the turbulence has no effect anymore once sea ice cover is sufficiently thick. In that case, columnar sea ice is more likely to form [Martin, 1981]. We therefore favor a marine ice origin, for the lower section of the core, with recent consolidation in near-surface conditions explaining the higher salinity [Tison *et al.*, 1998].

[26] Core E (Figure 4) is characterized by the absence of any snow/firn and shows ~ 12 m of marine ice outcropping at the surface in association with a dense network of crevasse fills. It also shows a regular increase of the salinity in the lower, younger layers. A profile with the televiewer showed several meters of loose frazil ice platelets in the sub-shelf water [Hubbard *et al.*, 2012]. This configuration is similar to that described by [Tison *et al.*, 1998] at the front of Hells Gate Ice Shelf, Antarctica, where the strong contrast in marine ice texture (granular as opposed to banded; the equivalent to facies at the bottom of core D as opposed to core E in the present case) was attributed to water circulation below the shelf.

6. Discussion

[27] Most observations of melt rates underneath ice shelves stem from satellite altimetry [e.g., Pritchard *et al.*, 2012]. However, close to the grounding line where the ice shelf is

not freely floating, ice thickness may well be overestimated using the satellite technique, leading to biases in basal melt rates. Our estimates based on measured ice thickness are not hampered by this bias and therefore more reliable and robust.

[28] It is generally thought that high rates of sub-shelf melting such as those observed on the Pine Island shelf ($20\text{--}30\text{ m a}^{-1}$) [Rignot, 1998; Jacobs *et al.*, 2011], and George VI Ice Shelf ($2.2\text{--}2.8\text{ m a}^{-1}$) [Potter and Paren, 1985; Corr *et al.*, 2002] are caused by incursions of CDW through deep troughs crossing the continental shelf and entering ice shelf cavities. More modest melting ($\sim 0.6\text{ m a}^{-1}$) measured beneath the Filchner Ice Shelf has been attributed to a convective thermohaline circulation due to HSSW formation [Hellmer and Olbers, 1989; Nicholls *et al.*, 2006]. Similar melt rates of 0.85 (but up to 2.85) m a^{-1} have been measured using phase-sensitive radar near the grounding line of Rutford Ice Stream [Jenkins *et al.*, 2006], and melt rates up to 0.85 m a^{-1} were also measured near the shore of the Fimbul ice shelf [Nicholls *et al.*, 2006, 2008].

[29] In contrast, our measurements across the grounding line of Roi Baudouin Ice Shelf indicate relatively small melt rates ($\sim 0.15\text{ m a}^{-1}$) compared with those measured beneath large ice shelves. Tidal influences can increase the intensification of sub-shelf circulation, resulting in increased melting and refreezing [MacAyeal, 1984; Makinson *et al.*, 2011]. Local geometry of the water column beneath a shelf and tidal mixing may also be important; model simulations [Holland,

2008] show that such mixing is confined to small areas and may only become significant under near-freezing conditions where the ocean cavity slope is shallow and tidal stirring is vigorous. Although such favorable conditions do exist beneath Roi Baudouin Ice Shelf, the relatively low melt rate indicated by our model-based interpretations of the radar data (Figure 3) suggests that this mechanism is not strong.

[30] Our observations indicate that the occurrence of accreted marine ice is restricted primarily to the rift zone. In such areas, it is thought that melt-driven convection at the sides of a rift cause cavity water to ascend and supercool, resulting in marine ice formation [Khazendar and Jenkins, 2003]. Khazendar [2000] has also shown that the amount of ice accreted in such rifts is greatly increased by the presence of pre-existing ISW formed upstream. Moreover, some preliminary conductivity/temperature/depth profiles collected from boreholes near the edge of the shelf, downstream from the rift suggest that a weak outflow of shallow ISW is present.

[31] The weak melting at the grounding line implies a weak buoyancy-forced circulation and correspondingly low freezing rates (i.e. a weak “ice pump”). Also the ice front region could easily be influenced by downwelling of the seasonally warmer surface layer [Hattermann et al., 2012]. Even if all the cavity waters were all at the surface freezing point, basal freezing may only influence the outer part of the ice shelf near the ice front [Lane-Serff, 1995], and marine ice could be melted off by downwelling beneath the ice front, leaving only marine ice in the rifts where it is protected.

[32] The incursion of HSSW or the downwelling of the seasonally warmer surface layer rather than CDW beneath RBIS is most probably controlled by regional water mass flows combined with RBIS’ shallow sub-shelf cavity. Since other ice shelves in the sector appear to be underlain by similarly shallow cavities, as evidenced by shelf-edge bathymetric data and the presence of frequent ice rises along the Princess Ragnhild Coast, it is likely that similar conditions might well prevail more widely than at RBIS alone [e.g., Hattermann et al., 2012]. Thus, we postulate that many of the ice shelves in this sector of East Antarctica are characterized by sub-shelf water circulation systems that are dominated by either the incursion of HSSW or the downwelling of ASW and characterized by low levels of sub-shelf melting and freezing relative to larger shelf systems located elsewhere in Antarctica. However, this inference has yet to be tested directly and might be considered a priority for future investigations. Nevertheless, the shallowness of the bathymetry in this area is restricted to the sections close to ice rises and ice-rise promontories. Deeper troughs at the exit of large outlet glaciers feeding into RBIS and other ice shelves in this sector of DML do exist and may eventually exhibit a different type of ice/ocean interaction.

7. Conclusions

[33] Ice-penetrating radar and kinematic GPS surveys across a grounding line, and ice core drilling within a zone of rifting farther downstream reveal sub-ice shelf melting near the grounding line and limited accretion of marine ice in the rift zone. The rate of sub-ice shelf melting is 0.15 m a^{-1} , which is rather low for an Antarctic ice shelf. Marine ice accretion is found in a rift system close to the edge of the ice shelf where it is either formed locally or protected from

melting due to warmer surface waters near the shelf edge. We conclude that the weak melt rates at the grounding line are not sufficient to sustain large-scale accretion of marine ice. We suspect that similar weak melting/refreezing conditions occur along much of the coastal sector in Dronning Maud Land where ice shelves are interspersed by ice rises and where rifting commonly occurs between those ice rises and the shelf front.

[34] **Acknowledgments.** This paper forms a contribution to the Belgian Research Programme on the Antarctic (Belgian Federal Science Policy Office), Project EA/11/3A ‘Belgian Ice Sheet – Shelf Ice Measurements in Antarctica (BELISSIMA)’. K.M. and H.C. were partly supported by a University of Washington Royalty Research Fund (project 4208). D.C. is supported by a FRIA (FRS–FNRS) grant. The isotopic analyses were carried out by B. Stenni at the Isotope Geochemistry Laboratory of the University of Trieste (Italy). The authors are indebted to A. Hubert, R. Wagemans and K. Soete for their valuable assistance in the field. We thank M. Truffer, M. Koutnik and the other referees for their constructive comments on the original manuscript.

References

- Bamber, J. L., J. L. Gomez-Dans, and J. A. Griggs (2009), A new 1 km digital elevation model of the antarctic derived from combined satellite radar and laser data—Part 1: Data and methods, *Cryosphere*, 3(1), 101–111.
- Bindschadler, R. A., H. Choi, and ASAID Collaborators (2011), High-Resolution Image-derived Grounding and Hydrostatic Lines for the Antarctic Ice Sheet, http://nsidc.org/data/docs/agdc/nsidc0489_bindschadler/index.html, Natl. Snow and Ice Data Cent., Boulder, Colo.
- Catania, G. A., H. Conway, C. F. Raymond, and T. A. Scambos (2006), Evidence for floatation or near floatation in the mouth of Kamb Ice Stream, West Antarctica, prior to stagnation, *J. Geophys. Res.*, 111, F01005, doi:10.1029/2005JF000355.
- Catania, G. A., C. Hulbe, and H. Conway (2010), Grounding line basal melt rates from radar-derived internal stratigraphy, *J. Glaciol.*, 56(197), 545–554.
- Corr, H., M. Popple, and A. Robinson (1995), Airborne radio echo investigations of a marine ice body, *Filchner-Ronne Ice Shelf Progr. Rep.* 8, pp. 14–17, Alfred Wegener Inst. for Polar and Mar. Res., Bremerhaven, Germany.
- Corr, H. F. J., A. Jenkins, K. W. Nicholls, and C. S. M. Doake (2002), Precise measurement of changes in ice-shelf thickness by phase-sensitive radar to determine basal melt rates, *Geophys. Res. Lett.*, 29(8), 1232, doi:10.1029/2001GL014618.
- Dupont, T. K., and R. B. Alley (2005), Assessment of the importance of ice-shelf buttressing to ice-sheet flow, *Geophys. Res. Lett.*, 32, L04503, doi:10.1029/2004GL022024.
- Fricker, H. A., S. Popov, I. Allison, and N. Young (2001), Distribution of marine ice beneath the Amery Ice Shelf, *Geophys. Res. Lett.*, 28(11), 2241–2244.
- Fujita, S., H. Maeno, S. Uratsuka, T. Furukawa, S. Mae, Y. Fujii, and O. Watanabe (1999), Nature of radio echo layering in the Antarctic ice sheet detected by a two-frequency experiment, *J. Geophys. Res.*, 104(B6), 13,013–13,024.
- Gagliardini, O., G. Durand, T. Zwinger, R. C. A. Hindmarsh, and E. L. Meur (2010), Coupling of ice-shelf melting and buttressing is a key process in ice-sheet dynamics, *Geophys. Res. Lett.*, 37, L14501, doi:10.1029/2010GL043334.
- Gow, A. J., and S. Epstein (1972), On the use of stable isotopes to trace the origins of ice in a floating ice tongue, *J. Geophys. Res.*, 77(33), 6552–6557.
- Greve, R. (1997), Large-scale ice-sheet modelling as a means of dating deep ice cores in Greenland, *J. Glaciol.*, 43(144), 307–310.
- Haefeli, R. (1963), A numerical and experimental method for determining ice motion in the central parts of ice sheets, *IAHS Publ.*, 61, 253–260.
- Hattermann, T., O. A. Nøst, J. M. Lilly, and L. H. Smedsrud (2012), Two years of oceanic observations below the Fimbul Ice Shelf, Antarctica, *Geophys. Res. Lett.*, 39, L12605, doi:10.1029/2012GL051012.
- Hellmer, H. H., and D. J. Olbers (1989), On the thermohaline circulation beneath the Filchner-Ronne ice shelves, *Antarct. Sci.*, 3(4), 433–442.
- Hindmarsh, R. C. A. (1999), On the numerical computation of temperature in an ice sheet, *J. Glaciol.*, 45(151), 568–574.
- Holland, P. R. (2008), A model of tidally dominated ocean processes near ice shelf grounding lines, *J. Geophys. Res.*, 113, C11002, doi:10.1029/2007JC004576.

- Hubbard, B., S. Roberson, D. Samyn, and D. Merton-Lyn (2008), Digital optical televiwing of ice boreholes, *J. Glaciol.*, *54*(188), 823–830.
- Hubbard, B., J. L. Tison, F. Pattyn, M. Dierckx, T. Boereboom, and D. Samyn (2012), Optical televiwer-based identification and characterization of material facies associated with an Antarctic ice-shelf rift, *Ann. Glaciol.*, *53*(60), 137–146.
- Huybrechts, P. (1994), Formation and disintegration of the Antarctic ice sheet, *Ann. Glaciol.*, *20*, 336–340.
- Jacobs, S. S., H. H. Helmer, C. S. M. Doake, A. Jenkins, and R. M. Frolich (1992), Melting of ice shelves and the mass balance of Antarctica, *J. Glaciol.*, *38*(130), 357–387.
- Jacobs, S. S., A. Jenkins, C. F. Giulivi, and P. Dutrieux (2011), Stronger ocean circulation and increased melting under Pine Island Glacier ice shelf, *Nat. Geosci.*, *4*, 519–523.
- Jenkins, A., H. F. J. Corr, K. W. Nicholls, C. L. Stewart, and C. S. M. Doake (2006), Interactions between ice and ocean observed with phase-sensitive radar near an Antarctic ice-shelf grounding line, *J. Glaciol.*, *52*(178), 325–346.
- Jenkins, A., P. Dutrieux, S. Jacobs, S. McPhail, J. Perrett, A. Webb, and D. White (2010), Observations beneath Pine Island Glacier in West Antarctica and implications for its retreat, *Nat. Geosci.*, *3*(7), 468–472.
- Khazendar, A. (2000), Marine ice formation in rifts of Antarctic ice shelves: A combined laboratory and modeling approach, PhD thesis, Univ. libre de Bruxelles, Brussels.
- Khazendar, A., and A. Jenkins (2003), A model of marine ice formation within Antarctic ice shelf rifts, *J. Geophys. Res.*, *108*(C7), 3235, doi:10.1029/2002JC001673.
- Khazendar, A., J. L. Tison, B. Stenni, M. Dini, and A. Bondesan (2001), Significant marine-ice accumulation in the ablation zone beneath an Antarctic ice shelf, *J. Glaciol.*, *47*(158), 359–368.
- Lane-Serff, G. F. (1995), On meltwater under ice shelves, *J. Geophys. Res.*, *100*(C4), 6961–6965.
- Lewis, E. L., and R. G. Perkins (1986), Ice pumps and their rates, *J. Geophys. Res.*, *91*(C10), 11,756–11,762.
- MacAyeal, D. R. (1984), Thermohaline circulation below the Ross Ice Shelf: A consequence of tidally induced vertical mixing and basal melting, *J. Geophys. Res.*, *89*(C1), 597–606.
- Makinson, K., P. R. Holland, A. Jenkins, K. W. Nicholls, and D. M. Holland (2011), Influence of tides on melting and freezing beneath Filchner-Ronne Ice Shelf, Antarctica, *Geophys. Res. Lett.*, *38*, L06601, doi:10.1029/2010GL046462.
- Martin, S. (1981), Frazil ice in rivers and oceans, *Ann. Rev. Fluid Mech.*, *13*, 379–397.
- Matsuoka, K., F. Pattyn, D. Callens, and H. Conway (2012), Radar characteristics of the basal interface across the grounding zone of an ice-rise promontory, East Antarctica, *Ann. Glaciol.*, *53*(60), 29–34.
- Morgan, V. (1972), Oxygen isotope evidence for bottom freezing on the Amery Ice Shelf, *Nature*, *238*, 393–394.
- Mügge, B., A. A. Savvin, R. Calov, and R. Greve (1999), Numerical age computation of the Antarctic ice sheet for dating deep ice cores, in *Advances in Cold-Region Thermal Engineering and Sciences*, edited by Y. W. K. Hutter and H. Beer, pp. 307–318, Springer, New York.
- Nicholls, K. W., et al. (2006), Measurements beneath an Antarctic ice shelf using an autonomous underwater vehicle, *Geophys. Res. Lett.*, *33*, L08612, doi:10.1029/2006GL025998.
- Nicholls, K. W., E. P. Abrahamson, K. J. Heywood, K. Stansfild, and S. Osterhus (2008), High-latitude oceanography using the Autosub autonomous underwater vehicle, *Limnol. Oceanogr.*, *53*(5), 2309–2320.
- Nishio, F., M. Ishikawa, H. Ohmae, S. Takahashi, and T. Katsushima (1984), A preliminary study of glacial geomorphology in area between Breid Bay and the Sør Rondane Mountains in Queen Maud Land, East Antarctica, *Nankyoku Shiryō*, *83*, 11–28.
- Nøst, O. A., M. Biuw, V. Tverberg, C. Lydersen, T. Hattermann, Q. Zhou, L. H. Smedsrud, and K. M. Kovacs (2011), Eddy overturning of the Antarctic Slope Front controls glacial melting in the Eastern Weddell Sea, *J. Geophys. Res.*, *116*, C11014, doi:10.1029/2011JC006965.
- Oerter, H., J. Kipfstuhl, J. Determann, H. Miller, D. Wagenbach, A. Minikin, and W. Graf (1992), Evidence for basal marine ice in the Filchner-Ronne Ice Shelf, *Nature*, *358*, 399–401.
- Padman, L., H. A. Fricker, R. Coleman, S. Howard, and L. Erofeeva (2002), A new tide model for the Antarctic ice shelves and seas, *Ann. Glaciol.*, *34*(1), 247–254.
- Pattyn, F. (2002a), Transient glacier response with a higher-order numerical ice-flow model, *J. Glaciol.*, *48*(162), 467–477.
- Pattyn, F. (2002b), Ice-flow characteristics over a rough bedrock: Implications for ice-core interpretation, *Polar Meteorol. Glaciol.*, *16*, 42–52.
- Pattyn, F. (2003), A new 3D higher-order thermomechanical ice-sheet model: Basic sensitivity, ice-stream development and ice flow across subglacial lakes, *J. Geophys. Res.*, *108*(B8), 2382, doi:10.1029/2002JB002329.
- Pattyn, F. (2010), Antarctic subglacial conditions inferred from a hybrid ice sheet/ice stream model, *Earth Planet. Sci. Lett.*, *295*, 451–461.
- Pattyn, F., A. Huyghe, S. De Brabander, and B. De Smedt (2006), Role of transition zones in marine ice sheet dynamics, *J. Geophys. Res.*, *111*, F02004, doi:10.1029/2005JF000394.
- Pattyn, F., K. Matsuoka, and J. Berte (2010), Glacio-meteorological conditions in the vicinity of the Belgian Princess Elisabeth Station, Antarctica, *Antarct. Sci.*, *22*(1), 79–85.
- Payne, A. J., P. R. Holland, A. P. Shepherd, I. C. Rutt, A. Jenkins, and I. Joughin (2007), Numerical modeling of ocean-ice interactions under Pine Island Bay's ice shelf, *J. Geophys. Res.*, *112*, C10019, doi:10.1029/2006JC003733.
- Potter, J. R., and J. G. Paren (1985), Interaction between ice shelf and ocean in George VI Sound, Antarctica, in *Antarctica, in Oceanology of the Antarctic Continental Shelf*, *Antarct. Res. Ser.*, vol. 43, edited by S. Jacobs, pp. 35–58, AGU, Washington, D. C., doi:10.1029/AR043p0035.
- Pritchard, H. D., S. R. M. Ligtenberg, H. A. Fricker, D. G. Vaughan, M. R. van den Broeke, and L. Padman (2012), Antarctic ice-sheet loss driven by basal melting of ice shelves, *Nature*, *484*, 502–505, doi:10.1038/nature10968.
- Reeh, N. (1988), A flow-line model for calculating the surface profile and the velocity, strain-rate, and stress fields in an ice sheet, *J. Glaciol.*, *34* (116), 46–54.
- Rignot, E. J. (1998), Fast recession of a West Antarctic glacier, *Science*, *281*(5376), 549–551, doi:10.1126/science.281.5376.549.
- Rignot, E. J., and S. S. Jacobs (2002), Rapid bottom melting widespread near Antarctic ice sheet grounding lines, *Science*, *296*(5575), 2020–2023.
- Rignot, E. J., J. L. Bamber, M. R. van den Broeke, C. Davis, Y. Li, W. J. van de Berg, and E. van Meijgaard (2008), Recent Antarctic ice mass loss from radar interferometry and regional climate modelling, *Nat. Geosci.*, *1*, 106–110.
- Rignot, E., J. Mouginot, and B. Scheuchl (2011), Ice flow of the Antarctic Ice Sheet, *Science*, *333*(6048), 1427–1430, doi:10.1126/science.1208336.
- Schoof, C. (2007), Ice sheet grounding line dynamics: Steady states, stability and hysteresis, *J. Geophys. Res.*, *112*, F03S28, doi:10.1029/2006JF000664.
- Shepherd, A., D. Wingham, and E. Rignot (2004), Warm ocean is eroding West Antarctic Ice Sheet, *Geophys. Res. Lett.*, *31*, L23402, doi:10.1029/2004GL021106.
- Shibuya, K., K. Doi, and S. Aoki (1999), Precise determination of geoid height and free-air gravity anomaly at Syowa Station, Antarctica, *Earth Planets Space*, *51*, 159–168.
- Smedsrud, L., A. Jenkins, D. M. Holland, and O. A. Nøst (2006), Modeling ocean processes below the Fimbul Ice Shelf, *J. Geophys. Res.*, *111*, C01007, doi:10.1029/2005JC002915.
- Souchez, R., M. Meneghel, J. L. Tison, R. Lorrain, D. Ronveaux, C. Baroni, A. Lozei, I. Tobacco, and J. Jouzel (1991), Ice composition evidence of marine ice transfer along the bottom of a small ice shelf, *Geophys. Res. Lett.*, *18*(5), 849–852.
- Thoma, M., A. Jenkins, D. Holland, and S. Jacobs (2008), Modelling circumpolar deep water intrusions on the Amundsen Sea continental shelf, Antarctica, *Geophys. Res. Lett.*, *35*, L18602, doi:10.1029/2008GL034939.
- Timmermann, R., et al. (2010), A consistent dataset of Antarctic ice sheet topography, cavity geometry, and global bathymetry, *Earth Syst. Sci. Data*, *3*(2), 231–257, doi:10.5194/essdd-3-231-2010.
- Tison, J. L., and A. Khazendar (2001), The isotope/salinity relationship in marine ice: New perspectives, *J. Geophys. Res.*, *106*(C12), 31,387–31,401.
- Tison, J. L., D. Ronveaux, and R. Lorrain (1993), Low salinity frazil ice generation at the base of a small Antarctic ice shelf, *Antarct. Sci.*, *5*(3), 309–322.
- Tison, J. L., R. Lorrain, A. Bouzette, M. Dini, T. Bondesan, and M. Stievenard (1998), Linking land fast sea ice variability to marine ice accretion at Hells Gate Ice Shelf, Ross Sea, in *Antarctic Sea Ice Physical Processes, Interactions and Variability*, *Antarct. Res. Ser.*, vol. 74, edited by M. Jeffries, pp. 375–407, AGU, Washington, D. C., doi:10.1029/AR074p0375.
- van de Berg, W. J., M. R. van den Broeke, C. H. Reijmer, and E. van Meijgaard (2006), Reassessment of the Antarctic surface mass balance using calibrated output of a regional atmospheric climate model, *J. Geophys. Res.*, *111*, D11104, doi:10.1029/2005JD006495.
- Waddington, E. D., T. A. Neumann, M. R. Koutnik, H. P. Marshall, and D. L. Morse (2007), Inference of accumulation-rate patterns from deep layers in glaciers and ice sheets, *J. Glaciol.*, *53*(183), 694–712.
- Weertman, J. (1974), Stability of the junction of an ice sheet and an ice shelf, *J. Glaciol.*, *13*, 3–11.
- Whitworth, T., A. H. Orsi, S. J. Kim, W. D. Nowlin, and R. A. Locarnini (1998), Water masses and mixing near the Antarctic slope front, in *Ocean, Ice, and Atmosphere: Interactions at the Antarctic Continental Margin*, *Antarct. Res. Ser.*, vol. 75, edited by S. S. Jacobs and R. F. Weiss, pp. 1–27, AGU, Washington D.C., doi:10.1029/AR075p0001.